NASA
Technical
Paper
3085

May 1991

Static Thrust-Vectoring Performance of Nonaxisymmetric Convergent-Divergent Nozzles With Post-Exit Yaw Vanes

Robert J. Foley and
Odis C. Pendergraft, Jr.

NASA

NASA
Technical
Paper
3085

1991

Static Thrust-Vectoring Performance of Nonaxisymmetric Convergent-Divergent Nozzles With Post-Exit Yaw Vanes

Robert J. Foley
The George Washington University
Joint Institute for Advancement of Flight Sciences
Langley Research Center
Hampton, Virginia

Odis C. Pendergraft, Jr.
Langley Research Center
Hampton, Virginia

NASA
National Aeronautics and
Space Administration
Office of Management
Scientific and Technical
Information Division

Contents

Summary 1

Introduction 1

Symbols 2

Apparatus and Procedures 3

- Facility 3
- Nozzle Design 3
- Instrumentation 4
- Balance and Bellows Calibrations 4
- Data Reduction 4

Presentation of Results 5

Results and Discussion 5

- Baseline Nozzle Performance 5
- Longitudinal Vane Location With Unvectored Nozzles ($\delta_{v,p} = 0$) 6
- Longitudinal Vane Location With Pitch-Vectored Nozzles 7
- Lateral Vane Location 8
- Double-Hinged Vane Configurations 8
- Vane Longitudinal Length 8
- Vane Vertical Height 9
- Vane Camber 9

Conclusions 10

References 11

Model Figures 12

Data Figures 26

PRECEDING PAGE BLANK NOT FILMED

ii INTENTIONALLY BLANK

Summary

An investigation has been conducted in the static test facility of the Langley 16-Foot Transonic Tunnel to determine the effects of post-exit yaw vane installation on two-dimensional convergent-divergent nozzle performance. The variation of several geometric parameters and the resulting performance and yaw-vectoring effects have been studied. Previously tested nozzles (dry-power, unvectored and vectored, and afterburning power, unvectored and vectored) were used. Vane deflection angle, longitudinal and lateral location, size, and camber were varied during this test. All vanes, regardless of position, were hinged at the exit plane. Configurations were also tested in which the vanes were hinged at two locations—the exit plane and the vane quarter-chord.

The vane concepts tested generally produced yaw-vectoring angles that were much smaller than the geometric angle for large (up to 8 percent) resultant thrust losses. On 0° pitch-vectored nozzles, yaw-vectoring effectiveness and thrust penalties were only slightly affected by vane longitudinal location. However, when the nozzles themselves were pitch vectored, yawing effectiveness decreased as the vanes were moved downstream. Thrust penalties and yawing effectiveness both dropped quickly as the vanes were moved laterally outboard. Increases in vane length produced correspondingly higher vectoring angles and thrust losses. Increased vane height produced only small increments in yawing ability. Increases in camber from 0 to 6 percent increased resultant yaw angles by 50 to 100 percent, as did the double-hinged scheme mentioned previously.

Introduction

It is anticipated that the next generation of fighter aircraft will be required to operate over a much greater performance envelope than aircraft of today, and achieving that performance will be more difficult than ever before. Studies have indicated, for example, that increases in thrust-to-weight ratio much beyond those currently available will no longer yield the performance gains achieved in the past. Designers are instead turning to such concepts as "supermaneuverability" (flight regimes for which conventional aerodynamic controls are ineffective) to attain the desired tactical advantage (ref. 1). Simulation studies in these areas indicate that the shorter maneuver times (used in both first shoot and evasion roles) made available through these advances will better enable aircraft to defeat a numerically superior foe (refs. 2 to 6). Lastly, to improve the fielding possibilities of such an aircraft, a short take-off and landing (STOL) capability may also be required.

The aspect of supermaneuverability that is of greatest interest here is post-stall maneuvering (PST). Such a maneuver entails a rapid, transient, pitch-up of the aircraft into the post-stall regime—trading energy (speed) for attitude and/or positional changes. Unfortunately, current aircraft designs generally experience degraded longitudinal and lateral-directional stability at the higher angles of attack, and conventional aerodynamic control surfaces rapidly lose their effectiveness as speed is reduced. One way to overcome this loss of aircraft control is to employ multiplane thrust vectoring to supplement or replace the aerodynamic controls. Several such vectoring concepts currently exist, and many studies indicate that at both low speed (low dynamic pressure) and high angles of attack, control forces available from thrust vectoring equal or exceed those from conventional control surfaces (refs. 7 to 9). These surfaces, normally sized large enough to maintain aircraft control at low speeds, can thus be reduced in size or even eliminated if thrust vectoring is employed, thereby reducing aircraft drag and gross weight.

One vectoring nozzle that has been thoroughly investigated over the past several years is the two-dimensional convergent-divergent (2-D C-D) nozzle. This nozzle offers internal performance comparable to existing axisymmetric (round) nozzles and highly efficient flow turning in the pitch axis (refs. 10 to 12). Reduced installed drag is offered in some installations (ref. 13). When utilized with a thrust reverser, landing-roll distances are also significantly reduced (refs. 2 and 14). However, nonaxisymmetric nozzles such as the 2-D C-D tend to be heavier than existing axisymmetric designs (without thrust-vectoring or reversing capability). Coupled with the added structure necessary to accommodate the vectoring forces generated, this increase in nozzle weight may result in increased gross vehicle weight (refs. 15 and 16).

As stated, the lateral control effectiveness of most current aircraft designs with conventional controls is reduced tremendously at the high angles of attack and low speed necessary for post-stall maneuvering. In several static investigations, the 2-D C-D nozzle has been modified to incorporate thrust vectoring in the yaw axis to counter this effect (refs. 17 to 19). The deflection of flat or curved plates into the jet exhaust to generate the vectoring force is discussed in references 18 and 19. These plates were integral with the 2-D C-D sidewall and were hinged at various locations between the nozzle throat (point of minimum duct area) and the nozzle exit. Unlike the tests in previous references, this investigation used airfoil-shaped vanes mounted away from the nozzle, at or downstream of the nozzle exit. A matrix of several

vane locations and four vane configurations (one of which was cambered) were tested at yaw deflection angles of 0°, 10°, and 20° on unvectored and pitch-vectored, dry (military) and afterburner power, 2-D C-D nozzles at nozzle pressure ratios (NPR) from 2.0 to 9.0. The use of post-exit vanes to provide both pitch and yaw vectoring on axisymmetric nozzles at static conditions has also been investigated and is reported in reference 20.

Symbols

A/B	afterburning
$(AR)_e$	nozzle exit aspect ratio (ratio of nozzle width to height, measured at nozzle exit)
$(AR)_t$	nozzle throat aspect ratio (ratio of nozzle width to height, measured at nozzle throat, w/h_t)
$(AR)_v$	vane aspect ratio (ratio of vane length to height, l_v/h_v)
A_e	nozzle exit area, in^2
A_e/A_t	nozzle expansion ratio
A_t	nozzle throat area, in^2
A_v	individual yaw vane planform area, in^2
A_v/A_e	ratio of vane planform area to nozzle exit area
F	measured thrust along body axis, positive in forward direction, lbf
F_i	ideal isentropic gross thrust, $w_p\sqrt{\frac{R_jT_{t,j}}{g^2}\frac{2\gamma}{\gamma-1}\left[1-\left(\frac{p_a}{p_{t,j}}\right)^{(\gamma-1)/\gamma}\right]}$, lbf
F_N	measured normal force, lbf
F_r	resultant gross thrust, $\sqrt{F^2+F_N^2+F_S^2}$, lbf
F_S	measured side force, lbf
g	acceleration due to gravity, 32.174 ft/sec^2
h_e	height of nozzle at exit, in.
h_v	vertical height of vane, in.
l_{df}	longitudinal length of divergent flap, from throat to exit, in.
l_v	longitudinal length of vane, in.
NPR	nozzle pressure ratio (ratio of jet total pressure to ambient pressure)
$(\mathrm{NPR})_d$	design nozzle pressure ratio (for fully expanded flow at nozzle exit)
p_a	ambient pressure, psi
$p_{t,j}$	jet total pressure, psi
R	radius, in.
R_j	gas constant, 1716 ft^2/sec^2-°R for air
SERN	single expansion ramp nozzle
Sta.	model station, in.
$T_{t,j}$	jet total temperature, °R
typ.	typical
V_h	ratio of vane height to nozzle exit height, h_v/h_e
V_l	ratio of vane length to nozzle divergent flap length, l_v/l_{df}
V_x	ratio of unvectored-vane leading-edge longitudinal distance from nozzle throat to nozzle divergent flap length, x_v/l_{df} (positive downstream)
V_y	ratio of unvectored-vane lateral distance from nozzle centerline to nozzle half-width, $y_v/(w/2)$
w	internal width of nozzle, in.
w_i	computed ideal isentropic weight-flow rate, $\left(\frac{2}{\gamma+1}\right)^{\frac{\gamma+1}{2(\gamma-1)}}\sqrt{\frac{\gamma g}{R_j}}p_{t,j}\frac{A_t}{\sqrt{T_{t,j}}}$, lbf/sec
w_p	measured weight-flow rate, lbf/sec
w_p/w_i	nozzle discharge coefficient
x_v	longitudinal distance of unvectored-vane leading edge from nozzle throat, in.
y_v	lateral distance of unvectored vane from nozzle centerline, in.
2-D C-D	two-dimensional convergent-divergent
γ	ratio of specific heats, 1.3997 for air
ΔF_r	increment in thrust ratio for installing and vectoring post-exit vanes, $(F_r/F_i)_{\substack{\text{Vanes}\\\text{installed}}} - (F_r/F_i)_{\substack{\text{Bare}\\\text{nozzle}}}$
δ_p	resultant pitch thrust-vector angle, $\tan^{-1}\frac{F_N}{F}$, deg
δ_y	resultant yaw thrust-vector angle, $\tan^{-1}\frac{F_S}{F}$, deg

$\delta_{v,p}$ geometric pitch thrust-vector angle (average of divergent flap angles) measured from model centerline, positive deflection produces positive F_N (see fig. 5(b)), deg

$\delta_{v,y}$ geometric yaw thrust-vector angle measured from model centerline, positive deflection produces positive F_S (see figs. 5(a) and 8(a)), deg

δ_y resultant yaw thrust-vector angle, $\tan^{-1}\frac{F_S}{F}$, deg

Apparatus and Procedures

Facility

This investigation was conducted in the static test facility of the Langley 16-Foot Transonic Tunnel (16-Foot Tunnel). The single-engine propulsion system, shown in figure 1, was mounted on a movable dolly that was located in a large open room. The same clean, dry, high-pressure air that is utilized in the 16-Foot Tunnel was routed to the simulation system through a series of remotely operated pressure regulating valves. Stagnation temperature of the supply air was maintained by a steam heat exchanger, also remotely operated.

Before reaching the model, high-pressure air was routed through two calibrated critical-flow venturis (mounted in parallel) to measure weight flow. From the venturis, the air was routed through two flexible lines to the dolly and up the strut through six lines to a high-pressure plenum. From this plenum, the air was moved axially and then radially outward into a low-pressure plenum through eight multiholed nozzles equally spaced around the end of the high-pressure plenum. (See fig. 2.) This complex air path was devised to minimize any forces that might be put on the force balance by the transfer of momentum as the air is passed from the nonmetric (mounted on the support system) to the metric (mounted on the balance) portion of the model. Two metal bellows were used to bridge the metric-to-nonmetric break, to prevent any loss of air volume, and to minimize the axial forces caused by pressurization. Once in the metric low-pressure plenum, the air was moved axially through a transition section (to change from circular to rectangular cross-sectional flow area), a choke plate, an instrumentation section, and finally the nozzles being tested. (See fig. 1.) The jet was exhausted to atmosphere. All model hardware was connected to the instrumentation section at model station 41.13. When in operation, the simulation system was visually monitored through the use of a closed-circuit television camera.

Nozzle Design

The baseline 2-D C-D nozzles used in this investigation are shown in figure 3. Two representative nozzle power settings—dry (military) power and afterburner power—were used. The nozzle sidewalls remained fixed at a constant width of 4.000 in. Nozzle area ratio was controlled by nozzle throat area and divergent flap exit area. The pitch-vector angle was determined from the average of the top and bottom divergent flap angles. Both flaps were symmetrically deflected either toward or away from the nozzle centerline to control area ratio, and they were differentially deflected (one flap toward the centerline, one away) to control pitch-vector angle. These nozzles were previously tested, and the results of those investigations are reported in references 11 and 19.

Typical installations of the post-exit vanes on the 2-D C-D nozzles are shown in figures 4 to 6 to illustrate the method of vane attachment and orientation. The baseline vane, size A, was designed such that its height approximately matched the maximum vertical travel of the nozzle divergent flaps when pitch vectored in the A/B power setting. This was done so that the baseline vane would provide at least some yaw vectoring when coupled with a pitch-vectored nozzle (fig. 5(b)). Vane size B maintained the baseline length but increased height by about 22 percent. Vane size C maintained the baseline height but increased length by 50 percent. To study the effects of camber, a duplicate set of size C vanes were built, but with 6-percent camber. All uncambered vanes were NACA 0006 airfoils, and the cambered vanes were NACA 6506 airfoils (ref. 21), as shown in figure 6.

To study the effects of vane location on static performance, a matrix of six vane locations were tested. These six locations are illustrated in figure 7 (with "+" symbols) and represent the vane leading-edge locations, regardless of size or type, when undeflected.

Yaw vectoring was accomplished by deflection of the post-exit vanes as shown in figures 4 and 5. Each vane was supported by two booms rigidly mounted to the nozzle sidewall. When viewed from the side, the boom height was 0.5 in. each, or a total of about 22 percent of vane height for the baseline size A vane. This height was kept constant for all vane locations. When the nozzle was pitch vectored, the vanes remained fixed—they did not rotate in the pitch axis with the nozzle divergent flaps. All vanes that were hinged about a vertical axis at the outboard edge of the nozzle exit plane (i.e., location A), regardless of location and size, are referred to as single-hinged vanes.

Results from previous static investigations indicate that the vane turned out of the exhaust flow had little effect on flow vectoring (ref. 17). To improve the yaw-vectoring capability of this vane, the baseline size A vane was tested with additional rotation about the vane quarter-chord (fig. 8). These vanes are referred to as double-hinged vanes. Both vanes were therefore immersed in the nozzle exhaust plume. The combination of rotations used was arbitrarily chosen to try to maximize coverage of the nozzle exit by the vanes.

Both the double-hinged and the cambered-vane geometries mentioned were concepts originally developed for this investigation to improve vane turning performance.

Instrumentation

An internally mounted, six-component, temperature-compensated, strain-gauge balance was used to measure all forces and moments experienced by the model. Two calibrated critical-flow venturis were used in parallel to measure the weight flow of air supplied to the model. (See ref. 22.) One four-probe rake and two three-probe rakes in the instrumentation section were used to measure jet total pressure. A single thermocouple, also in the instrumentation section, was used to measure jet total temperature (fig. 1). All balance and pressure transducer calibrations had an accuracy of 0.5 percent of the full-scale value.

Balance and Bellows Calibrations

The propulsion simulation system was designed to minimize any extraneous forces and moments that might be put on the balance (figs. 1 and 2). However, small interaction forces (or tares) caused by the presence of the propulsion simulation system accounted for up to several percent of the total load on any balance component. These tares were determined by calibration before the model was tested (ref. 23).

The presence of the metal bellows, necessary to maintain a sealed air passage across the metric-to-nonmetric gap, required two sets of calibrations. Jet-off calibrations were first performed because the bellows acted essentially as a spring between the nonmetric and metric ends of the balance and introduced one set of interactions. Loadings of known weights were put on each balance component, one at a time, and the loads that were induced on each individual component were recorded. These loads were used to correct the measured loads for bellows stiffness tares. The characteristics of the bellows, and thus the amount of tare forces induced on the balance, varied with the pressure and amount of air being passed through the bellows. To determine these tares, the air system was operated with unvectored convergent Stratford calibration nozzles (ref. 23) of various throat areas and of known performance (i.e., known axial force), and the induced tare forces and moments were computed as a function of nozzle throat area and pressure differential across the bellows. These tare forces were then subtracted from the test data (ref. 24).

Data Reduction

All analog data were recorded simultaneously, digitized, and stored on magnetic tape. Fifty frames of data, taken at a rate of 10 frames per second, were measured at each point. Averages of these 50 frames were used in all calculations (ref. 24). To be consistent, all data points were taken in ascending order of nozzle pressure ratio.

The performance parameters presented in this report are axial thrust ratio F/F_i, resultant thrust ratio F_r/F_i, nozzle discharge coefficient w_p/w_i, resultant pitch-vector angle δ_p, and resultant yaw-vector angle δ_y. All force quantities presented herein, with the exception of resultant thrust ratio, were resolved along the model centerline.

Axial thrust ratio F/F_i is the ratio of actual thrust measured along the body axis, corrected for balance interactions and airflow system tares, to ideal isentropic thrust. Ideal thrust is computed from measured weight-flow rate w_p, jet total pressure $p_{t,j}$, and jet total temperature $T_{t,j}$.

Resultant thrust ratio F_r/F_i is the ratio of resultant gross thrust to ideal isentropic thrust. Resultant gross thrust is the vector sum of corrected axial-, normal-, and side-force balance measurements. By definition, axial and resultant thrust ratios differ only when the jet exhaust is being vectored off the body centerline. When this occurs, axial thrust ratio F/F_i decreases and F_r/F_i remains constant, except for losses in flow turning. Thus, resultant thrust ratio represents a truer indication of nozzle efficiency.

Thrust-vector angle δ_p is the effective angle in the longitudinal-vertical plane that is determined by vector summation of the corrected axial- and normal-force components of the balance.

Thrust-vector angle δ_y is the effective angle in the longitudinal-lateral plane that, similar to δ_p, is determined by vector summation of the corrected axial- and side-force components of the balance.

Lastly, nozzle discharge coefficient w_p/w_i is the ratio of measured weight-flow rate to the ideal isentropic weight-flow rate. Actual weight-flow rate is

measured by two critical-flow venturis mounted in the air delivery system. Ideal weight-flow is computed from measured jet total temperature and pressure and measured nozzle throat area (minimum area of nozzle internal flow path). Discharge coefficient is a measure of the efficiency of the nozzle in passing airflow, and large changes in w_p/w_i between configurations would indicate variations in engine-nozzle internal losses, and there would be corresponding adverse effects on engine performance.

Presentation of Results

The results of this investigation are presented in the form of plotted data in figures 9 to 30, which are organized as follows:

Figure

Performance of baseline (no vanes installed) nozzles 9

Performance variation with increasing V_x for size A vane with unvectored dry-power nozzle 10

Performance variation with increasing V_x for size A vane with unvectored A/B power nozzle 11

Vane installation effects on performance for unvectored A/B nozzle 12

Performance variation with vane longitudinal position for unvectored dry-power and A/B power nozzles at $V_y = 1.00$ 13

Performance variation with increasing V_x for size A vane with vectored dry-power nozzle 14

Performance variation with increasing V_x for size A vane with vectored A/B power nozzle 15

Performance variation with increasing V_y for size A vane with unvectored dry-power nozzle at $V_x = 1.000$ 16

Performance variation with increasing V_y for size A vane with unvectored dry-power nozzle at $V_x = 1.440$ 17

Performance variation with increasing V_y for size A vane with unvectored A/B power nozzle at $V_x = 1.000$ 18

Performance variation with increasing V_y for size A vane with unvectored A/B power nozzle at $V_x = 1.455$ 19

Performance variation with vane lateral position for unvectored dry and A/B power nozzles at $V_x = 1.000$ 20

Performance comparison of single- and double-hinged vanes on unvectored dry and A/B power nozzles 21

Performance variation with vane hinge type for unvectored A/B power nozzle with $V_x = 1.455$ and $V_y = 1.00$ 22

Performance variation with increasing V_l for unvectored dry-power nozzle 23

Performance variation with increasing V_l for unvectored A/B power nozzle 24

Performance variation with vane length for unvectored dry-power nozzle with $V_x = 1.440$ and $V_y = 1.00$ 25

Performance variation with increasing V_h for vectored dry-power nozzle 26

Performance variation with increasing V_h for vectored A/B power nozzle 27

Performance comparison of cambered and uncambered vanes on unvectored dry-power nozzle 28

Performance comparison of cambered and uncambered vanes on unvectored A/B power nozzle 29

Performance variation with vane camber for unvectored A/B power nozzle with $V_x = 1.455$ and $V_y = 1.00$ 30

Results and Discussion

Baseline Nozzle Performance

The geometries for the baseline nozzles used are presented in figure 3, along with a table of important nozzle parameters. As is typical for convergent-divergent (C-D) nozzles, nozzle expansion ratio A_e/A_t usually determined the pressure ratio at which the nozzle operated fully expanded and at peak ($(\mathrm{NPR})_d$) efficiency (e.g., see fig. 9(a)). Below this design point, the flow was overexpanded, and shock losses along with shock-induced separation caused overall thrust efficiency (F/F_i) to decrease rapidly. Above this design point, the flow was underexpanded and thrust efficiency was decreased, though not as quickly as when overexpanded. Axial thrust ratio for the unvectored nozzles shown in figure 9(a) peaked for the dry-power nozzle ($(\mathrm{NPR})_d = 2.97$) at about NPR = 3.0 and at about NPR = 5.0 for the A/B power nozzle ($(\mathrm{NPR})_d = 4.65$).

Also typical for C-D nozzles is the variation of nozzle discharge coefficient (w_p/w_i) with NPR. As an NPR of 1.89 was approached and passed, the nozzle became choked (sonic velocity at the throat), and w_p/w_i remained nearly constant throughout the

remaining NPR range. The nozzle throat area A_t, in conjunction with this discharge coefficient, determined the amount of airflow that could be passed through the nozzle and thus, the amount of thrust attainable at a given nozzle setting. Reference 25 provides an excellent theoretical analysis of these flow processes.

When both the dry and A/B power nozzles were pitch vectored, there was a slight decrease in nozzle expansion ratio and throat area as a result of the manner in which the 2-D C-D divergent flaps were moved to accomplish the pitch vectoring. (See fig. 3.) Pressure data from reference 12 indicated that on the pitch-vectored A/B power nozzle, the throat pivoted about the radius on the lower convergent flap and moved downstream on the upper divergent flap. Similar results were also expected for the vectored dry-power nozzle. The drop in discharge coefficient in figure 9 from the unvectored to the vectored nozzles (especially at the dry-power nozzle) reaffirmed the aforementioned decreases in nozzle exit and throat areas. Most of the turning occurred in the subsonic flow ahead of the skewed throat and thus would not produce large supersonic shock losses. The dry and A/B power nozzles exhibited substantially different characteristics of flow-turning δ_p variation with NPR.

On the vectored dry-power nozzle, again as a result of the vectoring geometry of the 2-D C-D nozzle, the lower divergent flap was longer than the upper divergent flap relative to the exhaust-flow centerline. The flow was fully contained for about 70 percent of the distance down the divergent section (again relative to the flow centerline). For the remaining 30 percent, the flow expanded against a solid boundary on one side (the lower flap) and against a free boundary on the other side. This type of expansion is typical of single expansion ramp nozzles (SERN), whose behavior is well documented. (E.g., see ref. 26.) Typically, these unvectored SERN nozzles experience a large variation in thrust-vector angle with NPR; this variation results in a steady decrease in resultant pitch-vector angle as NPR is increased. This same trend, as shown in figure 9(b), is exhibited by the pitch-vectored dry-power nozzle of the current investigation.

A very different flow phenomenon occurred on the vectored A/B power nozzle. Flow in its divergent section was probably dominated by complete flow separation from the lower divergent flap at the lower values of NPR (overexpanded nozzle operation) and resulted in low thrust deflection angles (ref. 12). As NPR was increased, the flow progressively attached to the lower divergent flap, and resultant pitch-vector angle increased between NPR = 2.0 and 4.0 (fig. 9(b)). Resultant thrust ratio also decreased in this NPR range. These nozzle trends were first reported extensively in reference 12 (except the vectored dry-power nozzle) and subsequently in reference 19 (including the vectored dry-power nozzle).

Longitudinal Vane Location With Unvectored Nozzles ($\delta_{v,p} = 0$)

The behavior of the exhaust plume downstream of the nozzle is just as important as its behavior within the nozzle, particularly in this investigation in which yaw vanes are mounted downstream of the nozzle exit. At values of NPR less than $(\mathrm{NPR})_d$, overexpansion and then compression of the jet exhaust plume created a pocket in which the undeflected vanes could be located so as not to interact with the jet exhaust and thus minimize the scrubbing drag effects on nozzle performance. As NPR was increased to the design point and then above, undeflected vanes placed at the nozzle exit interacted with the expanding jet plume and had to be moved laterally outward, away from the exit, to avoid any effects at this condition.

Vane size A was tested with the dry and A/B power unvectored nozzles at 0°, 10°, and 20° geometric yaw angles. Results for a constant value of $V_y = 0$ (lateral location) and several values of V_x (longitudinal location) with these nozzle and vane settings are presented in figures 10 and 11.

Installation of the unvectored vanes on the unvectored dry-power nozzles caused thrust losses at NPR = 3.0 (near the $(\mathrm{NPR})_d$ of 2.97) of about 1 to 1.5 percent. These losses were generally independent of V_x and were most likely caused by the added skin friction of the vane surfaces. During underexpanded conditions above the design NPR, the dry-power nozzles, with vanes installed, experienced increased thrust losses in addition to those noted previously (up to 1 percent more). These additional losses were an indication that the exhaust plume was probably expanding laterally and further impinging upon the vanes (fig. 10(a)). Similar results would be expected for the A/B power nozzle, though the weight-flow limitations of the facility precluded setting of NPR much above the design value. The effects of an overexpanded nozzle, however, can be seen clearly with the A/B power configurations (fig. 11(a)). Below $(\mathrm{NPR})_d$, the exhaust plume collapsed slightly upon exiting the nozzle and caused little or no flow to interact with the vanes. Therefore, there were no additional thrust losses. As the design NPR (4.65) was reached, the nozzle began to fill completely and the skin-friction losses increased to a maximum of about 1.5 percent at maximum NPR.

Since the vane was closest to the nozzle exit plane for vane location A (V_x = 1.000), these losses began at the lowest NPR. They occurred at a higher NPR for location B (V_x = 1.455), and for location C (V_x = 1.909) the losses began to grow just as the design NPR was reached.

When the yaw vanes were deflected, large thrust losses resulted. For the dry-power nozzle, losses at NPR = 3.0 of 4 to 5 percent were experienced at all values of V_x when the vanes were deflected 20° (fig. 10(c)). The vanes were turning supersonic flow, and shock losses were expected to be high. For the yaw angles tested, oil flow visualization photographs (not shown) indicated that the exhaust flow was almost completely separated from the vane turned out of the flow. The vane turned into the flow most likely produced most of the flow turning and all of the thrust losses (ref. 18). Only 7° to 8° of actual flow turning δ_y was produced. Typically, values of δ_y at and near $(\mathrm{NPR})_d$ remained steady, peaked at some higher NPR, and then rapidly fell off. This pattern was repeated at all three vane locations, and the peak shifted to higher values of NPR as V_x was increased.

Similar results with the vanes deflected were obtained for the A/B power nozzle with $\delta_{v,p}$ = 0° (figs. 11(b) and 11(c)). At design conditions, thrust losses of 4 to 6 percent and yaw angles of 8° to 10° were produced at a 20° deflection angle. The data for the A/B nozzle with $\delta_{v,p}$ = 0° and with A vanes located at V_x = 1.455 are replotted in figure 12 to more clearly show the effects of increasing vane yaw angle on nozzle performance and vane turning efficiency for all three vane deflection angles (0°, 10°, and 20°). As shown, thrust-ratio losses were as high as 6 percent for $\delta_{v,y}$ = 20°, and resultant yaw-vector angles averaged about 8° for V_x = 1.455. Data from figures 10 and 11, cross-plotted to show the effect of vane longitudinal position on yaw-vector angle ratio $\delta_y/\delta_{v,y}$ and nozzle resultant thrust-ratio increments ΔF_r at nozzle design NPR, are presented in figure 13 for both the dry-power and A/B power nozzles. As shown, moving the yaw vanes aft produced mixed but only minor effects on ΔF_r and $\delta_y/\delta_{v,y}$.

Even though post-exit vanes produce only small resultant yaw-vector angles, whether from nonaxisymmetric nozzles (ref. 18) or axisymmetric nozzles (ref. 20) at static conditions, they can be very effective at wind-on conditions (e.g., see ref. 27) because of the effects on the surrounding external flow.

Longitudinal Vane Location With Pitch-Vectored Nozzles

As previously stated, the yaw vanes were rigidly attached to the nozzle sidewalls by two support booms. That is, when the nozzles themselves were pitch vectored, the vanes did not move vertically with the exhaust plume (fig. 4). Coverage of the exhaust plume by the vanes was reduced, especially as V_x was increased. The yaw-vectoring capability of the vane would thus be expected to diminish, and this was indeed the case. Vane size A was tested on the vectored dry and A/B power nozzles with 0°, 10°, and 20° vane deflection angles (figs. 14 and 15).

Installing the unvectored vanes at location A (V_x = 1.000) on the dry-power, pitch-vectored ($\delta_{v,p}$ = 19.56°) nozzle introduced a resultant thrust loss of about 1 percent at NPR near design, just as for the nozzle with $\delta_{v,p}$ = 0°. However, at the two higher values of V_x (locations B and C), vane-installed, resultant thrust losses were 0.5 percent less near design NPR than with the unvectored nozzle (compare fig. 10(a) with fig. 14(a)). At NPR = 3.0, the dry-power nozzle was vectoring the exhaust plume 20° in pitch. Thus, the jet, when vectored, was probably in contact with an increasingly larger percentage of the vane surface (more skin-friction drag) as the vane was moved upstream (decreasing V_x) and/or as NPR was increased to underexpanded conditions (plume billows outward).

A similar effect could be seen with the pitch-vectored A/B power nozzle at NPR = 5.0 (fig. 15(a)). There was little change in the resultant thrust lost at V_x = 1.000 between the unvectored and pitch-vectored nozzles (both experiencing about 1.5-percent losses), but as V_x was increased, any resultant thrust losses that were present were decreased when the nozzle was pitch vectored.

As expected, there was a reduction in vane flow-turning (yaw-vectoring) capability with the vanes deflected when installed on the pitch-vectored nozzles. Comparing the results for the unvectored and pitch-vectored dry-power nozzles, smaller resultant yaw-vector angles and reduced thrust losses are evident for the pitch-vectored configurations (compare fig. 10(b) with fig. 14(b) and fig. 10(c) with fig. 14(c)). As the yaw vanes were moved aft (increasing V_x), the magnitude of the resultant thrust loss and resultant yaw thrust-vector angle for the pitch-vectored nozzles tended to decrease from those shown for the unvectored nozzles. The same patterns of resultant yaw angle with NPR were still present, but the magnitudes were reduced substantially.

Installation of these same yaw vane configurations on the pitch-vectored A/B power nozzle produced results similar to those for the dry-power nozzle (figs. 15(b) and 15(c)). As explained previously, flow conditions in this nozzle were characterized by a rapid increase in resultant pitch-vector angle at NPR from 2.0 to 4.0. As this occurred, the yaw-vectoring ability of the externally mounted yaw vanes generally dropped sharply. At NPR = 5.0, the flow in the nozzle stabilized (attached flow), and trends similar to those for the pitch-vectored dry-power nozzle could be discerned.

Lateral Vane Location

The effects of lateral vane location on nozzle performance at two constant longitudinal stations are presented in figures 16 and 17 for the unvectored dry-power nozzle and in figures 18 and 19 for the unvectored A/B power nozzle. On both nozzles, the size A vane was tested at 0°, 10°, and 20° yaw deflection angles.

For the dry-power nozzle, thrust loss of about 1 percent at NPR = 3.0 occurred with the undeflected vanes installed at location A (fig. 16(a)). As V_y was increased (vanes moved outboard), these losses disappeared. Similar results were seen when the vanes were moved from location B to location E (fig. 17(a)). The vanes at $V_y > 1.0$ (locations D, E, and H) were removed from the exhaust such that the plume did not impinge upon the vanes, and there was no associated skin-friction drag. With the unvectored A/B power nozzle, a similar decrease in thrust losses associated with vane installation at the outboard locations was experienced (figs. 18(a) and 19(a)).

Just as the distance of the vanes from the exhaust plume served to maintain efficiency in the unvectored configurations, it also reduced the effectiveness of the vanes in turning the jet (yaw thrust vectoring). When the deflected vanes were moved laterally from location A to location H on the dry-power nozzle with $\delta_{v,p} = 0°$, resultant yaw-vector angle decreased (figs. 16(b) and 16(c)). The reduction of resultant thrust loss as the vanes were moved from location A to location H, as well as the reduced vectoring capacity, indicated again that the vanes were simply too far removed (laterally) from the exhaust to be effective at static conditions. Similar results were observed when moving from location B to location E (figs. 17(b) and 17(c)).

For these same configurations on the A/B power nozzle with $\delta_{v,p} = 0°$, similar trends in resultant thrust ratio and resultant yaw-vector angle for the same variations in vane lateral location were found (figs. 18 and 19). The data for the dry and A/B power nozzles with $\delta_{v,p} = 0°$ and with size A vanes at $V_x = 1.000$ from figures 16 and 18 are cross-plotted in figure 20 to more clearly illustrate the effects of vane lateral spacing on yaw-vector angle ratio $\delta_y/\delta_{v,y}$ and nozzle resultant thrust-ratio increments ΔF_r. As stated previously, for both the dry-power and A/B power nozzles, moving the vanes outboard reduces thrust losses. When $\delta_{v,y} = 0°$, resultant thrust losses were essentially eliminated for all but the vane positions with $V_y = 1.0$. Also, the turning effectiveness of the vanes was adversely affected as the vanes were moved outboard.

Double-Hinged Vane Configurations

A vane deflected out of the exhaust flow was responsible for little, if any, of the flow turning, as the exhaust flow never attached itself to the vane inner surface. A method was devised by which this vane could also be immersed in the jet. The geometry for these double-hinged vanes is presented in figure 8. As illustrated, both vanes should now be able to generate flow turning. Vane size A, with this double-hinged geometry, was tested at location B on both the dry and A/B nozzles with $\delta_{v,p} = 0°$. A direct comparison of the nozzle performance parameters between the single- and double-hinged vanes is presented in figure 21.

On the dry-power nozzle with $\delta_{v,p} = 0°$ at NPR = 3.0, for both the 10° and 20° yaw deflection angles, the double-hinged vanes produced more than double the resultant thrust losses of the single-hinged vanes with less than a 50-percent improvement to the resultant yaw angle (fig. 21(a)). At 20° yaw deflection, δ_y at NPR = 3.0 increased from about 8° to 11°, while resultant thrust ratio decreased an additional 4.5 percent. Similar results were observed for the A/B power nozzle compared with the dry-power nozzle, except that slightly better turning performance was achieved for most conditions.

Data for the unvectored A/B nozzle with size A vanes at $V_x = 1.455$ and $V_y = 1.00$ are cross-plotted in figure 22 at NPR = 4.6 to more clearly show the effect of vane deflection angle and hinge type on turning efficiency and resultant thrust-ratio loss. As indicated previously, turning efficiency is substantially higher for the double-hinged vanes than for the single-hinged vanes, but thrust-ratio losses are more than doubled at $\delta_{v,y} = 20°$.

Vane Longitudinal Length

To determine the effects of vane length, the baseline size A vane was increased in length 50 percent,

from $V_l = 1.758$ to 2.637 on the dry-power nozzle. This size C vane was tested at locations A, B, and E and at yaw-vector angles of 0°, 10°, and 20° on both the unvectored dry and A/B power nozzles. A comparison of results for size A and size C vanes is presented in figures 23 and 24.

At $\delta_{v,y} = 0°$, the size C vane exhibited resultant thrust-ratio trends similar to those discussed previously for the size A vane on both the dry and A/B power nozzles (figs. 23(a) and 24(a)). For the dry-power nozzle with $\delta_{v,p} = 0°$, increasing vane length increased thrust losses over the entire NPR range tested (most likely because of increased skin-friction drag) when the vane was installed at $V_y = 1.00$. Moving the vane downstream from the exit (increasing V_x) had little effect on resultant thrust losses. As with the size A vane, thrust losses for the size C vane on the A/B power nozzle, as NPR increased, did not begin until the jet plume expanded sufficiently to contact the vanes. The NPR at which this occurred increased as the vanes were moved downstream. On the dry-power nozzle, at values of NPR greater than $(\mathrm{NPR})_d$, thrust losses increased as the jet expanded increasingly outward onto the vanes, and the magnitude of those thrust losses was higher for the larger C vane. At location E, just as with the size A vane, the C vane created no thrust losses over most of the NPR test range for either nozzle. As before, the vane was mounted far enough away (laterally) from the exhaust to avoid contact with the plume. However, at higher values of NPR on the dry-power nozzle, the jet expanded sufficiently to impinge upon the vanes, and thrust losses increased slightly (fig. 23(a)).

As expected, the larger size C vane, when deflected, generally increased resultant yaw-vector angle, particularly for the dry-power nozzle (figs. 23(b) and 23(c)). However, for the A/B power nozzle (figs. 24(b) and 24(c)), this improved yaw-vectoring performance was accompanied by larger resultant thrust-ratio losses. These effects were small for the A/B power nozzle with $\delta_{v,y} = 10°$.

To show more clearly the effect of vane turning angle for two different vane lengths on the vane turning efficiency and resultant thrust-ratio losses, data for the dry-power nozzle at $V_x = 1.440$ and $V_y = 1.00$ are cross-plotted in figure 25 at NPR = 3.0 for the size A vanes ($V_l = 1.758$) and the size C vanes ($V_l = 2.637$). As previously indicated, both turning efficiency and resultant thrust-ratio losses were increased for the dry-power nozzle by increasing vane length.

Vane Vertical Height

The effect of vane height was determined by testing the size B vane, which had a height about 22 percent greater than the baseline size A vane. The height of the baseline A vane was sized such that it approximately matched the maximum vertical movement (up and down) of the upper or lower nozzle flap as pitch-vector angle was increased from 0° to 20°. Using this criterion ensured that, during yaw vectoring, at least a small percentage of the baseline vane would turn into the exhaust, even when the nozzle was pitch vectored. The most extreme case was the vectored A/B power nozzle. (See fig. 5(b).) Vane size B was tested to see if increased yaw-vector angle, when coupled with nozzle pitch vectoring, could be realized. A comparison of nozzle performance for vane sizes B and A on both the pitch-vectored dry and A/B power nozzles is presented in figures 26 and 27, respectively.

When installed at $\delta_{v,y} = 0°$ on either pitch-vectored nozzle, the size B vane experienced nearly identical resultant thrust losses (within 0.5 percent) as the A vane. As with the size A vane (figs. 26(a) and 27(a)), these losses were constant with V_x. The deflected size B vane produced a slight increase in resultant yaw vectoring over the size A vane and caused up to an additional 0.5-percent thrust loss on both vectored nozzles, especially for $\delta_{v,y} = 20°$ (figs. 26(c) and 27(c)). These results and the added structural weight of these larger B vanes would eliminate their use on an aircraft.

Vane Camber

To determine the effects of camber, a vane of the same dimensions as the size C vane, but with 6-percent camber, was built. This vane was tested at the same locations as the uncambered size C vane, namely locations A, B, and E, and at yaw-vector angles of 0°, 10°, and 20°. Performance comparisons between the cambered and uncambered vanes, installed on the dry and A/B power nozzles with $\delta_{v,p} = 0°$, are presented in figures 28 and 29, respectively.

At $\delta_{v,y} = 0°$, the cambered vane exhibited results essentially the same as the uncambered vane at all three locations and on both nozzles (figs. 28(a) and 29(a)). As for the uncambered vane, resultant thrust losses were experienced at both values of V_x (locations A and B), and these losses disappeared as V_y was increased (location E).

For deflected-vane cases (figs. 28(b) and (c) and figs. 29(b) and (c)) on both the dry and A/B power

nozzles, and at all three locations tested, resultant yaw-vector angles were increased for the cambered vanes by 50 to 100 percent over the uncambered vanes and caused an additional resultant thrust penalty of only about 1 to 2 percent. Treating the vanes as airfoils immersed in supersonic flow, the cambered vanes would, at a given vane angle of attack, be expected to generate more lift (lateral thrust deflection in this application) for less drag (thrust loss) than the uncambered counterparts (ref. 21). On the dry-power nozzle, for 20° yaw deflection, resultant yaw angles were nearly equal to the geometric angle. On the A/B power nozzle with vanes at $V_y = 1.00$ and 10° yaw deflection, resultant yaw angles equal to the geometric angle were achieved at near-design NPR. At 20° yaw deflection, $(\mathrm{NPR})_d$ could not be set, because the maximum yawing-moment capacity of the force balance was reached first. However, significant resultant yaw-vector angles were generated even at values of NPR below design. The cambered vanes are probably capable of producing 19° to 20° of resultant yaw-vector angle, which is double what the uncambered vanes developed. These large increases in δ_y were accompanied by only 1- to 2-percent additional resultant thrust penalties. Further improvements may be possible by optimizing the combination of camber amount and location.

Data from figure 29 for the A/B power nozzle are cross-plotted in figure 30 to compare the effects of uncambered and cambered C vanes on turning efficiency and resultant thrust-ratio losses for yaw vane deflection. This figure clearly shows the dramatic increase in turning efficiency for the vanes at $V_x = 1.455$ and $V_y = 1.00$ with only about another 1-percent loss in resultant thrust ratio.

Conclusions

The effects of post-exit yaw vane installation on two-dimensional convergent-divergent nozzles have been studied in the static test facility of the Langley 16-Foot Transonic Tunnel. Both unvectored and pitch-vectored nozzle models of dry and afterburner power two-dimensional convergent-divergent (2-D C-D) nozzles were tested with vanes on and vanes off at nozzle pressure ratios from 2.0 to 9.0.

All vanes were mounted external to the 2-D C-D nozzle; therefore, it was expected that the presence of the vanes would significantly alter the external flow field, but would have little effect upon the internal flow characteristics of the jet. The nozzle throat was well upstream of, and well isolated from, the yaw vanes, and therefore discharge coefficient was not affected by vane installation, positional change, or geometric yaw-vector angle. Similarly, when the nozzles were pitch vectored, all turning in the pitch plane was accomplished internally, and pitch-vector angles were only slightly affected, if at all, by the presence of the vanes.

Airfoil-shaped post-exit vanes of various planform shapes (uncambered and cambered) were tested at several locations relative to the nozzle exit at 0°, 10°, and 20° yaw deflection angles. Also, trends in the data indicate the following conclusions for nozzles tested at static conditions:

1. When installed along a line extending downstream from the inner surface of the dry-power nozzle sidewall, undeflected vanes produced thrust losses of 1.0 to 2.5 percent because of scrubbing losses on the vanes. For the afterburning (A/B) power nozzle, vane scrubbing losses of about 1.5 percent are evident just above the design nozzle pressure ratio at a nozzle pressure ratio (NPR) of 6 (maximum flow limit).
2. As the vanes were moved laterally outward away from the inner surface of the nozzle sidewall, undeflected thrust losses disappeared.
3. When mounted on nozzles unvectored in pitch, deflected vanes produced one-half or less of the geometric yaw-vector angle, with large thrust penalties. This effect was fairly constant with longitudinal location.
4. Yaw thrust-vectoring effectiveness of the vanes dropped substantially as the vanes were moved laterally outboard of the nozzle exit.
5. When the nozzles were pitch vectored, yawing effectiveness of the vanes decreased, and this decrease became more pronounced as the vanes were moved downstream.
6. Increasing vane length by 50 percent produced up to about a 50-percent increase in yawing effectiveness, depending on NPR, with small additional resultant thrust losses for the yaw vanes undeflected and deflected.
7. Increasing vane height by about 20 percent produced only a slight increase in yawing effectiveness for the pitch-vectored nozzles. The added structural weight of these vanes would probably preclude their use on an aircraft.
8. Cambered vanes produced 50 to 100 percent more yaw vectoring than uncambered vanes with no additional undeflected thrust penalty and only 1 to 2 percent additional thrust penalty when deflected.

9. Especially on the A/B power nozzle, the double-hinged concept produced substantially more turning efficiency but substantially more resultant thrust losses.

NASA Langley Research Center
Hampton, VA 23665-5225
March 1, 1991

References

1. Herbst, W. B.: Future Fighter Technologies. *J. Aircr.*, vol. 17, no. 8, Aug. 1980, pp. 561–566.
2. Capone, Francis J.: The Nonaxisymmetric Nozzle—It Is for Real. AIAA Paper 79-1810, Aug. 1979.
3. Well, K. H.; Faber, B.; and Berger, E.: Optimization of Tactical Aircraft Maneuvers Utilizing High Angles of Attack. *J. Guid., Control, & Dyn.*, vol. 5, no. 2, Mar.–Apr. 1982, pp. 131–137.
4. Tamrat, B.: Flight Path/Nose Pointing: A Required Criterion in Future Fighter Aircraft Design. AIAA-83-2123, Aug. 1983.
5. Herrick, Paul W.: Propulsion Influences on Air Combat. AIAA-85-1457, July 1985.
6. Gallaway, C. R.; and Osborn, R. F.: Aerodynamics Perspective of Supermaneuverability. AIAA-85-4068, Oct. 1985.
7. Capone, Francis J.; and Mason, Mary L.: *Multiaxis Aircraft Control Power From Thrust Vectoring at High Angles of Attack.* NASA TM-87741, 1986.
8. Reubush, David E.; and Berrier, Bobby L.: *Effects of the Installation and Operation of Jet-Exhaust Yaw Vanes on the Longitudinal and Lateral-Directional Characteristics of the F-14 Airplane.* NASA TP-2769, 1987.
9. Capone, Francis J.; and Bare, E. Ann: *Multiaxis Control Power From Thrust Vectoring for a Supersonic Fighter Aircraft Model at Mach 0.20 to 2.47.* NASA TP-2712, 1987.
10. Leavitt, Laurence D.: Summary of Nonaxisymmetric Nozzle Internal Performance From the NASA Langley Static Test Facility. AIAA-85-1347, July 1985.
11. Re, Richard J.; and Leavitt, Laurence D.: *Static Internal Performance Including Thrust Vectoring and Reversing of Two-Dimensional Convergent-Divergent Nozzles.* NASA TP-2253, 1984.
12. Capone, Francis J.: *Static Performance of Five Twin-Engine Nonaxisymmetric Nozzles With Vectoring and Reversing Capability.* NASA TP-1224, 1978.
13. Capone, Francis J.: *Aeropropulsive Characteristics at Mach Numbers up to 2.2 of Axisymmetric and Nonaxisymmetric Nozzles Installed on an F-18 Model.* NASA TP-2044, 1982.
14. Laughrey, J. A.; Drape, D. J.; and Hiley, P. E.: Performance Evaluation of an Air Vehicle Utilizing Non-Axisymmetric Nozzles. AIAA Paper 79-1811, Aug. 1979.
15. Wallace, Hoyt W.; and Bowers, Douglas L.: Advanced Nozzle Integration for Air Combat Fighter Application. AIAA-82-1135, June 1982.
16. Callahan, C. J.: Tactical Aircraft Payoffs for Advanced Exhaust Nozzles. AIAA-86-2660, Oct. 1986.
17. Mason, Mary L.; and Berrier, Bobby L.: *Static Investigation of Several Yaw Vectoring Concepts on Nonaxisymmetric Nozzles.* NASA TP-2432, 1985.
18. Mason, Mary L.; and Berrier, Bobby L.: *Static Performance of Nonaxisymmetric Nozzles With Yaw Thrust-Vectoring Vanes.* NASA TP-2813, 1988.
19. Taylor, John G.: *Static Investigation of a Two-Dimensional Convergent-Divergent Exhaust Nozzle With Multiaxis Thrust-Vectoring Capability.* NASA TP-2973, 1990.
20. Berrier, Bobby L.; and Mason, Mary L.: *Static Performance of an Axisymmetric Nozzle With Post-Exit Vanes for Multiaxis Thrust Vectoring.* NASA TP-2800, 1988.
21. Abbott, Ira H.; and Von Doenhoff, Albert E.: *Theory of Wing Sections.* Dover Publ., Inc., c.1959.
22. Berrier, Bobby L.; Leavitt, Laurence D.; and Bangert, Linda S.: *Operating Characteristics of the Multiple Critical Venturi System and Secondary Calibration Nozzles Used for Weight-Flow Measurements in the Langley 16-Foot Transonic Tunnel.* NASA TM-86405, 1985.
23. Peddrew, Kathryn H., compiler: *A User's Guide to the Langley 16-Foot Transonic Tunnel.* NASA TM-83186, 1981.
24. Mercer, Charles E.; Berrier, Bobby L.; Capone, Francis J.; Grayston, Alan M.; and Sherman, C. D.: *Computations for the 16-Foot Transonic Tunnel—NASA, Langley Research Center, Revision 1.* NASA TM-86319, 1987. (Supersedes NASA TM-86319, 1984.)
25. Liepmann, H. W.; and Roshko, A.: *Elements of Gasdynamics.* John Wiley & Sons, Inc., c.1957.
26. Berrier, Bobby L.; and Leavitt, Laurence D.: *Static Internal Performance of Single-Expansion-Ramp Nozzles With Thrust-Vectoring Capability up to 60°.* NASA TP-2364, 1984.
27. Berrier, Bobby L.: Results From NASA Langley Experimental Studies of Multiaxis Thrust Vectoring Nozzles. *SAE 1988 Transactions—Journal of Aerospace,* Section 1—Volume 97, c.1989, pp. 1.1289–1.1304. (Available as SAE Paper 881481.)

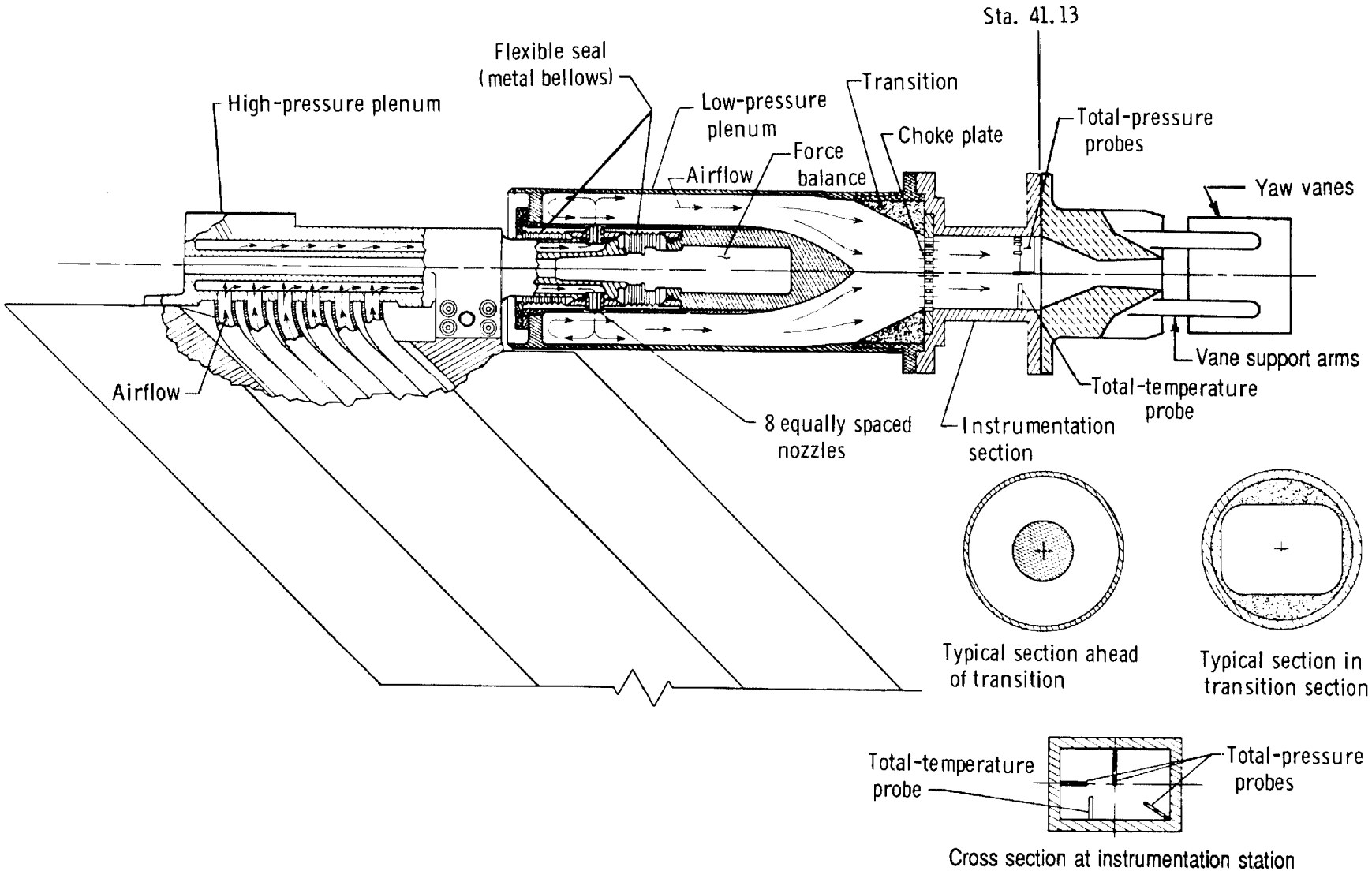

Figure 1. Sketch of single-engine propulsion simulation system with 2-D C-D nozzle and post-exit yaw vanes installed. Not a true cross section of nozzle.

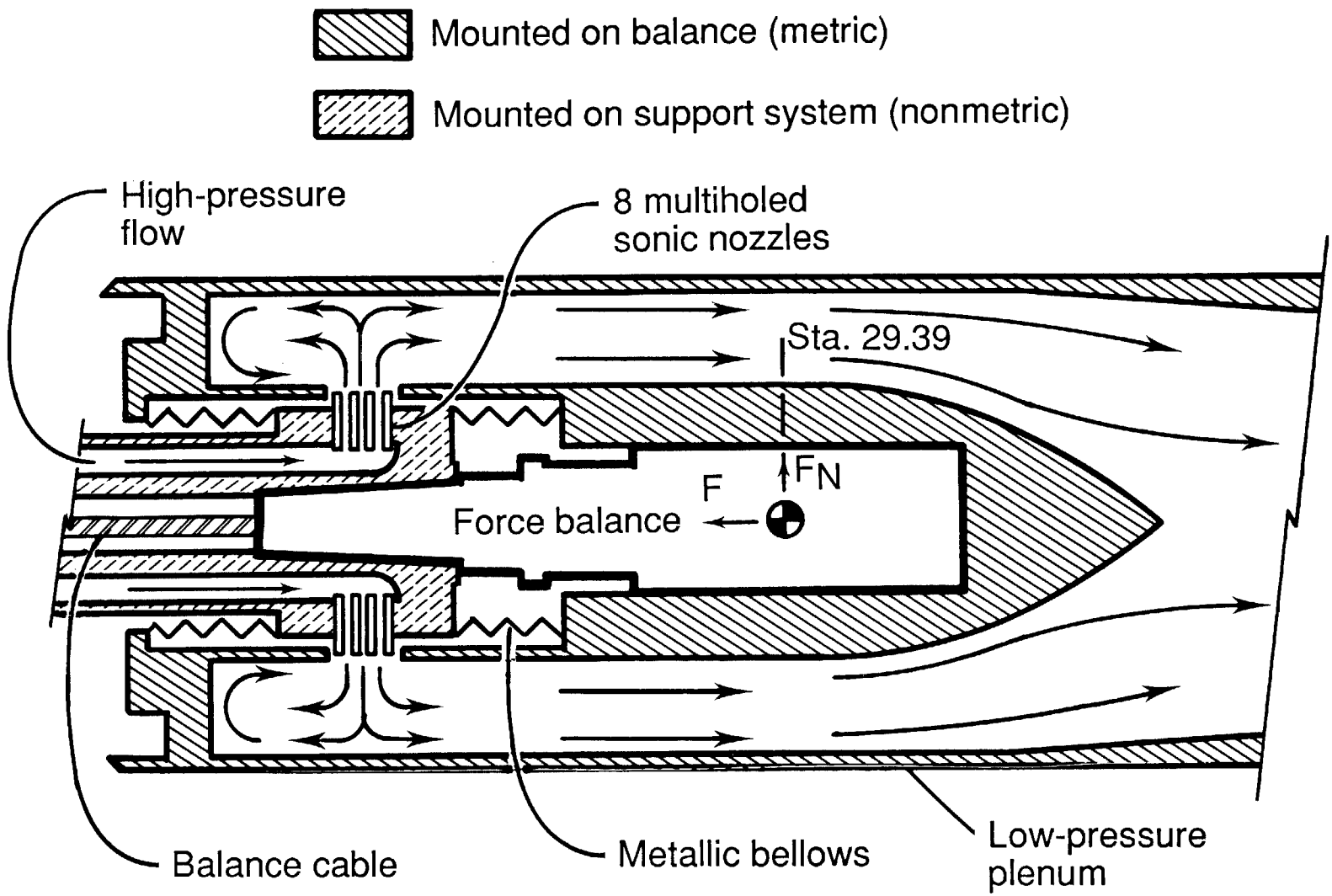

Figure 2. Schematic cross section of flow transfer system.

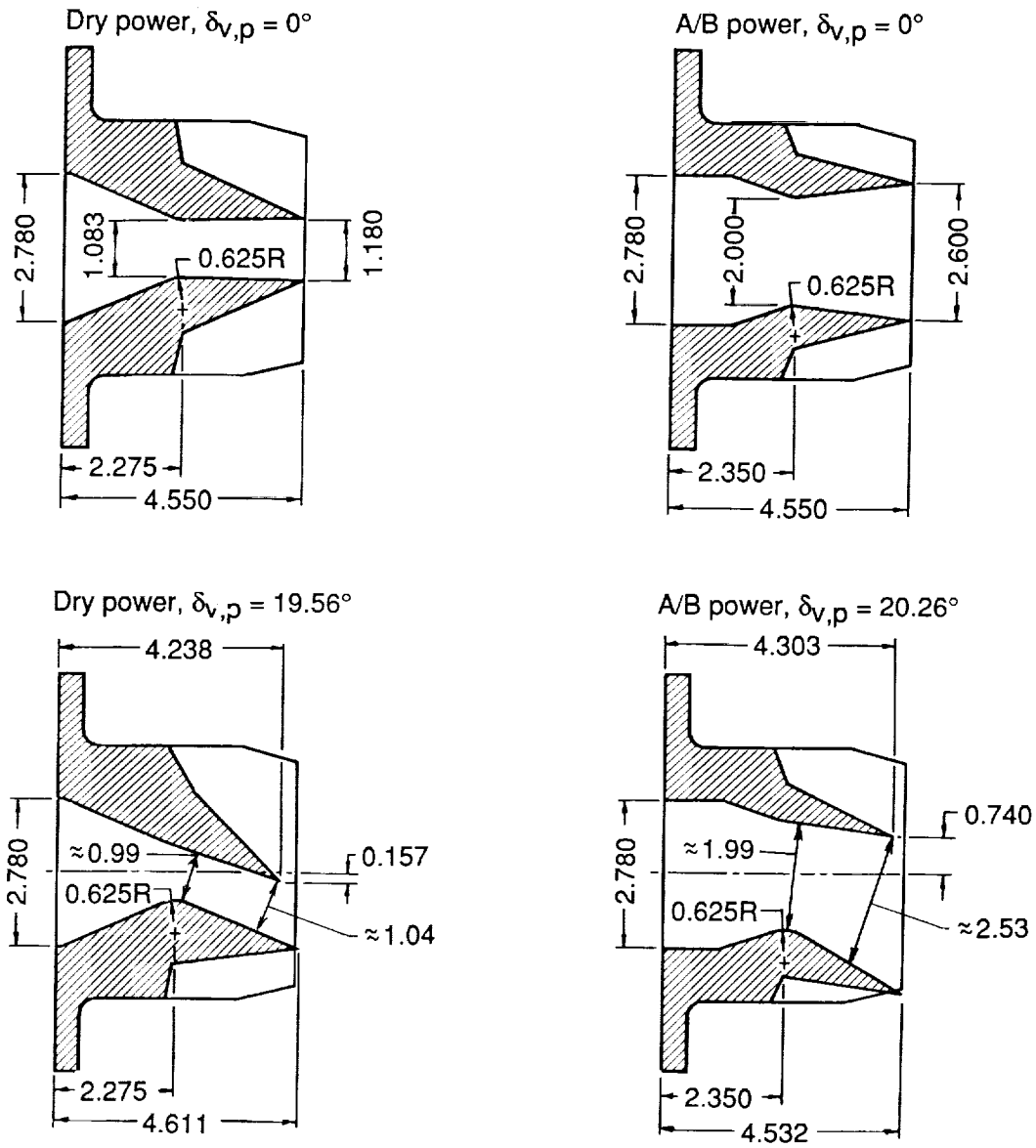

Nozzle	$\delta_{v,p}$, deg	$(NPR)_d$	A_e/A_t	A_e, in^2	A_t, in^2	$(AR)_t$	$(AR)_e$
Dry power	0	2.97	1.089	4.720	4.332	3.693	3.390
Dry power	19.56	2.63	1.050	4.150	3.953	4.048	3.854
A/B power	0	4.65	1.300	10.400	8.000	2.000	1.538
A/B power	20.26	4.40	1.270	10.124	7.972	2.007	1.580

Figure 3. Sketches of baseline nozzle geometry. (Nozzle internal width is 4.000 in.; all linear dimensions are in inches.)

ORIGINAL PAGE
BLACK AND WHITE PHOTOGRAPH

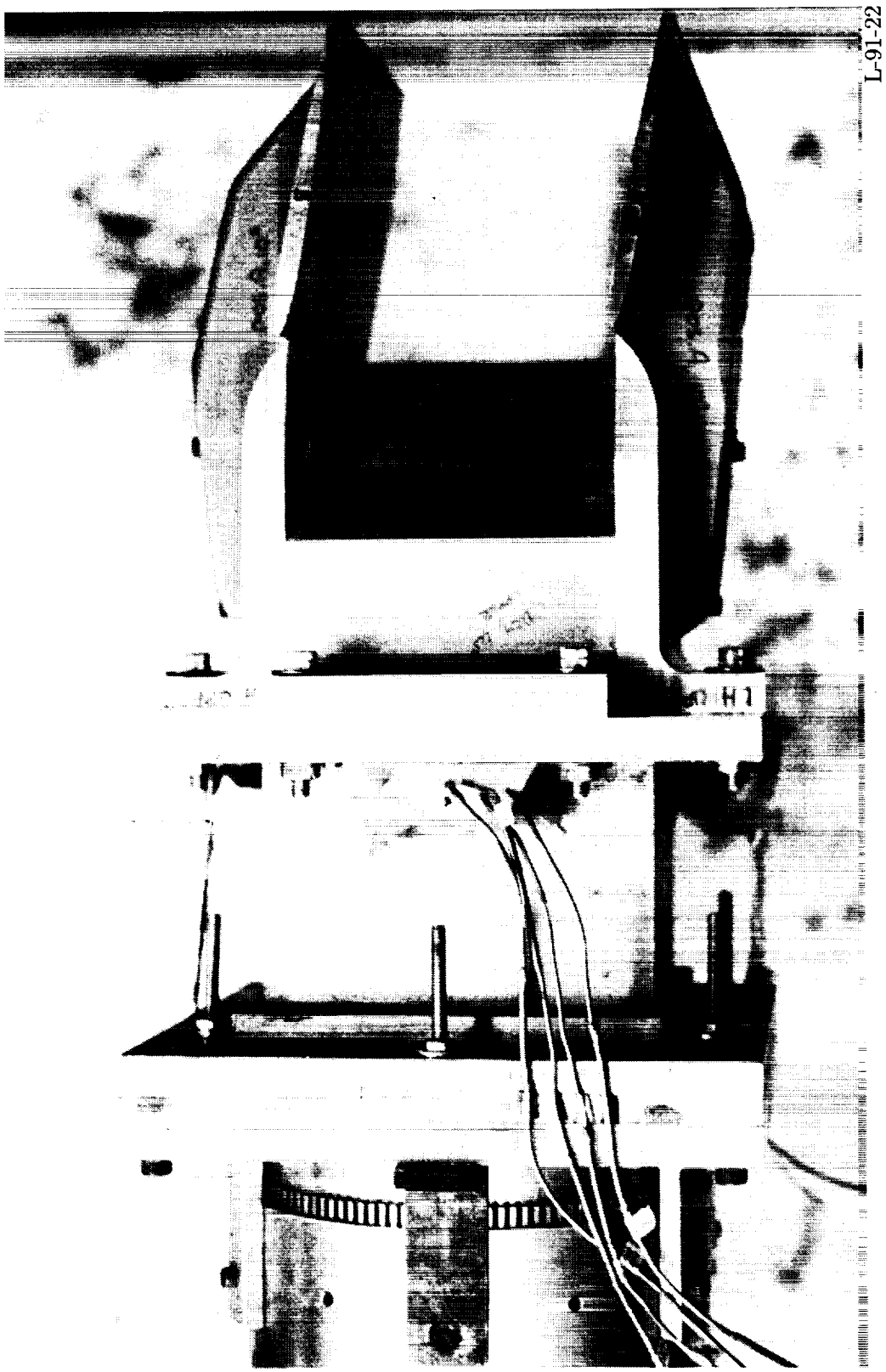

(a) Top view.

Figure 4. Photographs of size B vane installed on vectored, dry-power nozzle. $\delta_{v,y} = 10°$.

ORIGINAL PAGE
BLACK AND WHITE PHOTOGRAPH

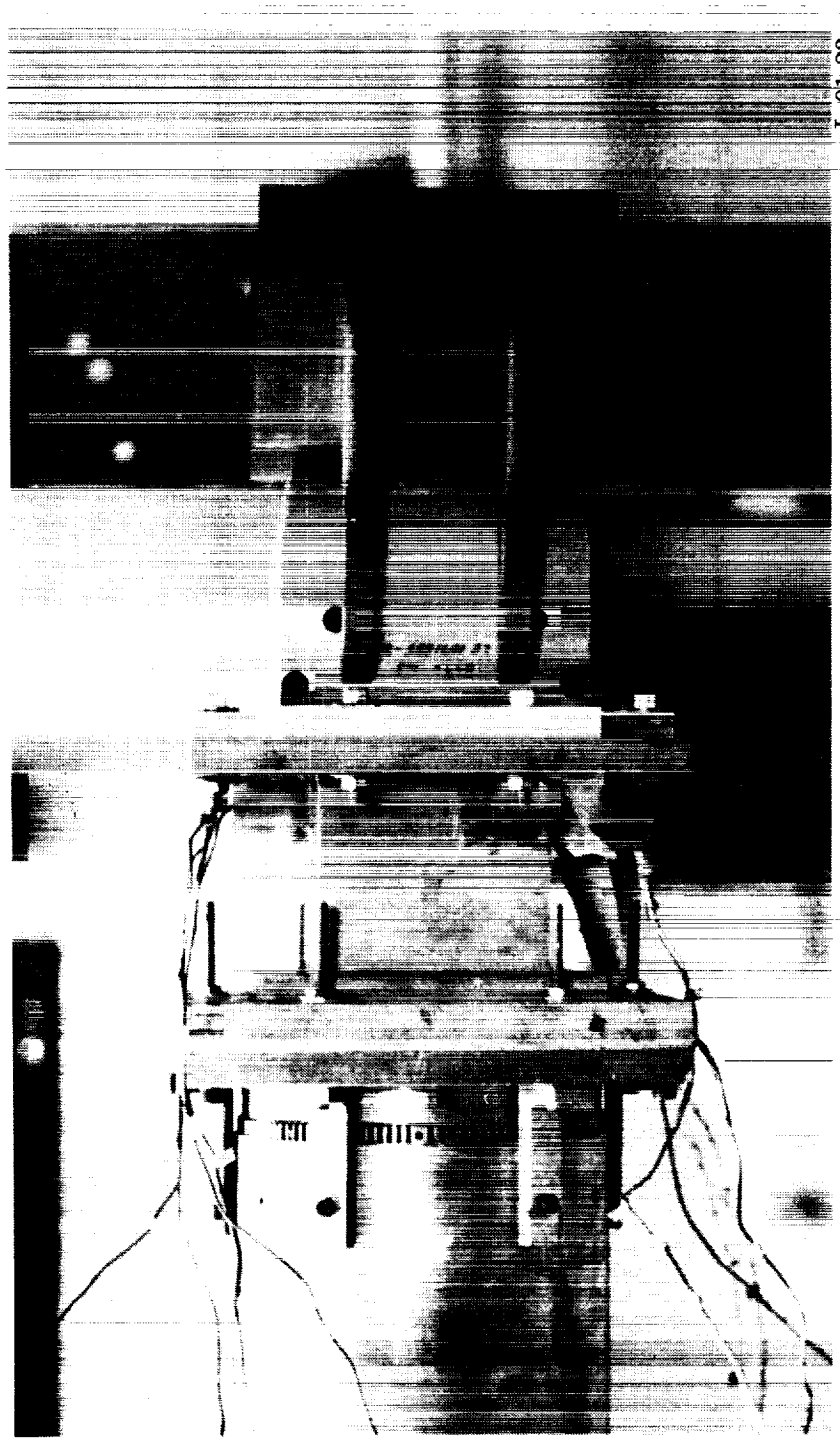

L-91-23

(b) Side view.

Figure 4. Continued.

ORIGINAL PAGE
BLACK AND WHITE PHOTOGRAPH

L-91-24

(c) Rear quarter view.

Figure 4. Continued.

ORIGINAL PAGE
BLACK AND WHITE PHOTOGRAPH

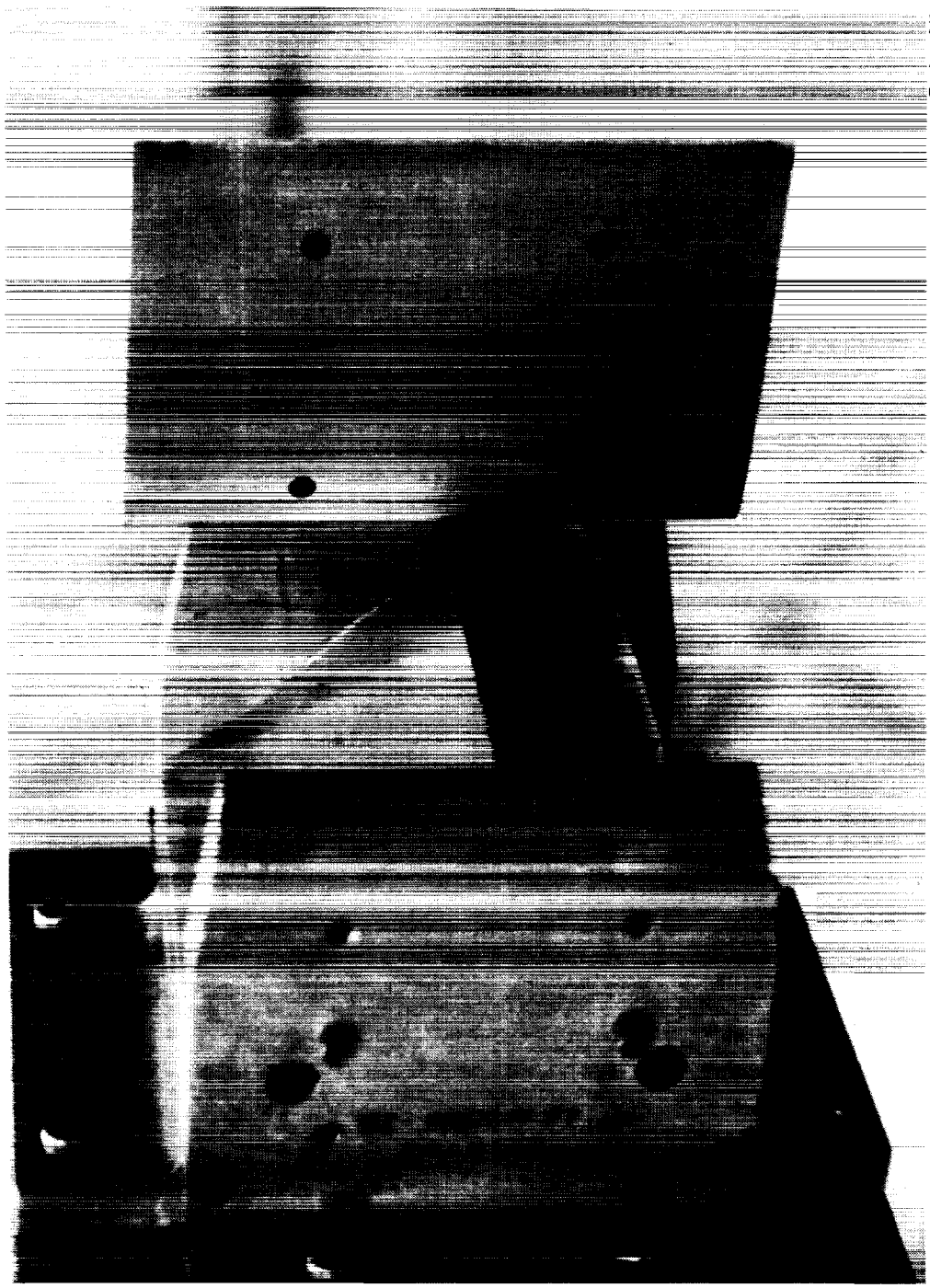

L-91-25

(d) Close up of rear quarter view with near vane removed.

Figure 4. Concluded.

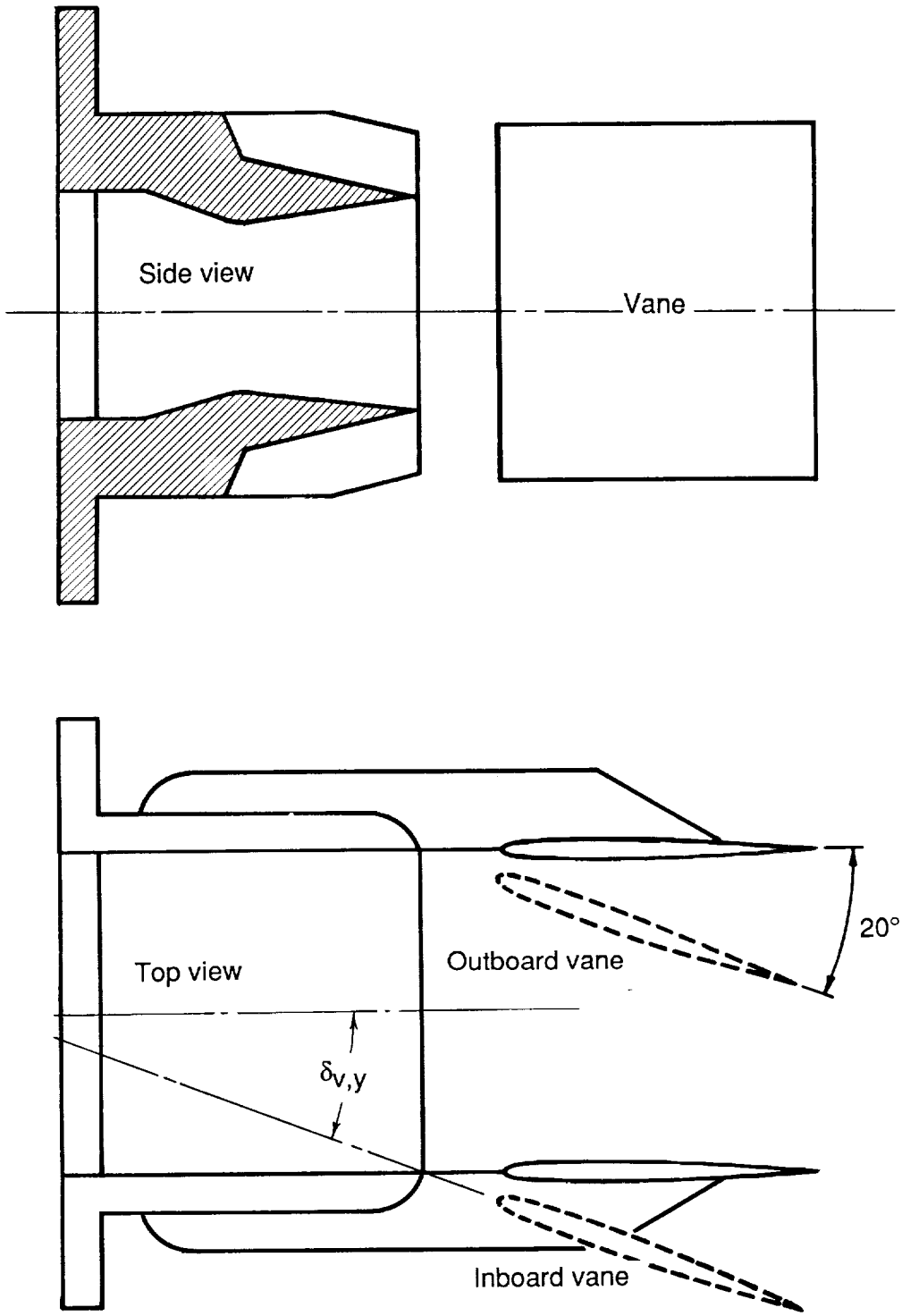

(a) Unvectored A/B power nozzle.

Figure 5. Typical installations of post-exit yaw vanes on 2-D C-D nozzles.

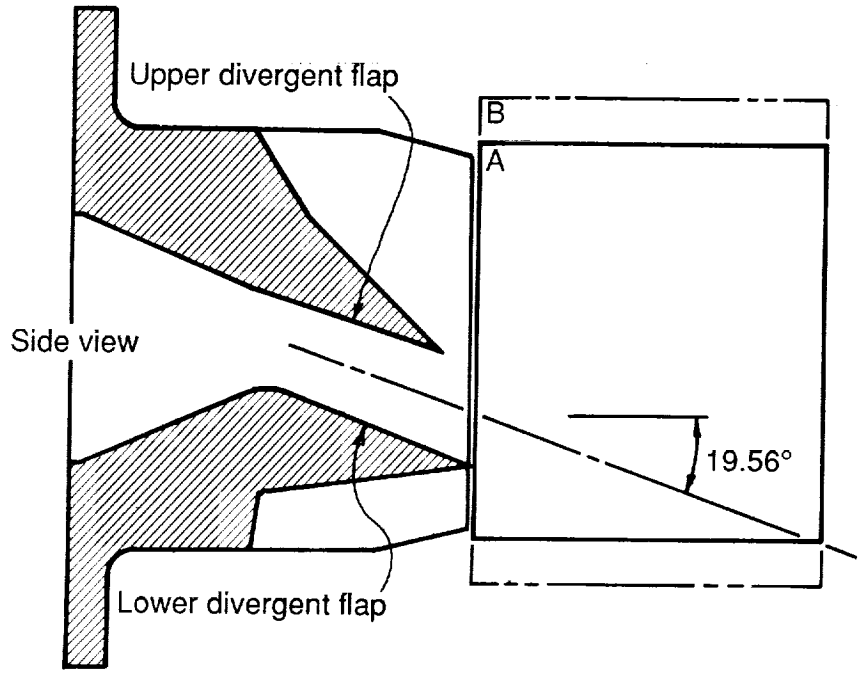

Dry-power nozzle, vane location A

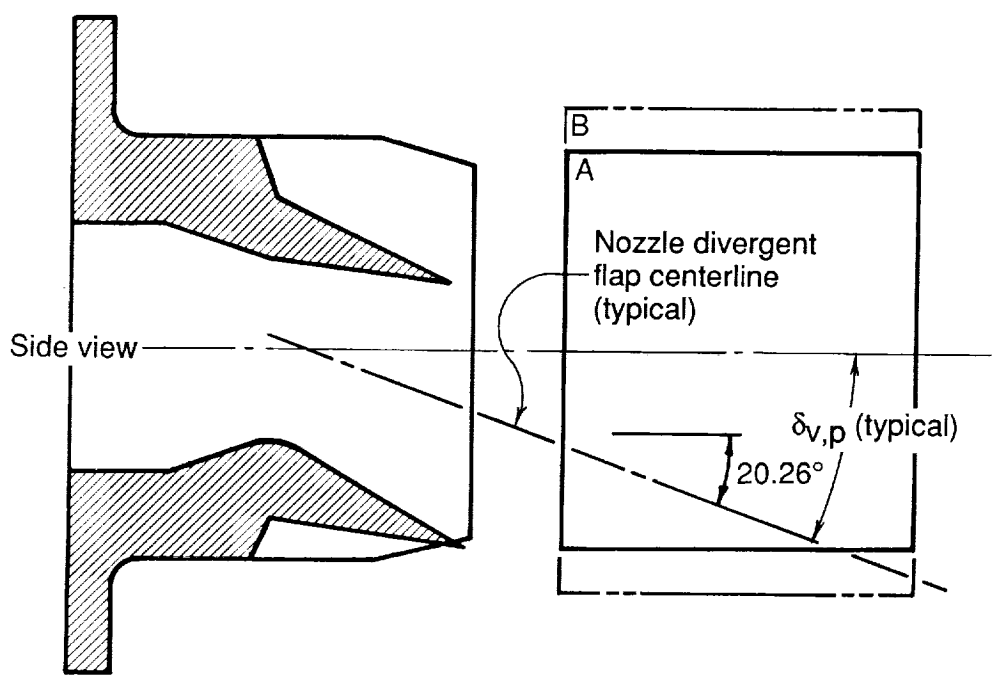

A/B power nozzle, vane location B

(b) Vectored nozzles.

Figure 5. Concluded.

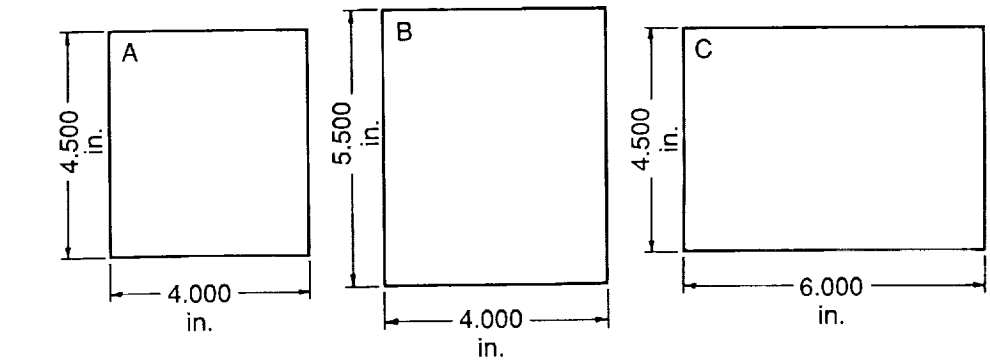

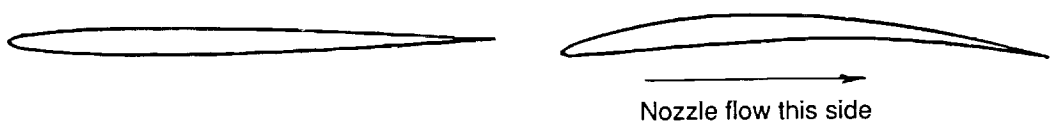

Vane size	h_V, in.	l_V, in.	A_V, in^2	$(AR)_V$
A	4.500	4.000	18.000	0.889
B	5.500	4.000	22.000	.727
C	4.500	6.000	27.000	1.333

Uncambered vanes are NACA 0006 airfoils
Cambered vanes are NACA 6506 airfoils (size C only)

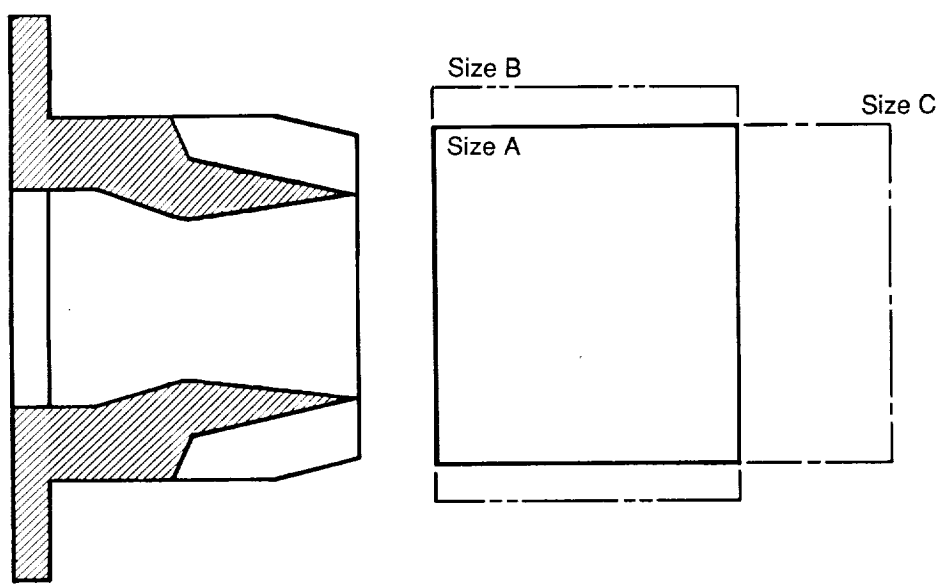

Figure 6. Sketches of vane geometries.

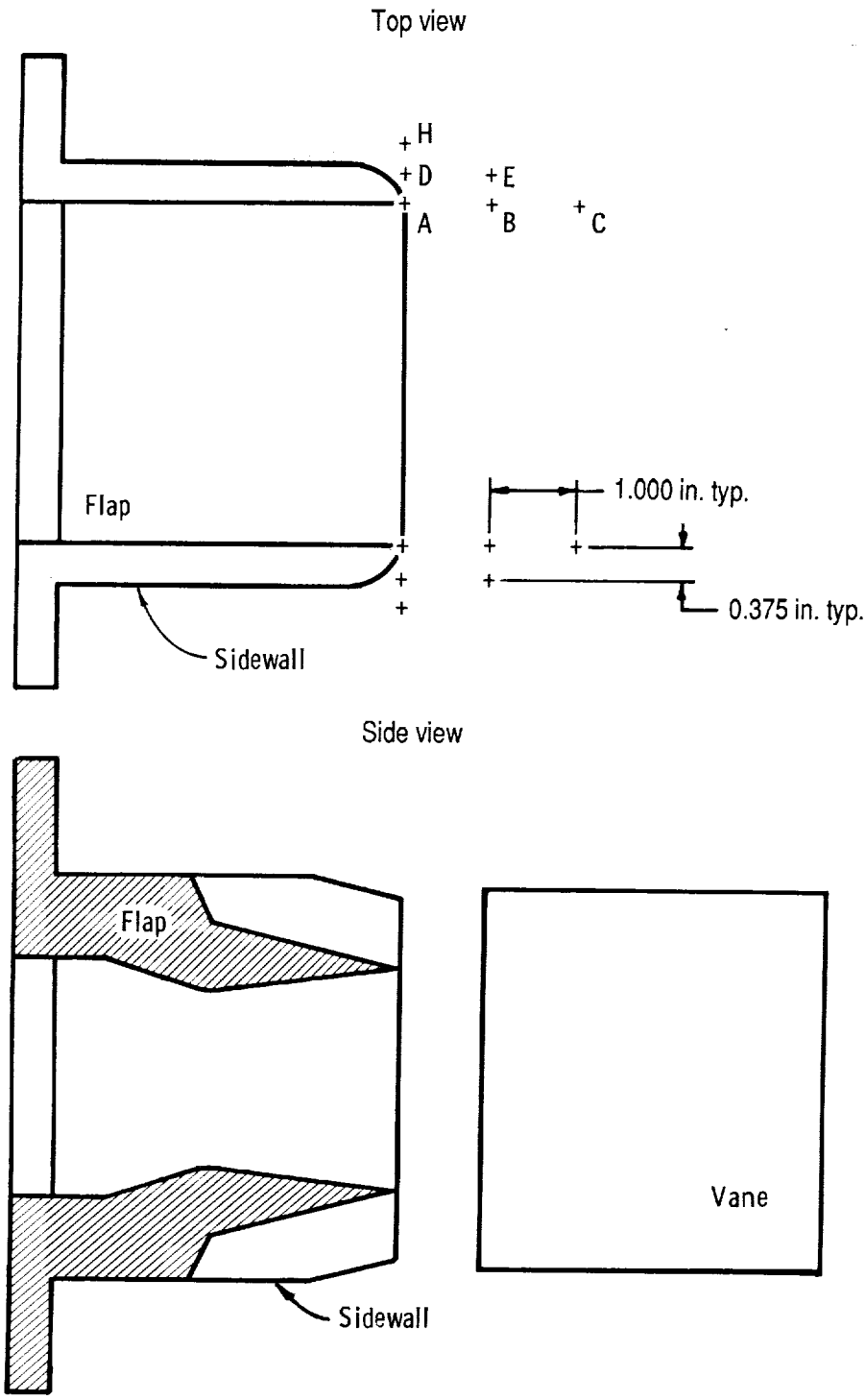

Installation on unvectored A/B power nozzle shown

(a) Vane location matrix.

Figure 7. Sketches of vane installation geometry. (All leading-edge locations are for unvectored vanes.)

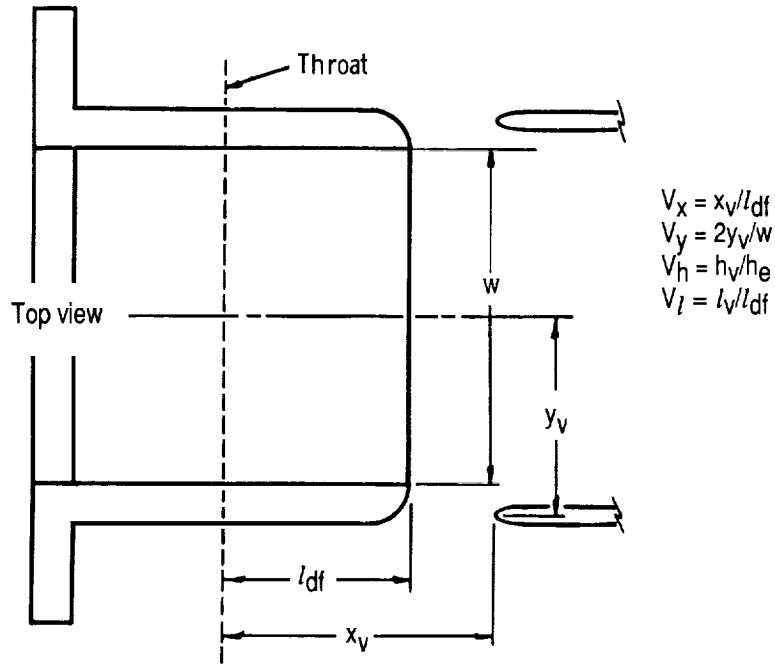

Nozzle	Vane location	x_v, in.	y_v, in.	V_x	V_y
Dry	A	2.275	2.000	1.000	1.0
	B	3.275	2.000	1.440	1.0
	C	4.275	2.000	1.879	1.0
	D	2.275	2.375	1.000	1.2
	E	3.275	2.375	1.440	1.2
	H	2.275	2.750	1.000	1.4
A/B	A	2.200	2.000	1.000	1.0
	B	3.200	2.000	1.455	1.0
	C	4.200	2.000	1.909	1.0
	D	2.200	2.375	1.000	1.2
	E	3.200	2.375	1.455	1.2
	H	2.200	2.750	1.000	1.4

Nozzle	Vane position	A_v / A_e	V_h	V_l
Dry	A	3.814	3.814	1.758
Dry	B	4.661	4.661	1.758
Dry	C	5.720	3.814	2.637
A/B	A	1.731	1.731	1.818
A/B	B	2.115	2.115	1.818
A/B	C	2.596	1.731	2.727

(b) Normalized vane parameters.

Figure 7. Concluded.

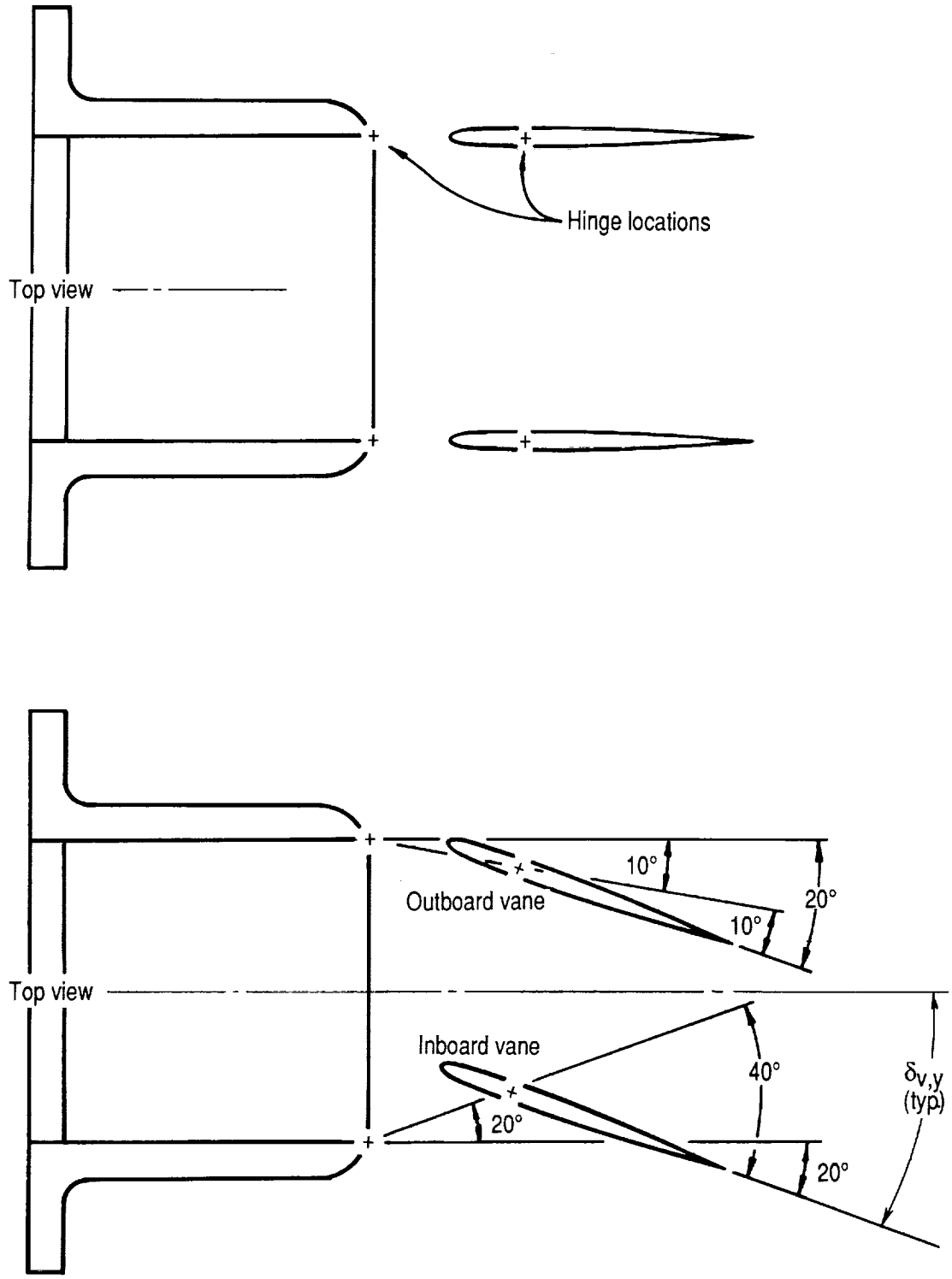

(a) Yaw-vectoring geometry. For 10° vane deflection, divide all angles by 2.

Figure 8. Sketches of double-hinged vanes.

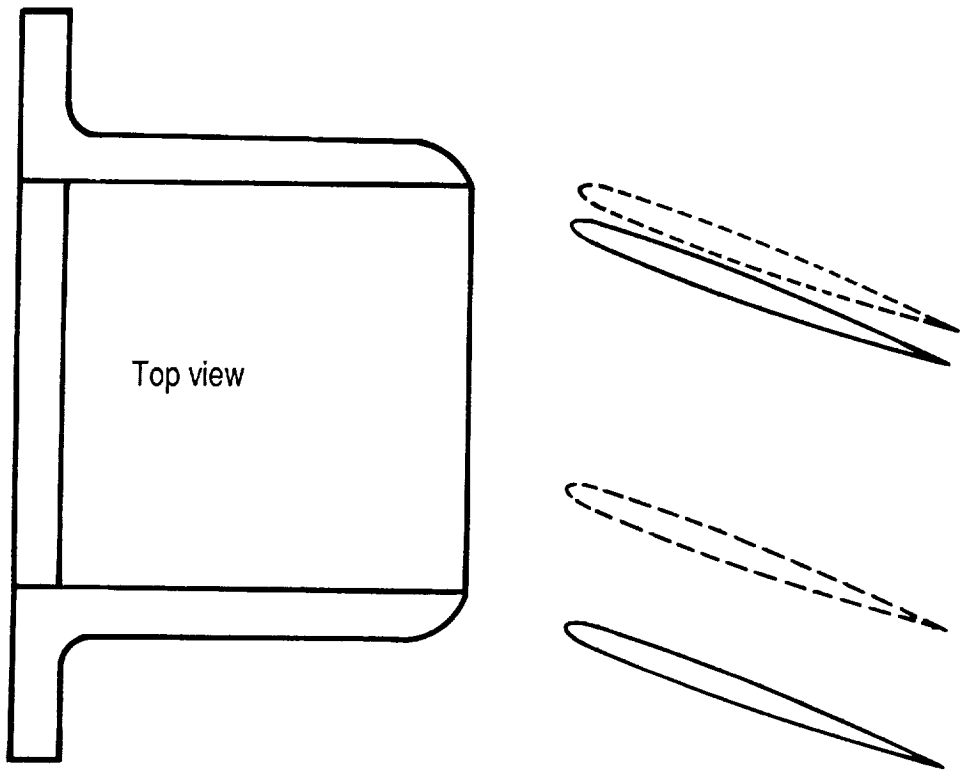

(b) Relative locations of single-hinged (solid lines) and double-hinged (dashed lines) vanes.

Figure 8. Concluded.

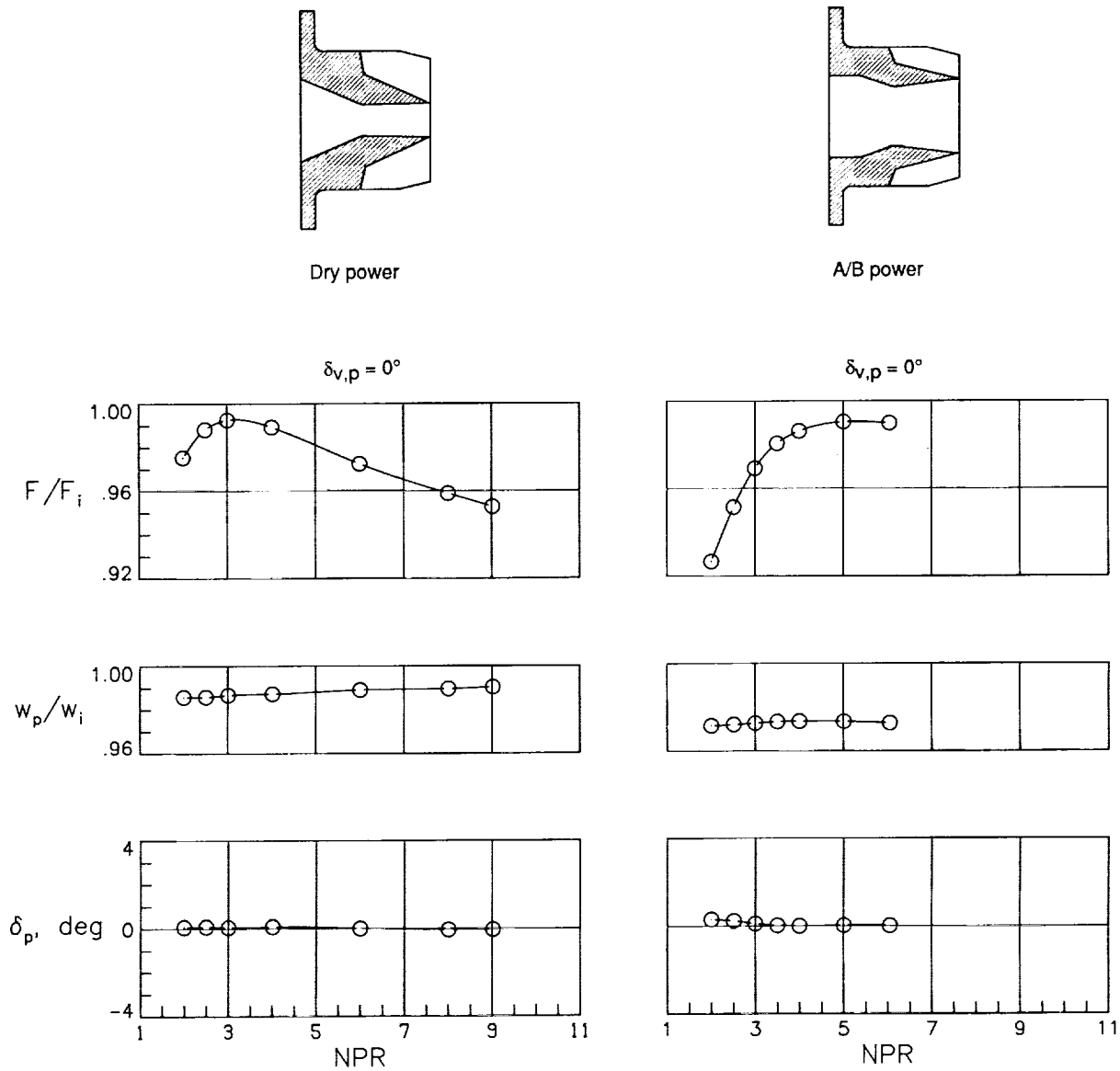

(a) Unvectored.

Figure 9. Baseline nozzle performance.

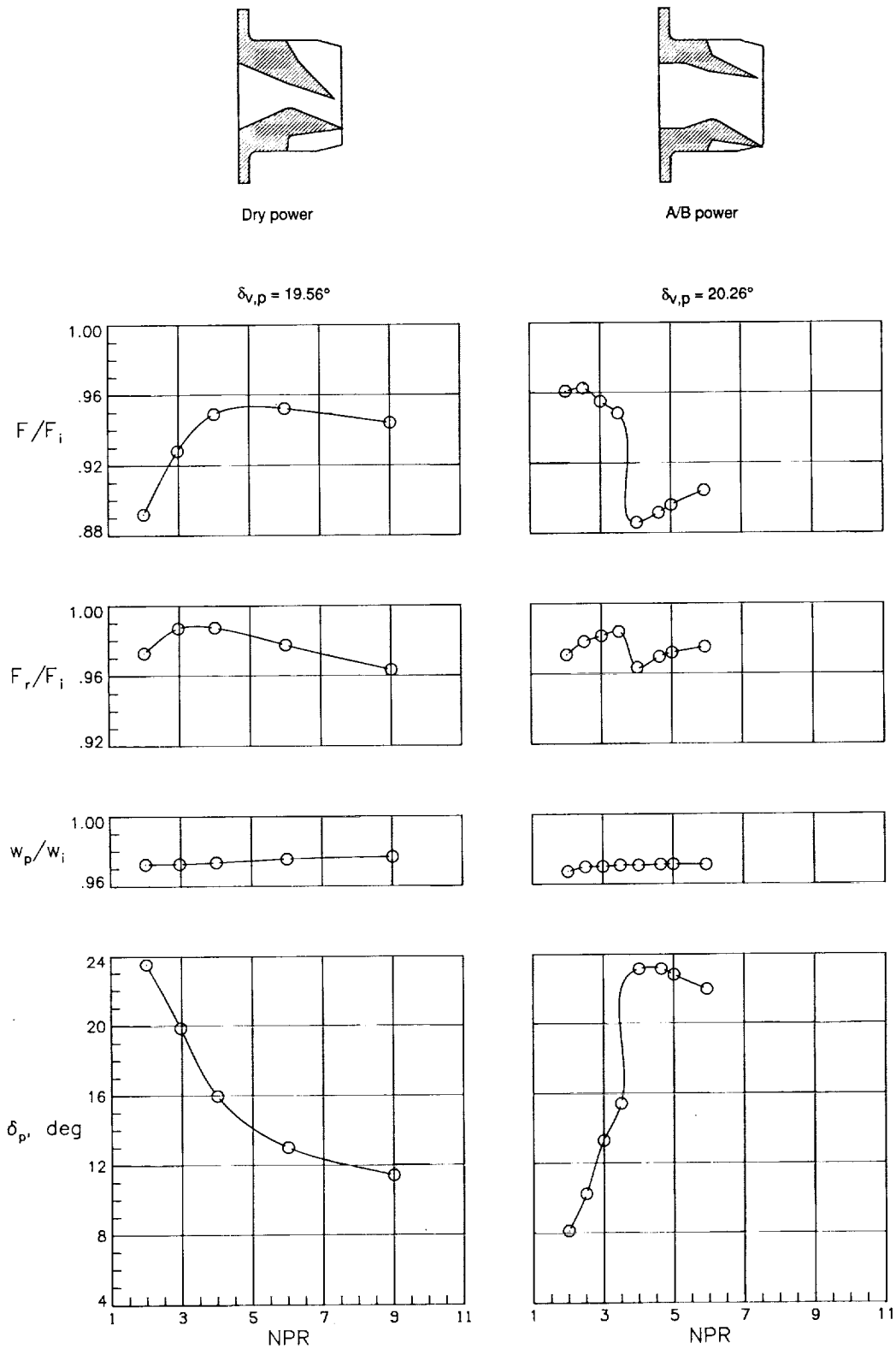

(b) Vectored.

Figure 9. Concluded.

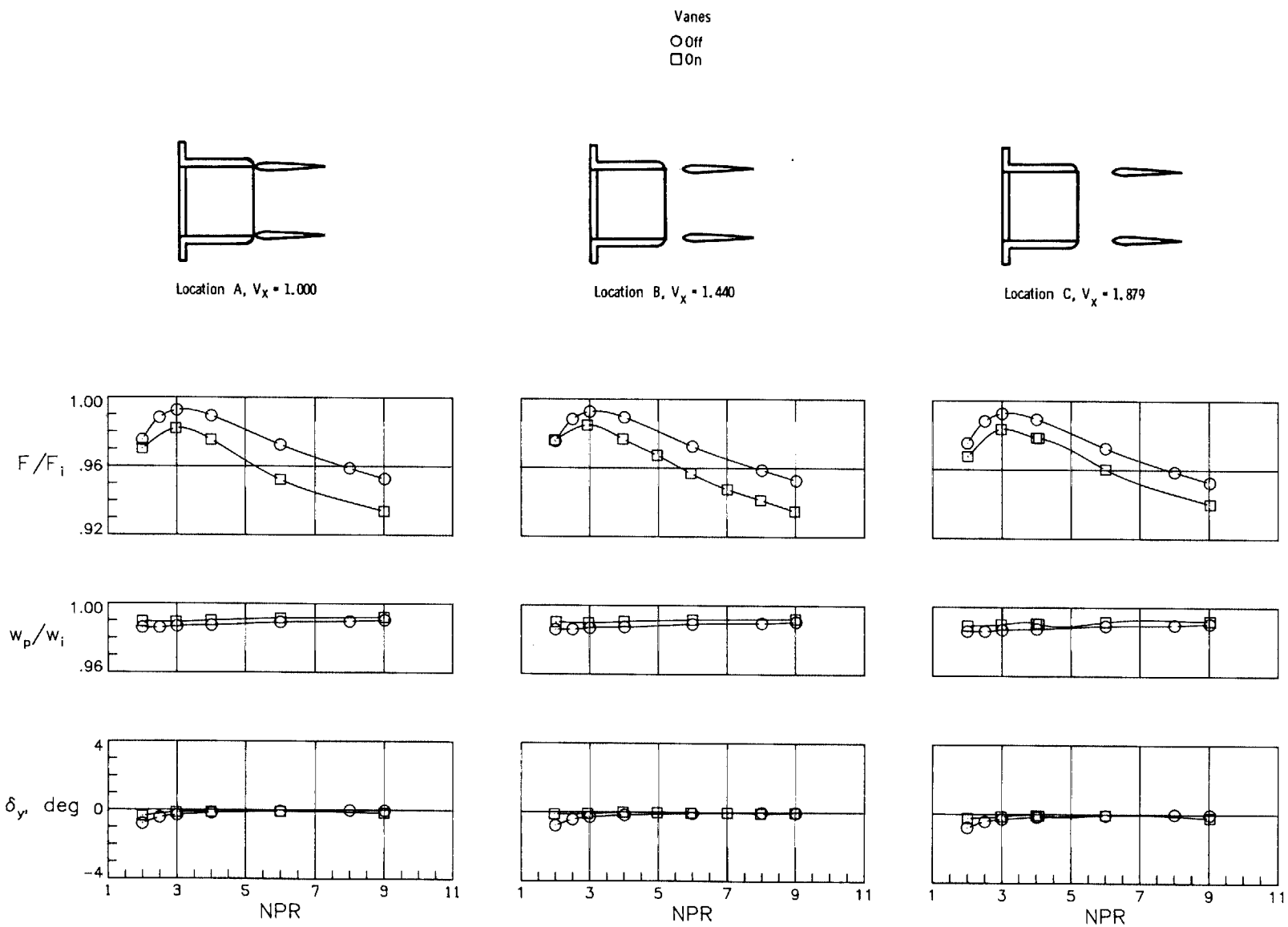

(a) $\delta_{v,y} = 0°$.

Figure 10. Effect of vane longitudinal position for size A vanes with $\delta_{v,p} = 0°$, dry-power nozzle, and $V_y = 1.00$.

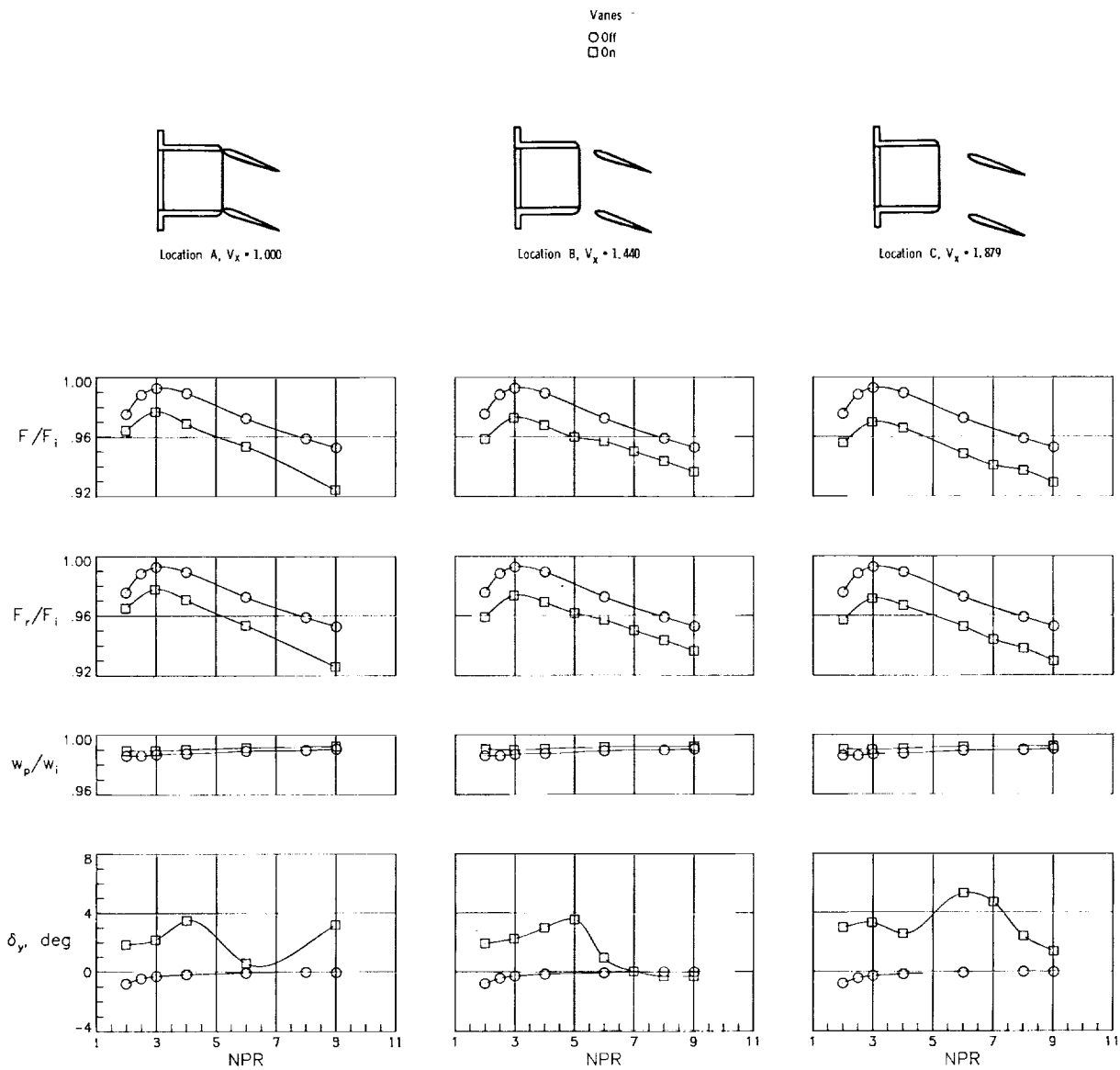

(b) $\delta_{v,y} = 10°$.

Figure 10. Continued.

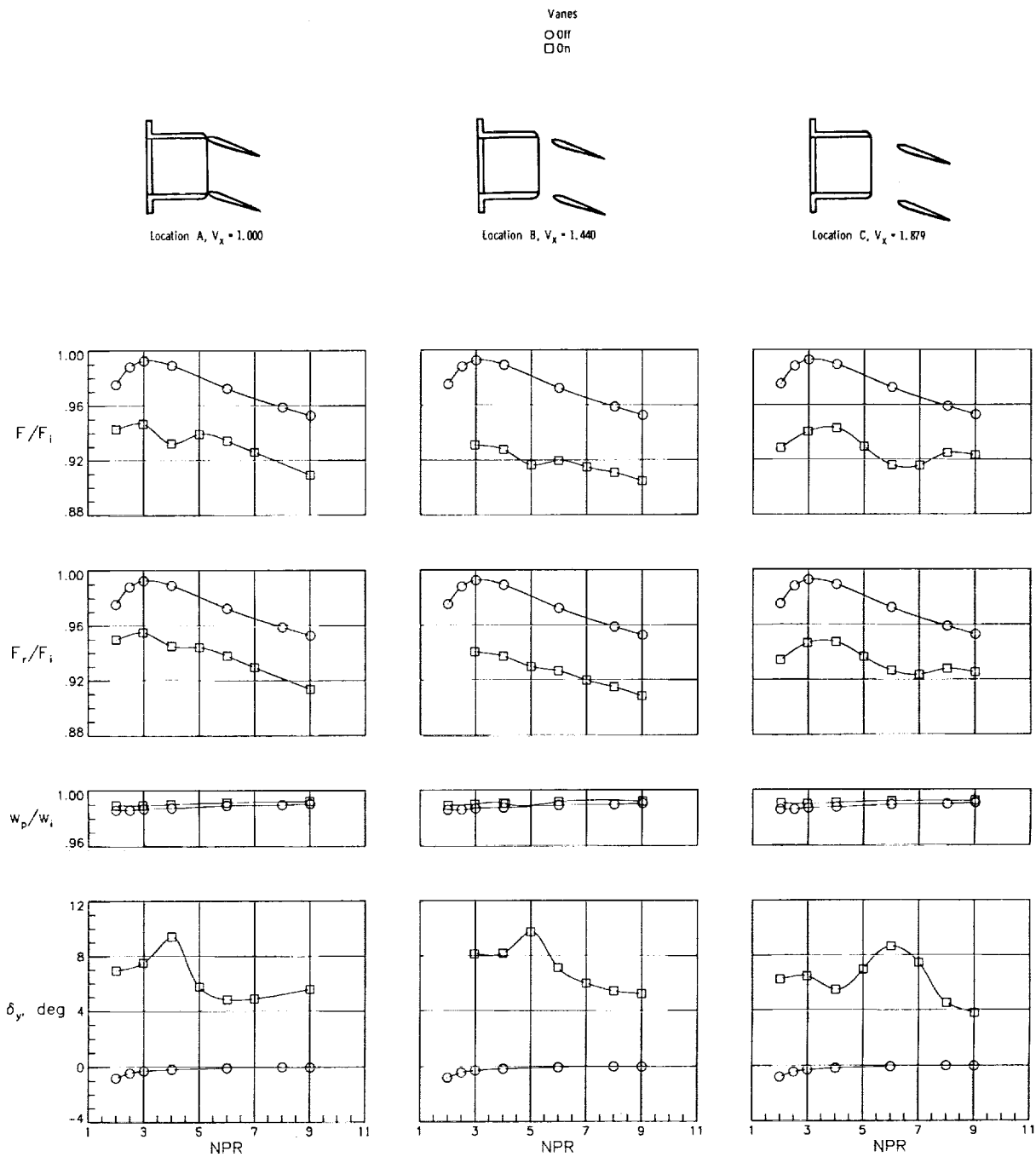

(c) $\delta_{v,y} = 20°$.

Figure 10. Concluded.

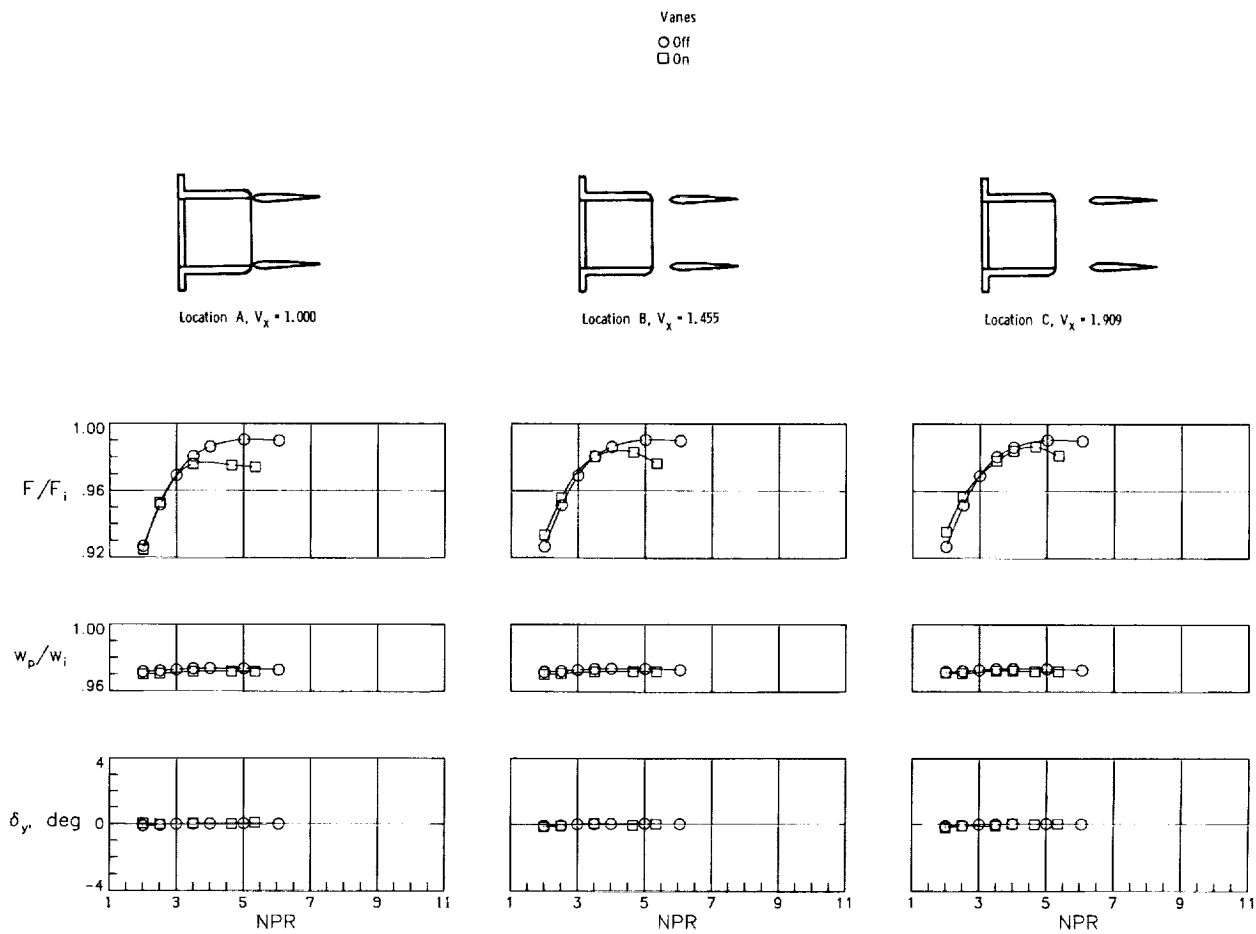

(a) $\delta_{v,y} = 0°$.

Figure 11. Effect of vane longitudinal position for size A vanes with $\delta_{v,p} = 0°$, A/B power nozzle, and $V_y = 1.00$.

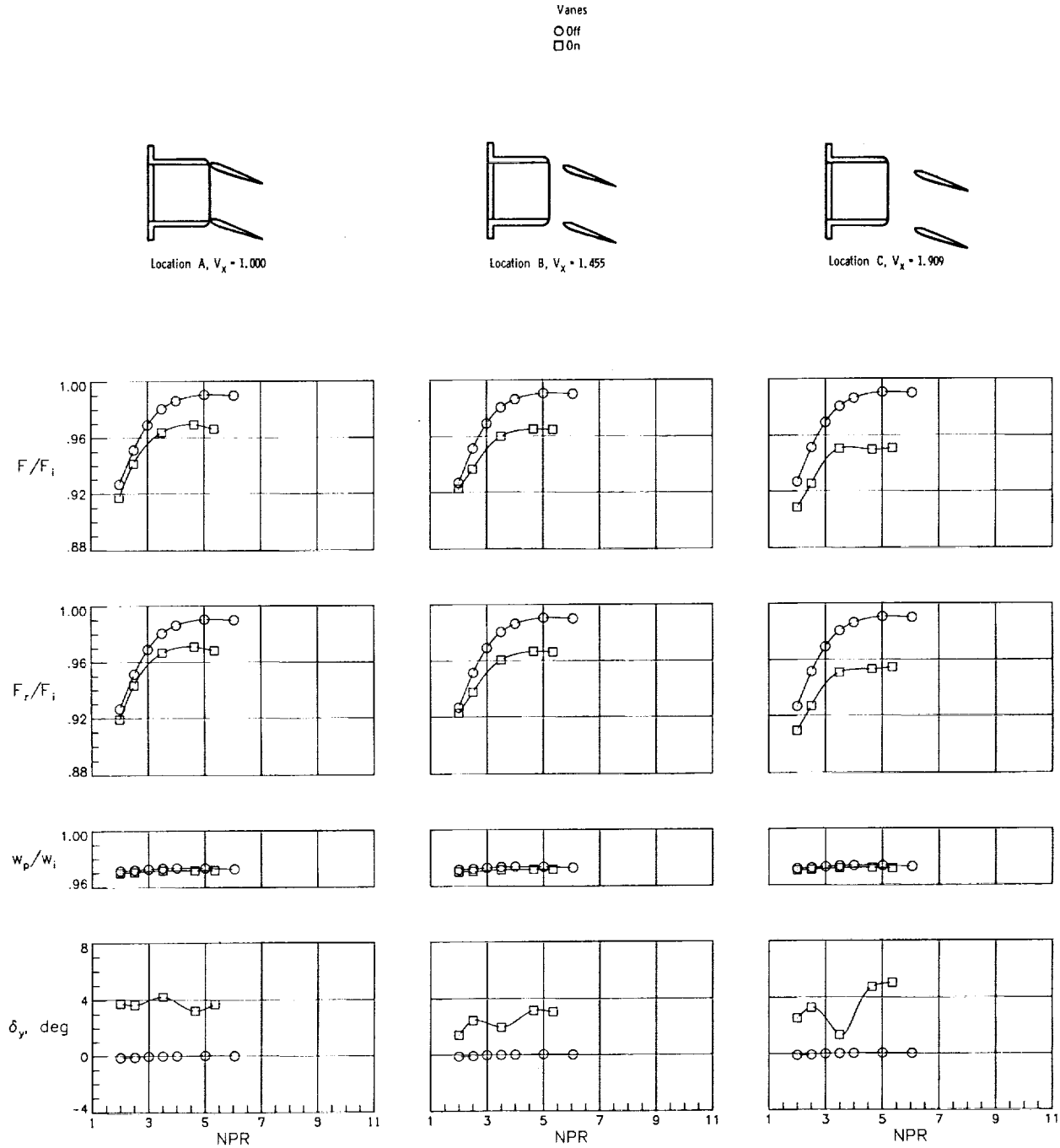

(b) $\delta_{v,y} = 10°$.

Figure 11. Continued.

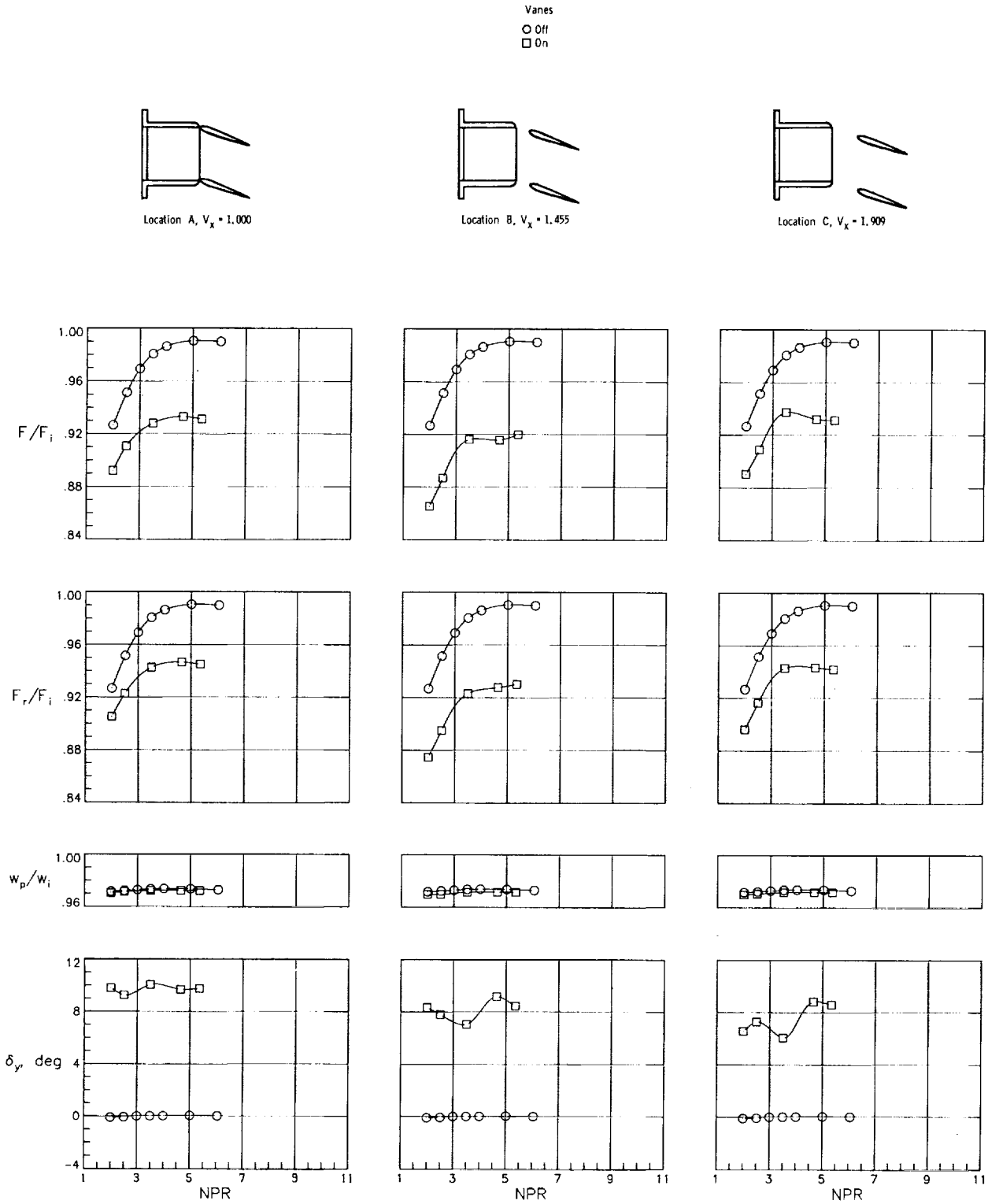

(c) $\delta_{v,y} = 20°$.

Figure 11. Concluded.

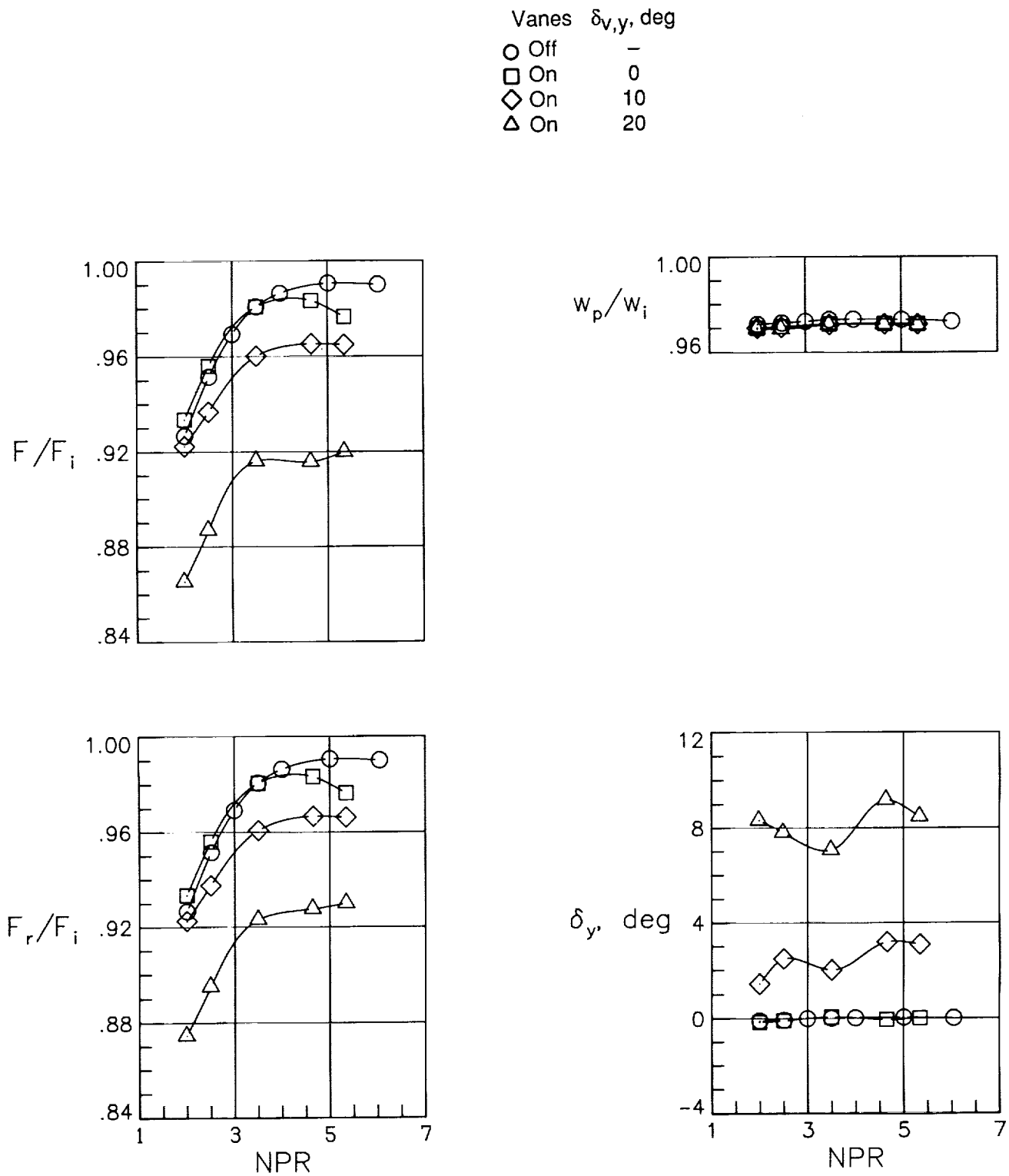

Figure 12. Effect of vane installation and yaw angle on performance of A/B power nozzle with $\delta_{v,p} = 0°$ for size A vanes at $V_x = 1.455$ and $V_y = 1.00$.

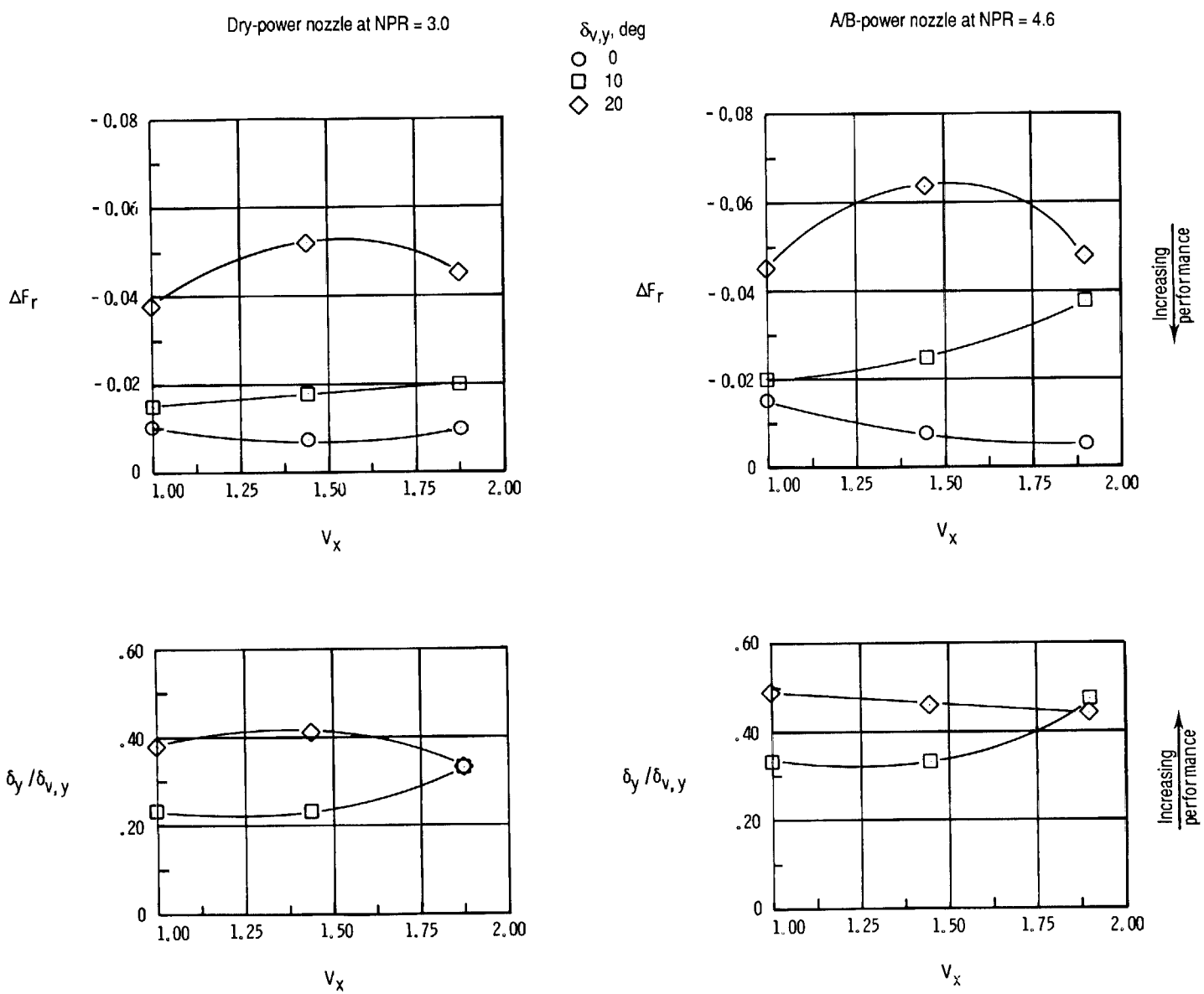

Figure 13. Effect of vane longitudinal position and yaw angle on nozzle performance and turning efficiency for unvectored nozzle with size A vanes and $V_y = 1.00$.

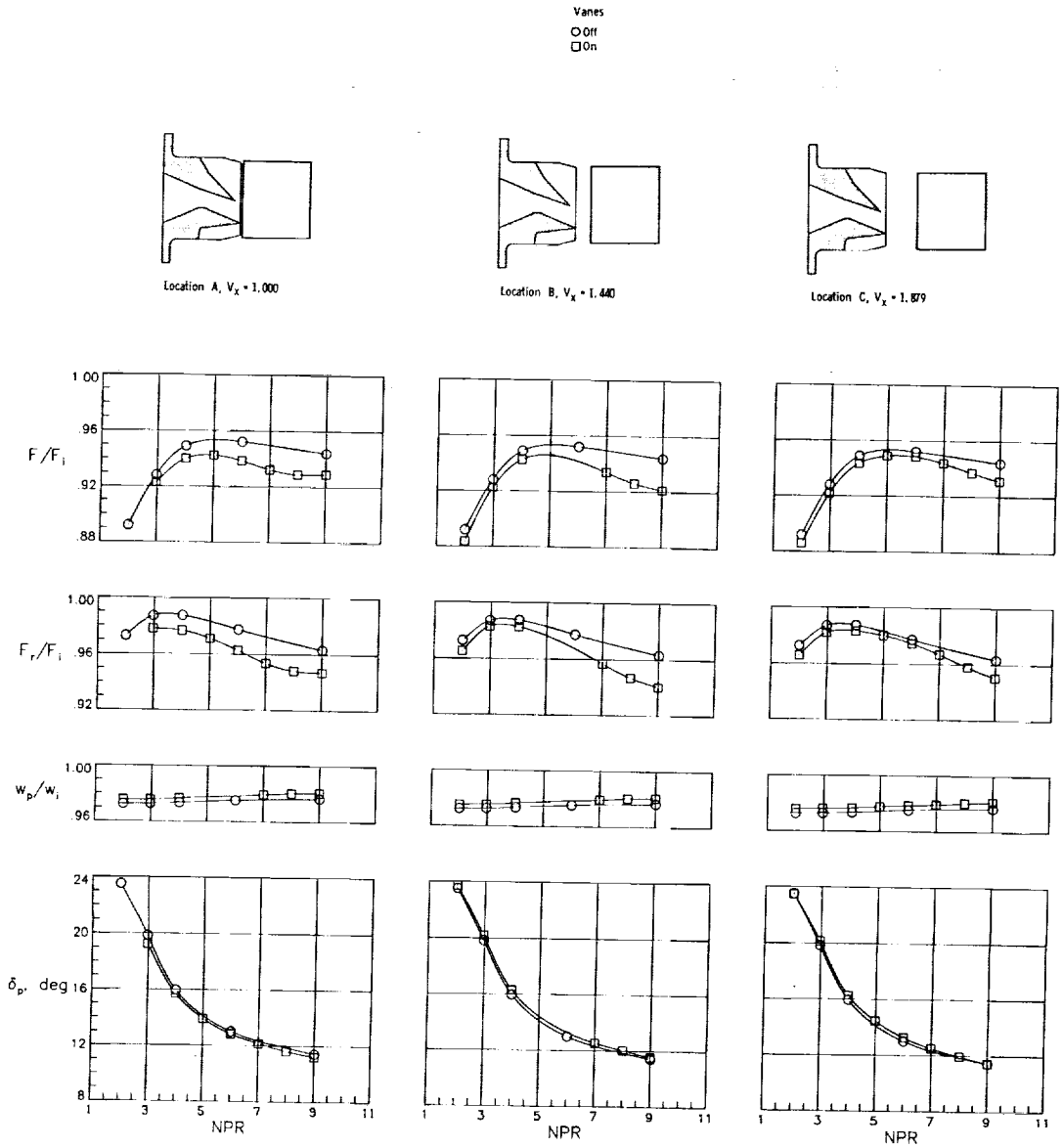

(a) $\delta_{v,y} = 0°$.

Figure 14. Effect of vane longitudinal position for size A vanes with $\delta_{v,p} = 19.56°$, dry-power nozzle, and $V_y = 1.00$.

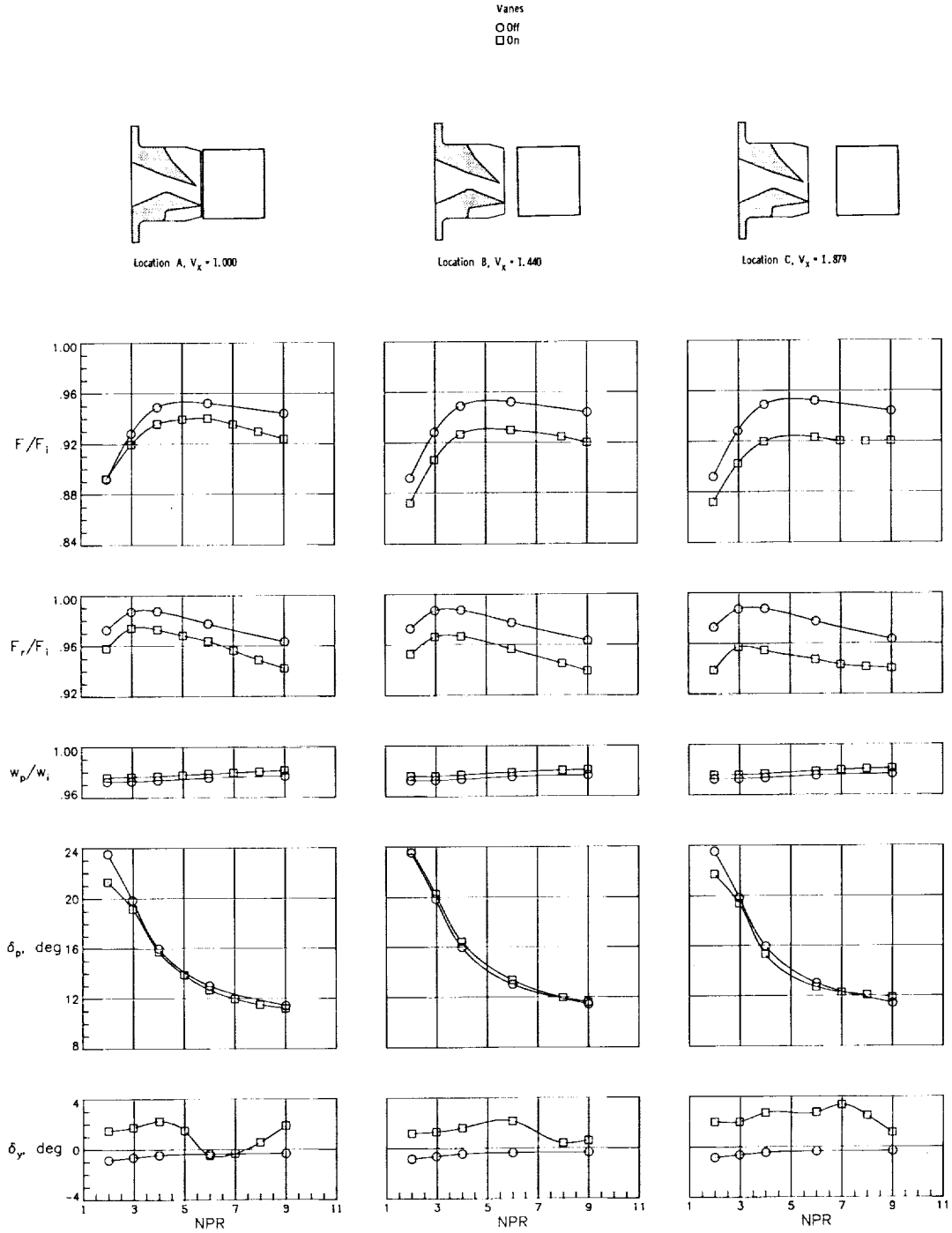

(b) $\delta_{v,y} = 10°$.

Figure 14. Continued.

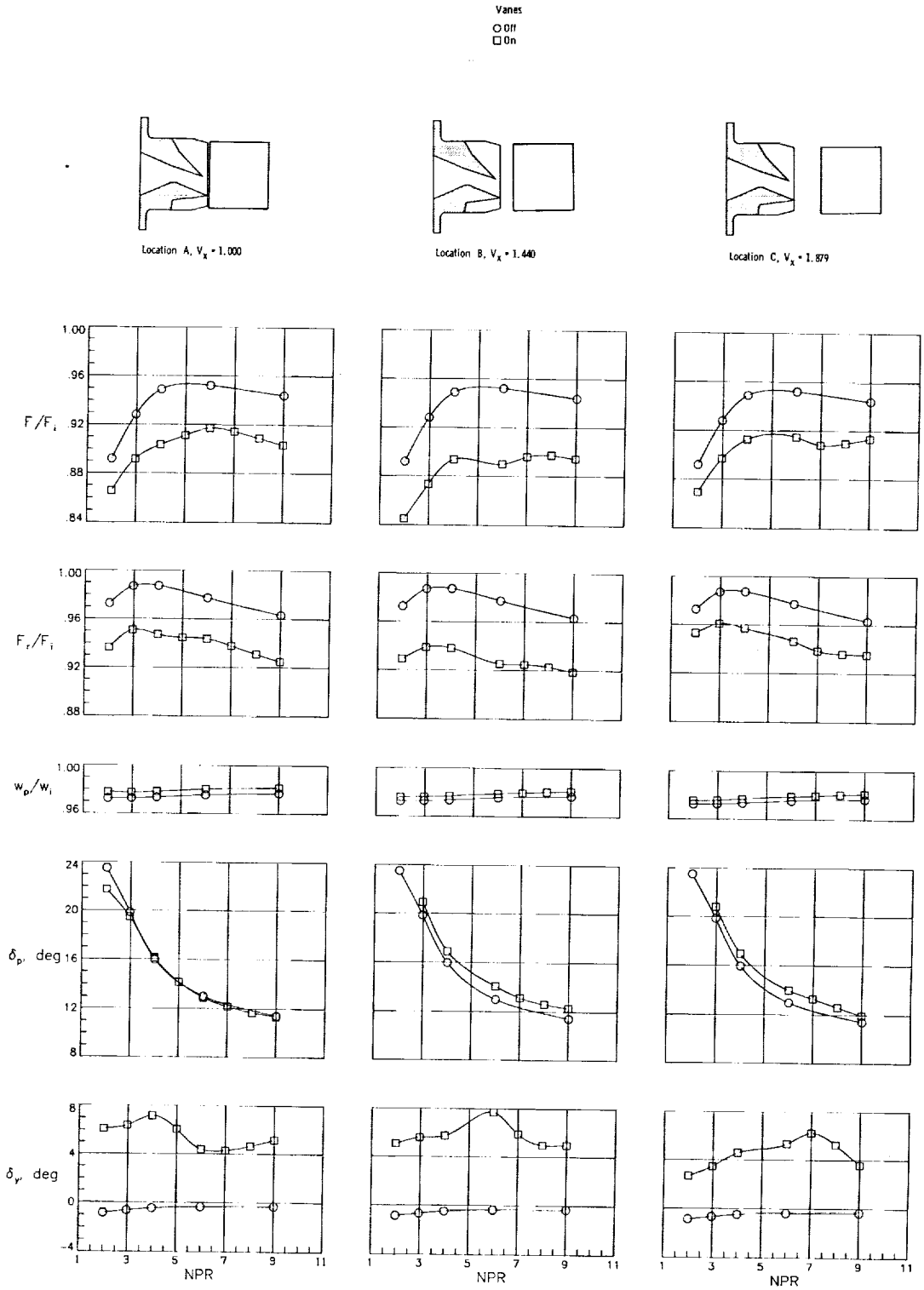

(c) $\delta_{v,y} = 20°$.

Figure 14. Concluded.

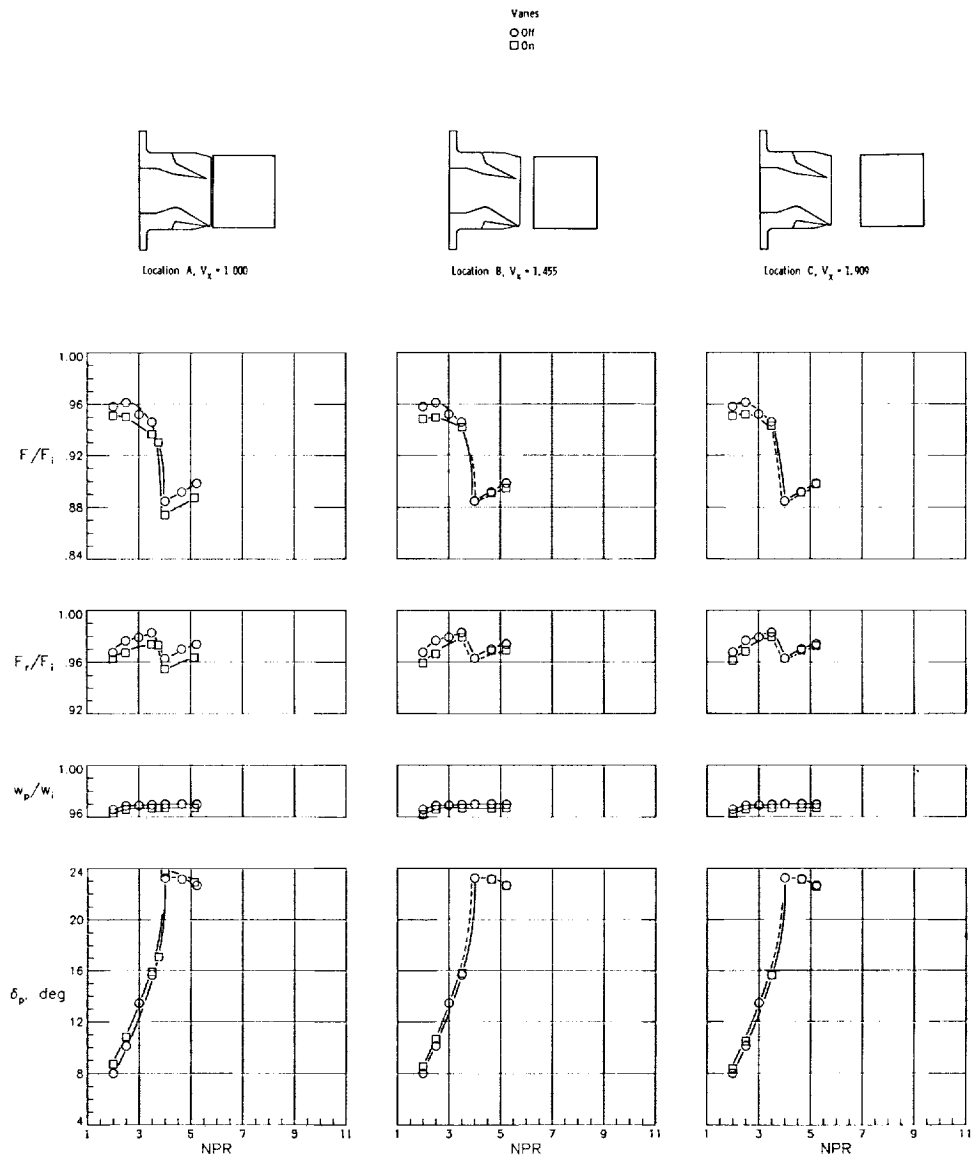

(a) $\delta_{v,y} = 0°$.

Figure 15. Effect of vane longitudinal position for size A vanes with $\delta_{v,p} = 20.26°$, A/B power nozzle, and $V_y = 1.00$.

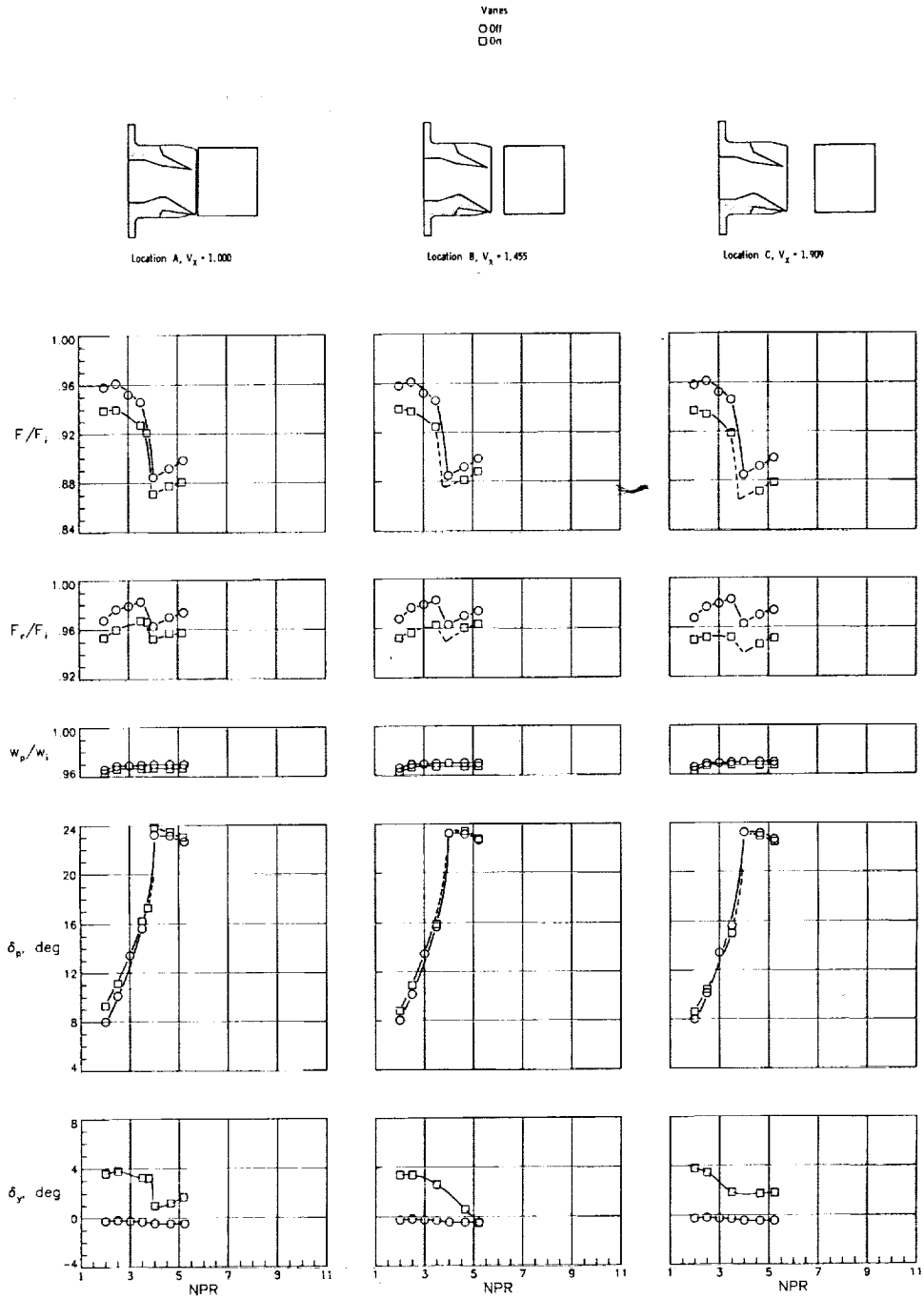

(b) $\delta_{v,y} = 10°$.

Figure 15. Continued.

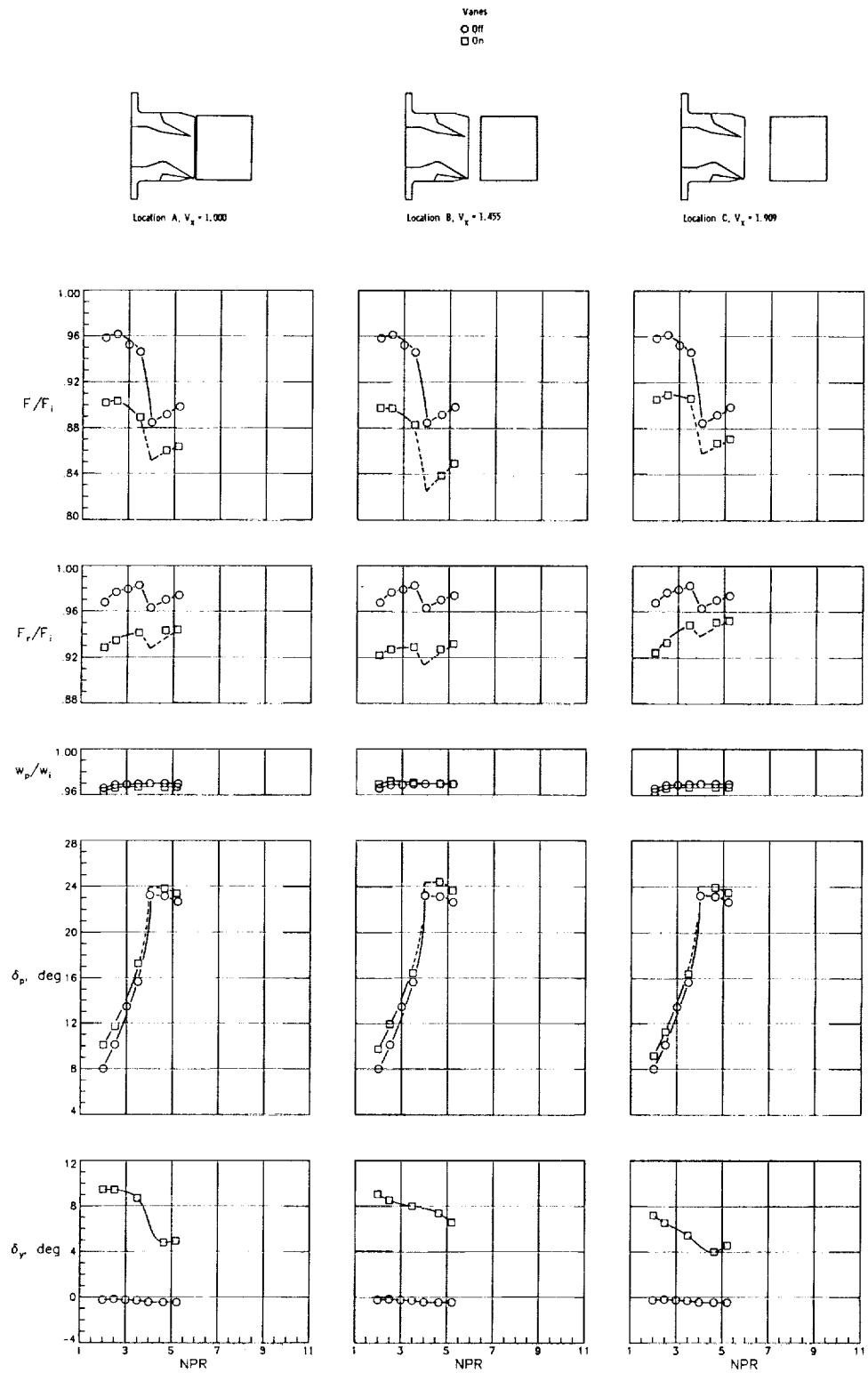

(c) $\delta_{v,y} = 20°$.

Figure 15. Concluded.

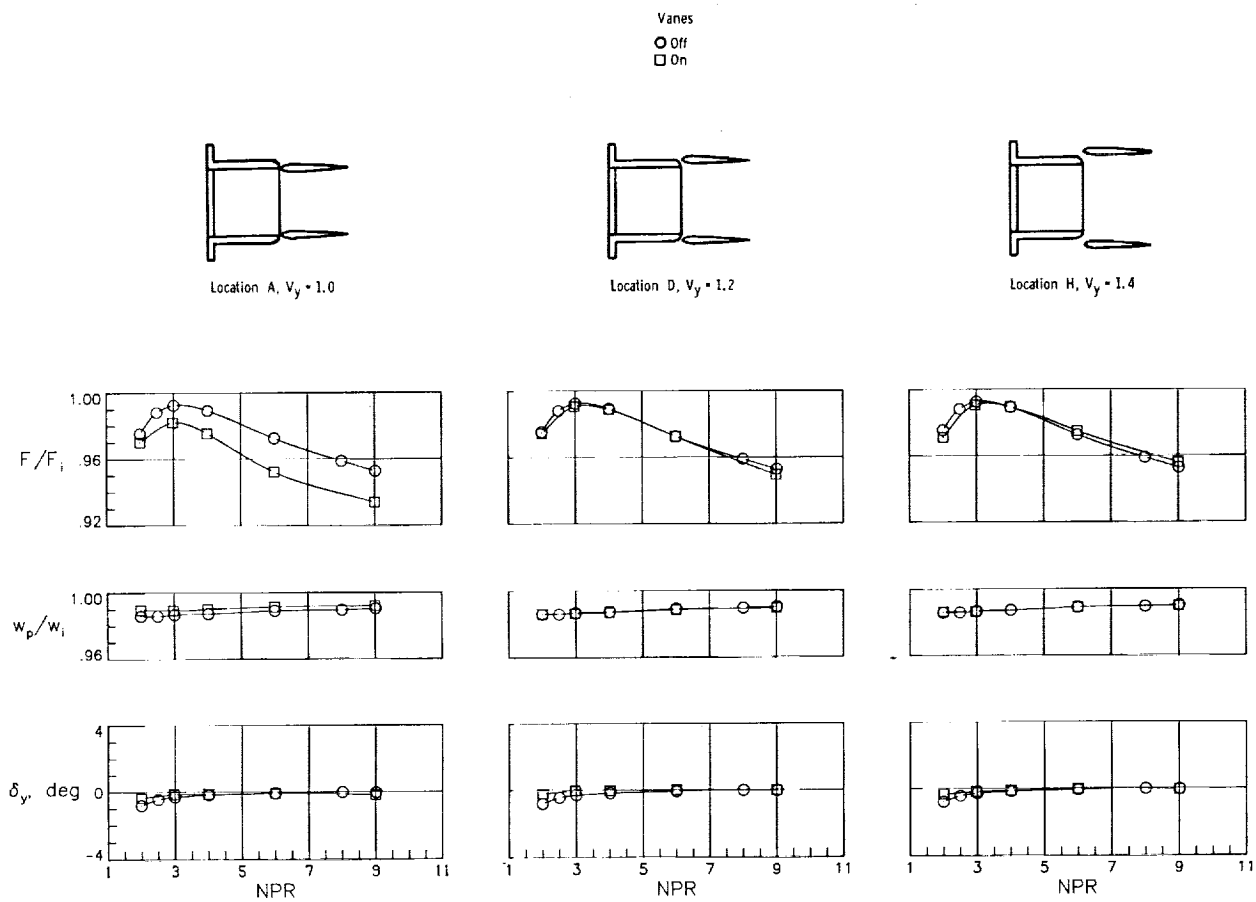

(a) $\delta_{v,y} = 0°$.

Figure 16. Effect of vane lateral position for size A vanes with $\delta_{v,p} = 0°$, dry-power nozzle, and $V_x = 1.000$.

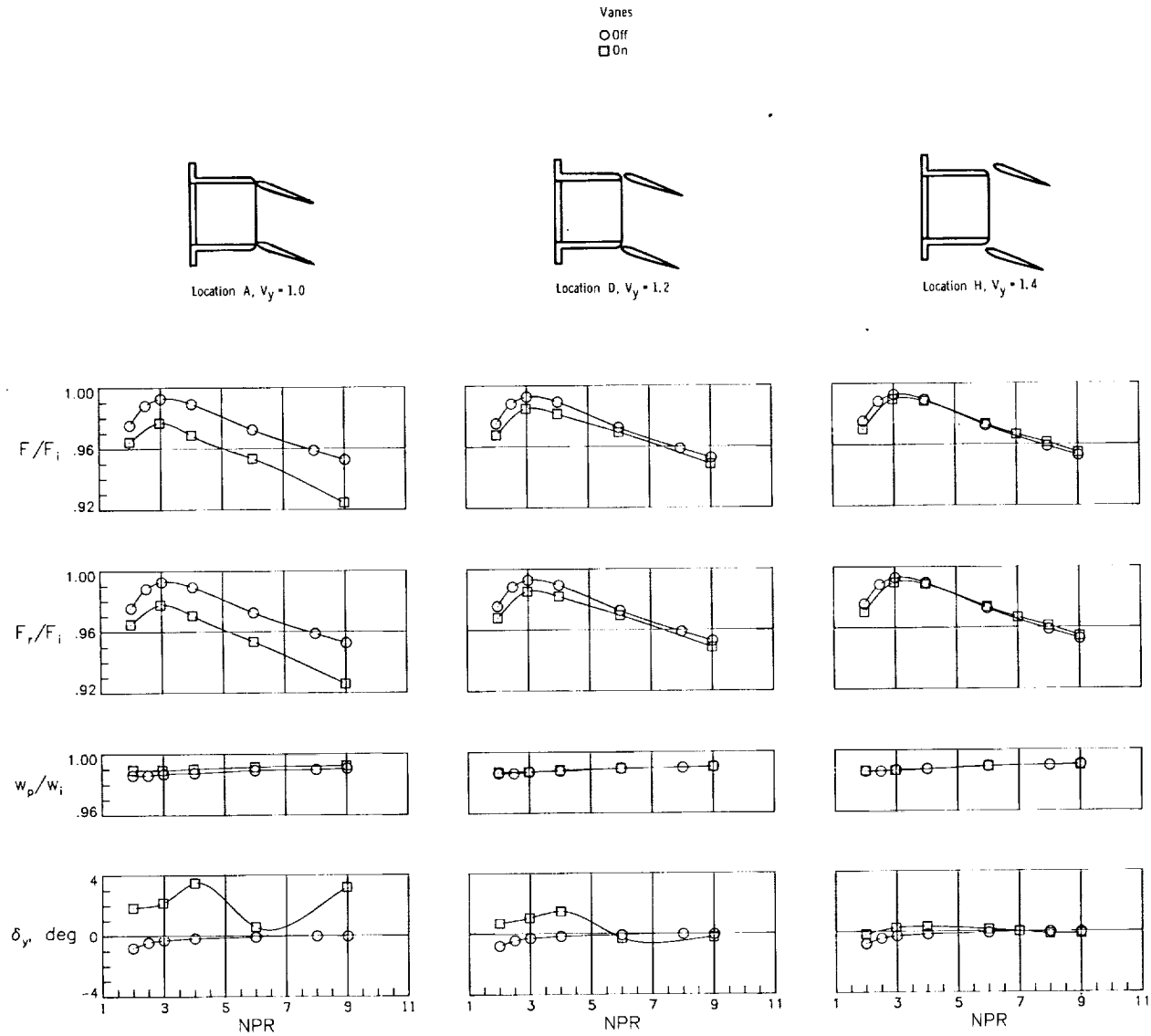

(b) $\delta_{v,y} = 10°$.

Figure 16. Continued.

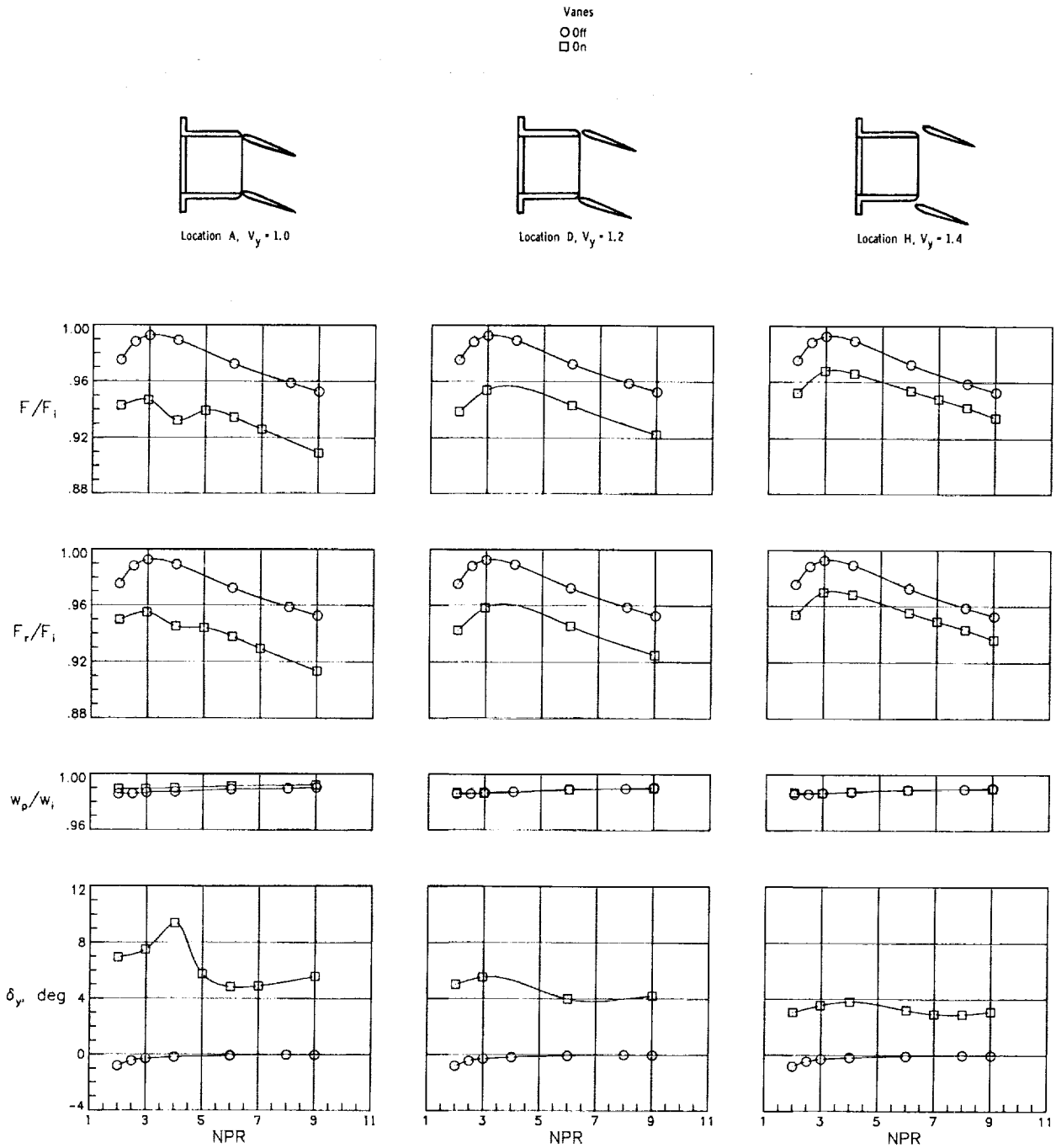

(c) $\delta_{v,y} = 20°$.

Figure 16. Concluded.

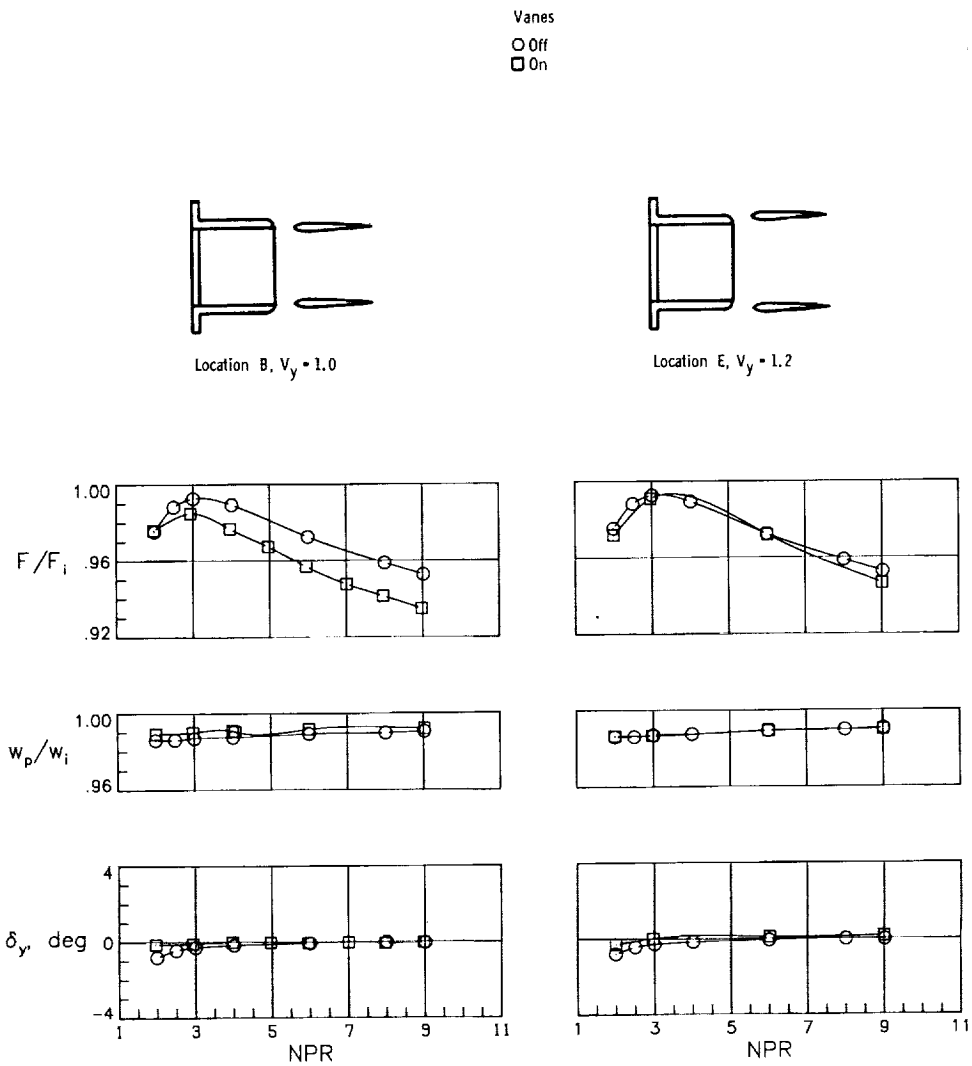

(a) $\delta_{v,y} = 0°$.

Figure 17. Effect of vane lateral position for size A vanes with $\delta_{v,p} = 0°$, dry-power nozzle, and $V_x = 1.440$.

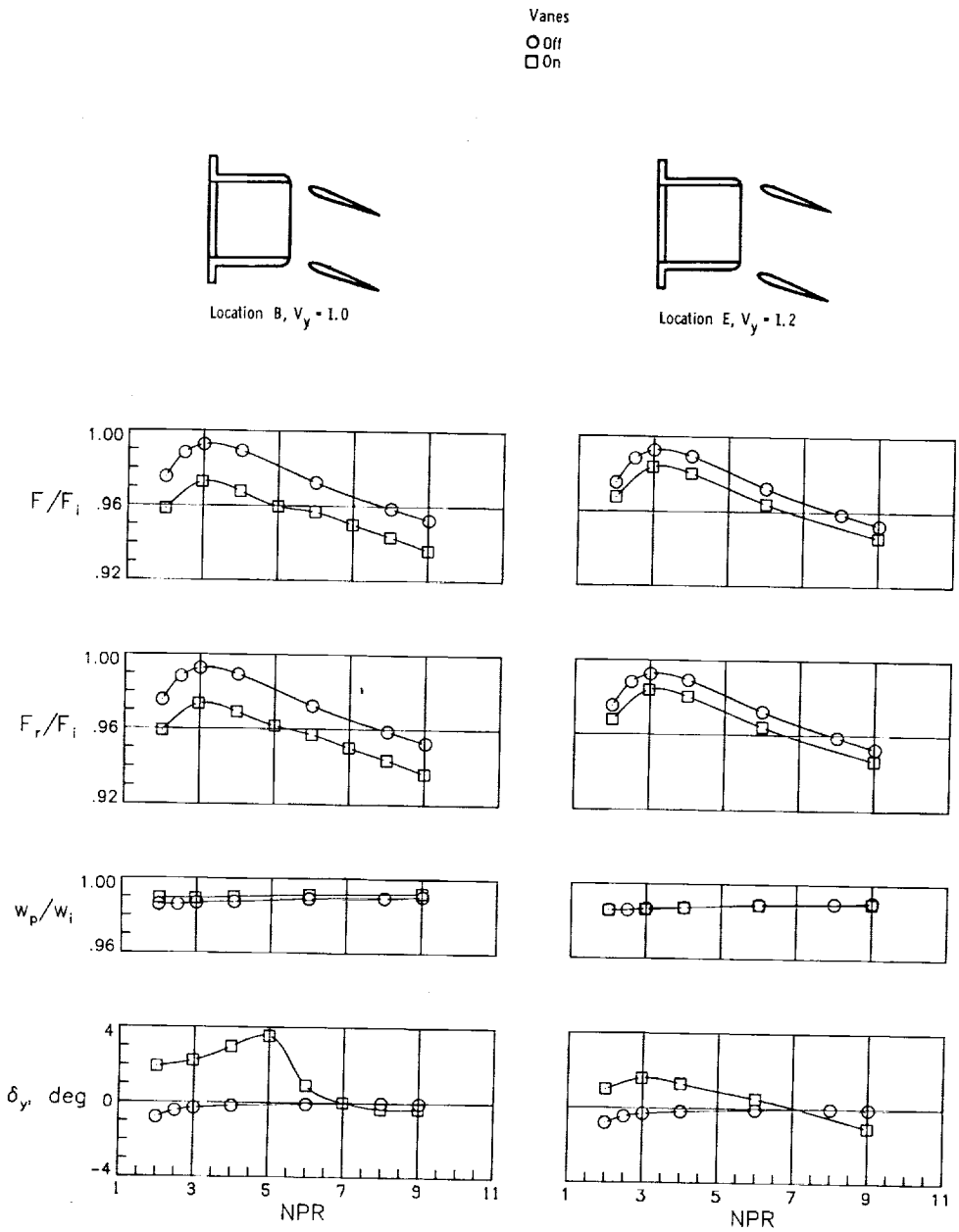

(b) $\delta_{v,y} = 10°$.

Figure 17. Continued.

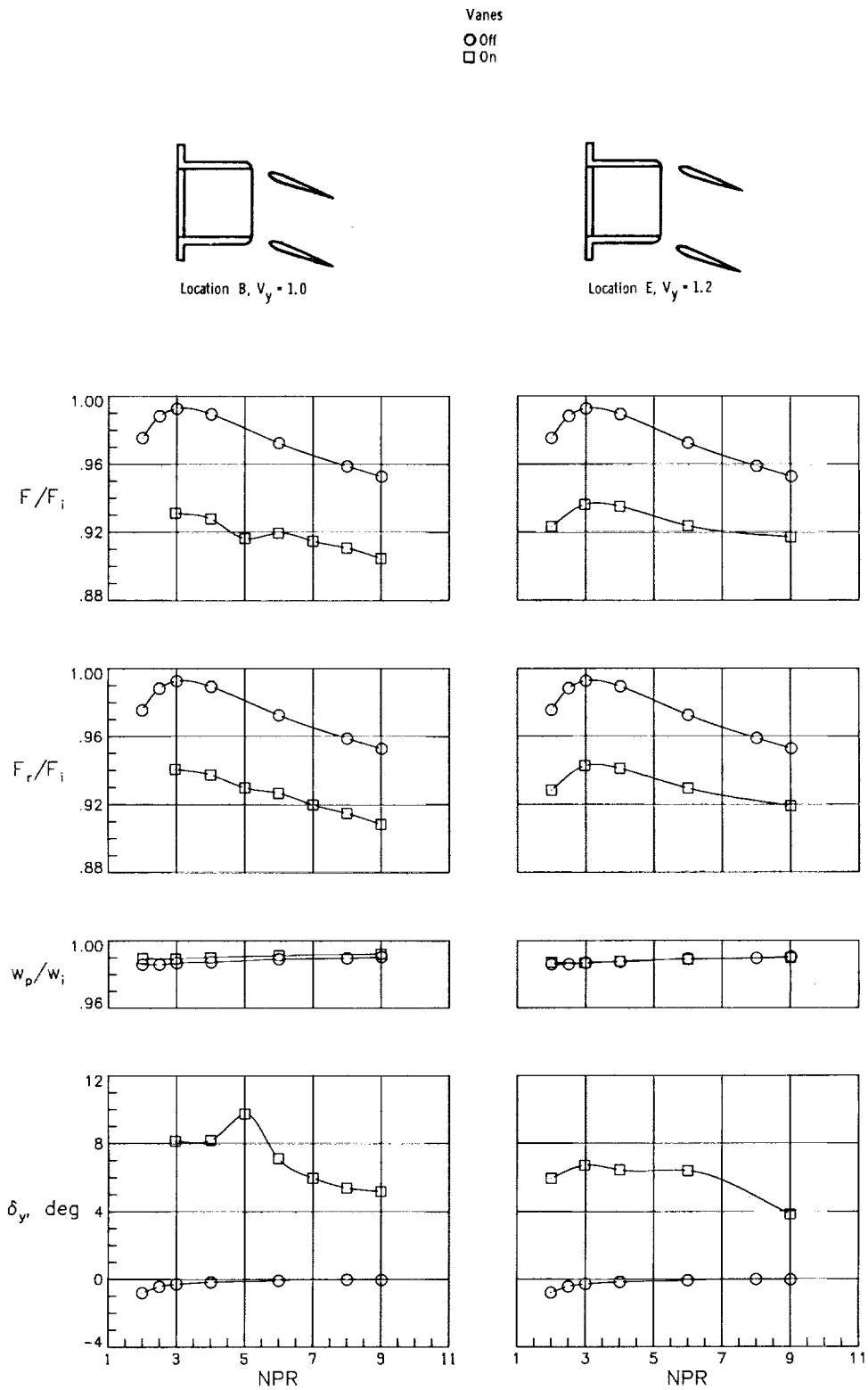

(c) $\delta_{v,y} = 20°$.

Figure 17. Concluded.

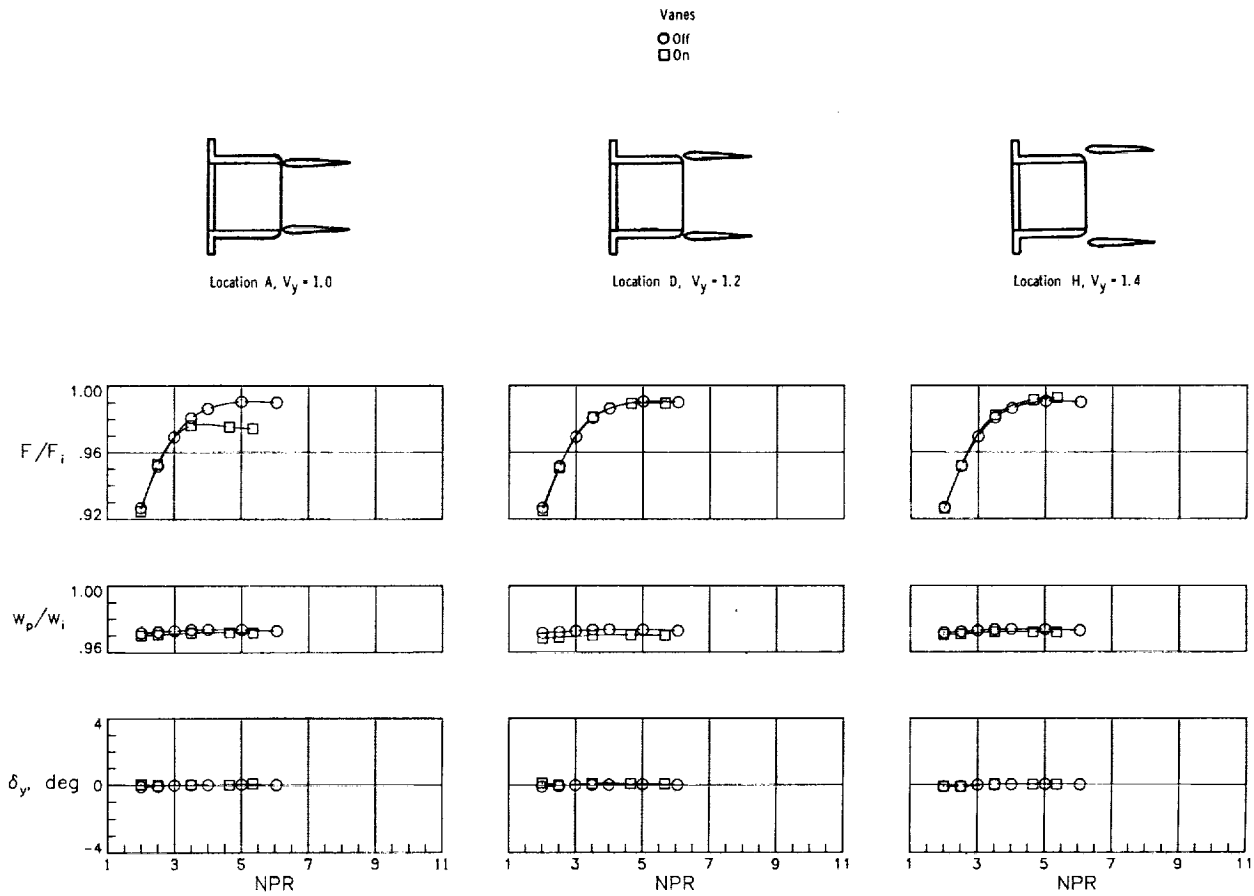

(a) $\delta_{v,y} = 0°$.

Figure 18. Effect of vane lateral position for size A vanes with $\delta_{v,p} = 0°$, A/B power nozzle, and $V_x = 1.000$.

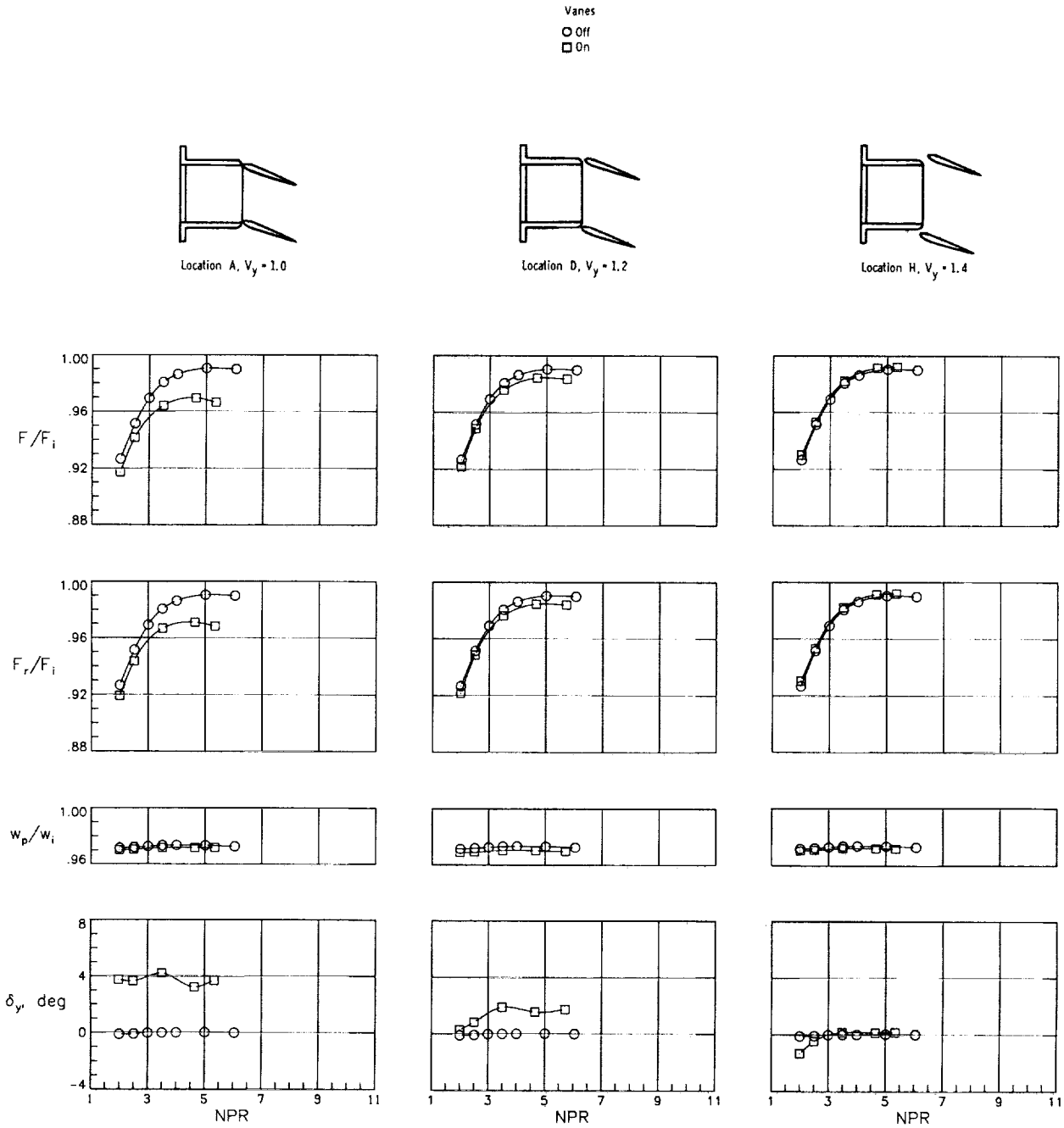

(b) $\delta_{v,y} = 10°$.

Figure 18. Continued.

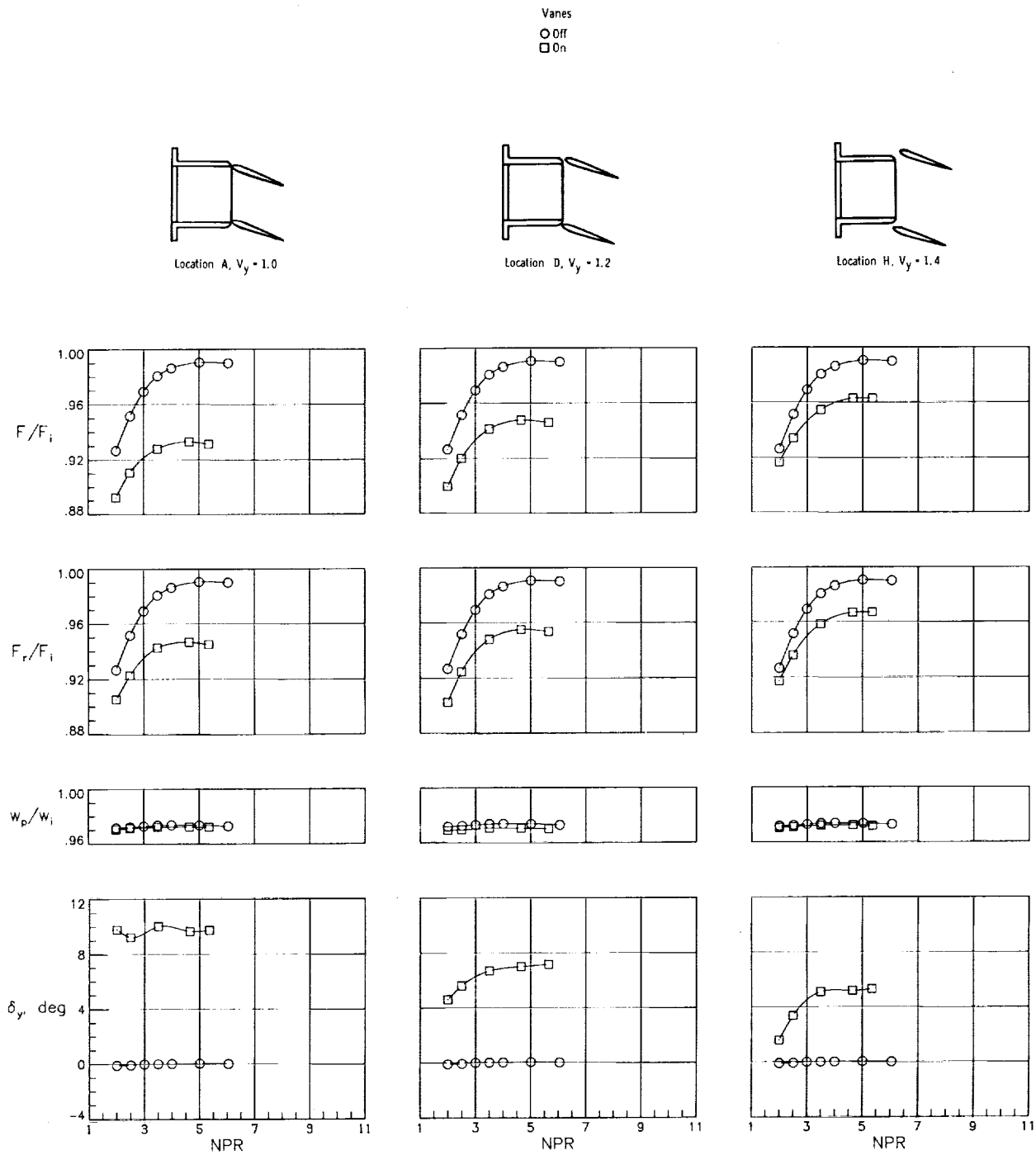

(c) $\delta_{v,y} = 20°$.

Figure 18. Concluded.

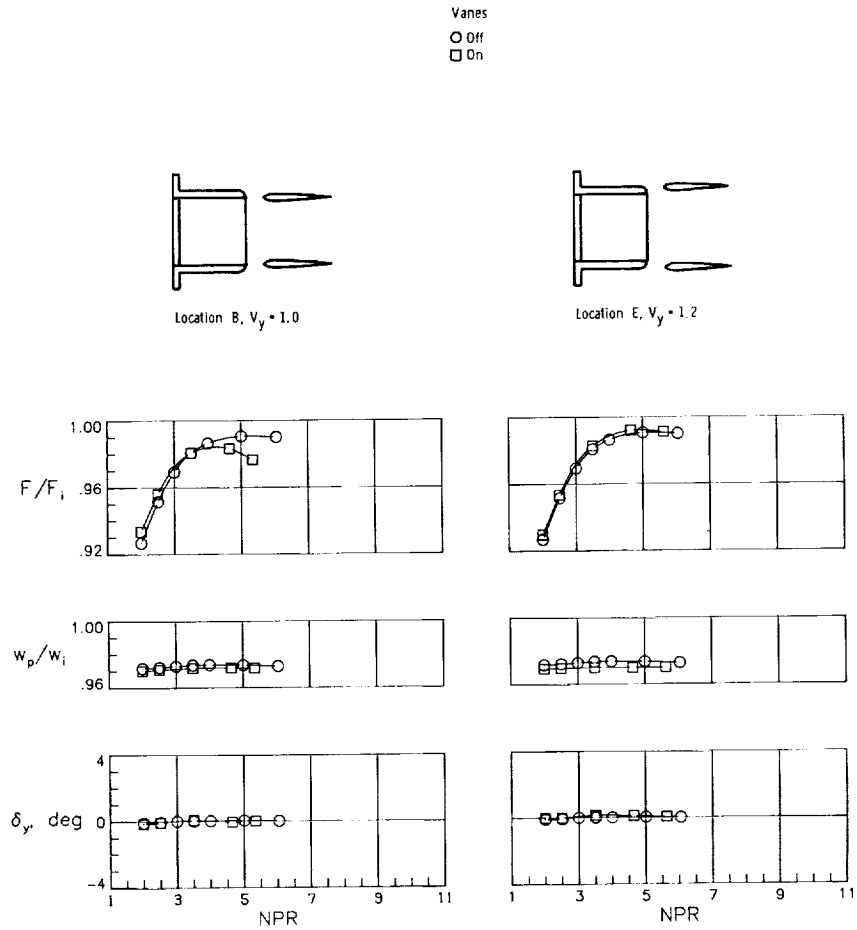

(a) $\delta_{v,y} = 0°$.

Figure 19. Effect of vane lateral position for size A vanes with $\delta_{v,p} = 0°$, A/B power nozzle, and $V_x = 1.455$.

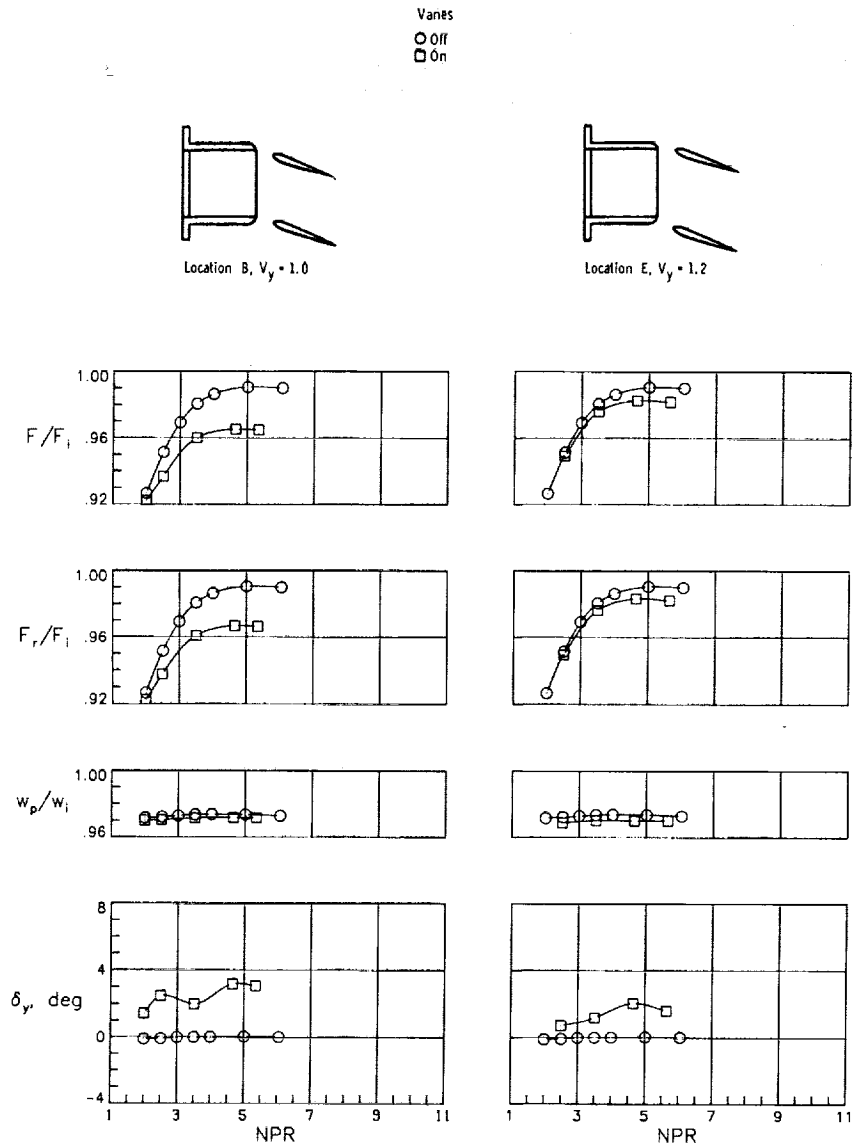

(b) $\delta_{v,y} = 10°$.

Figure 19. Continued.

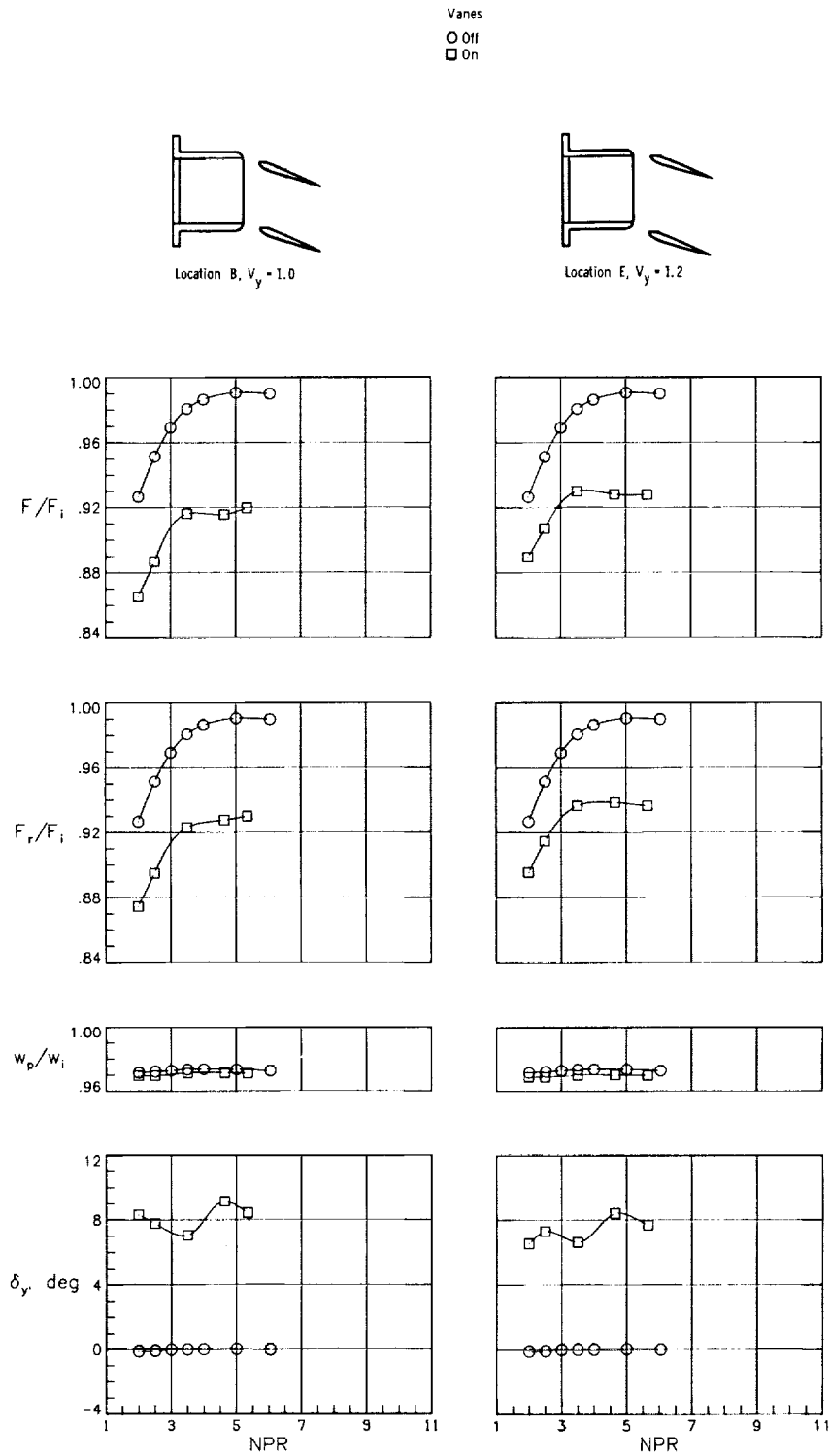

(c) $\delta_{v,y} = 20°$.

Figure 19. Concluded.

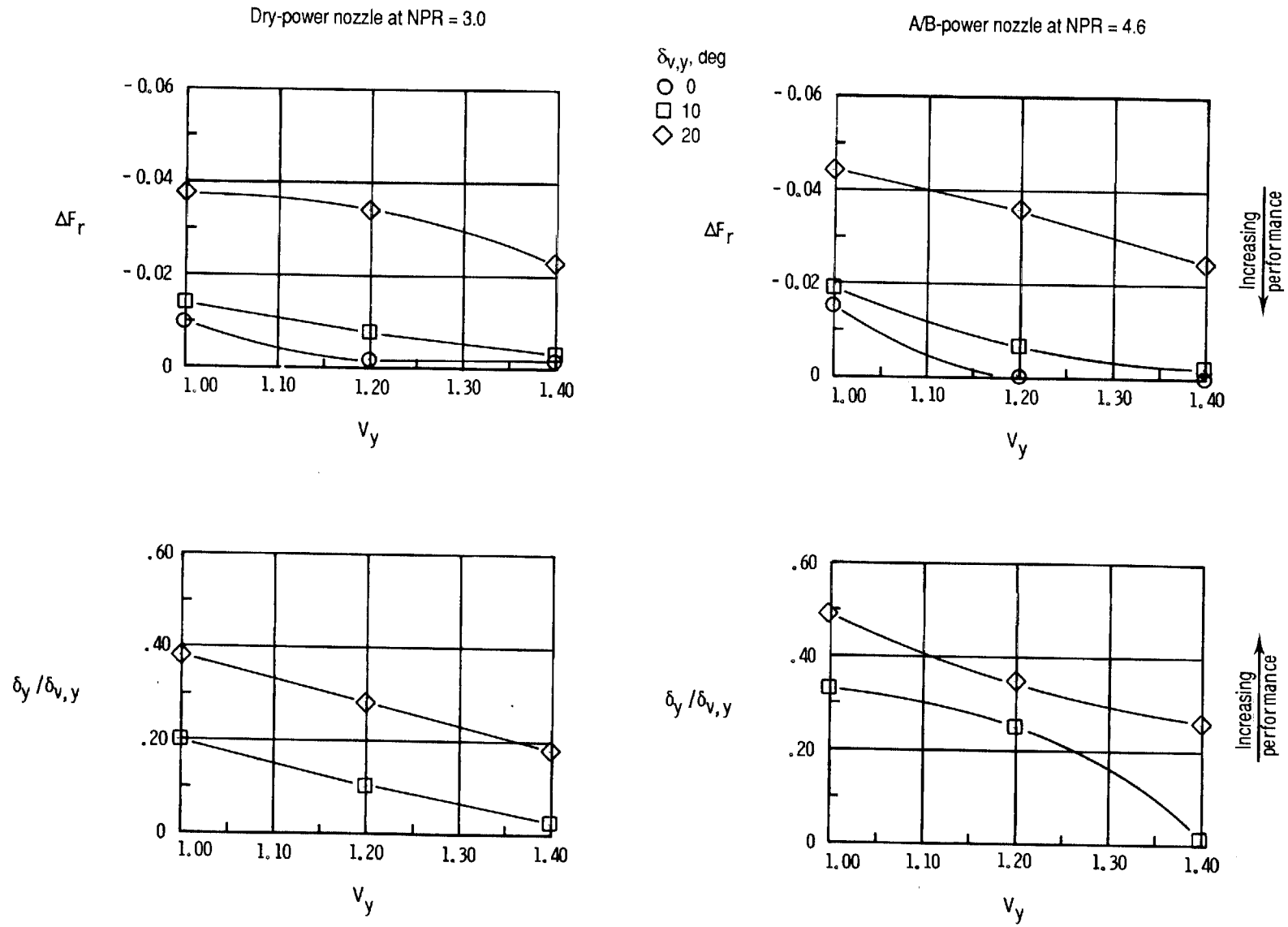

Figure 20. Effect of vane lateral position and yaw angle on nozzle performance and turning efficiency for unvectored nozzle with size A vanes and $V_x = 1.000$.

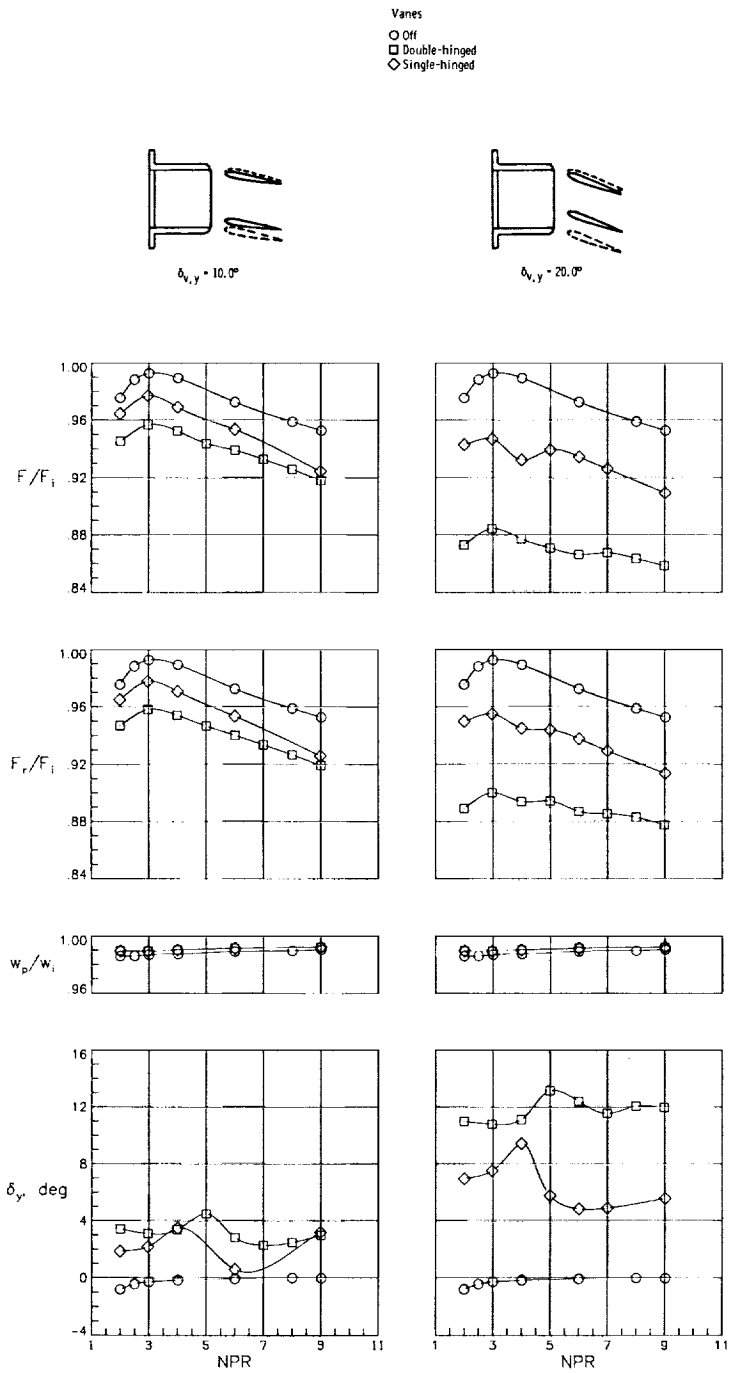

(a) Dry-power nozzle.

Figure 21. Comparison of single- and double-hinged vanes for size A vanes at position B with $\delta_{v,p} = 0°$.

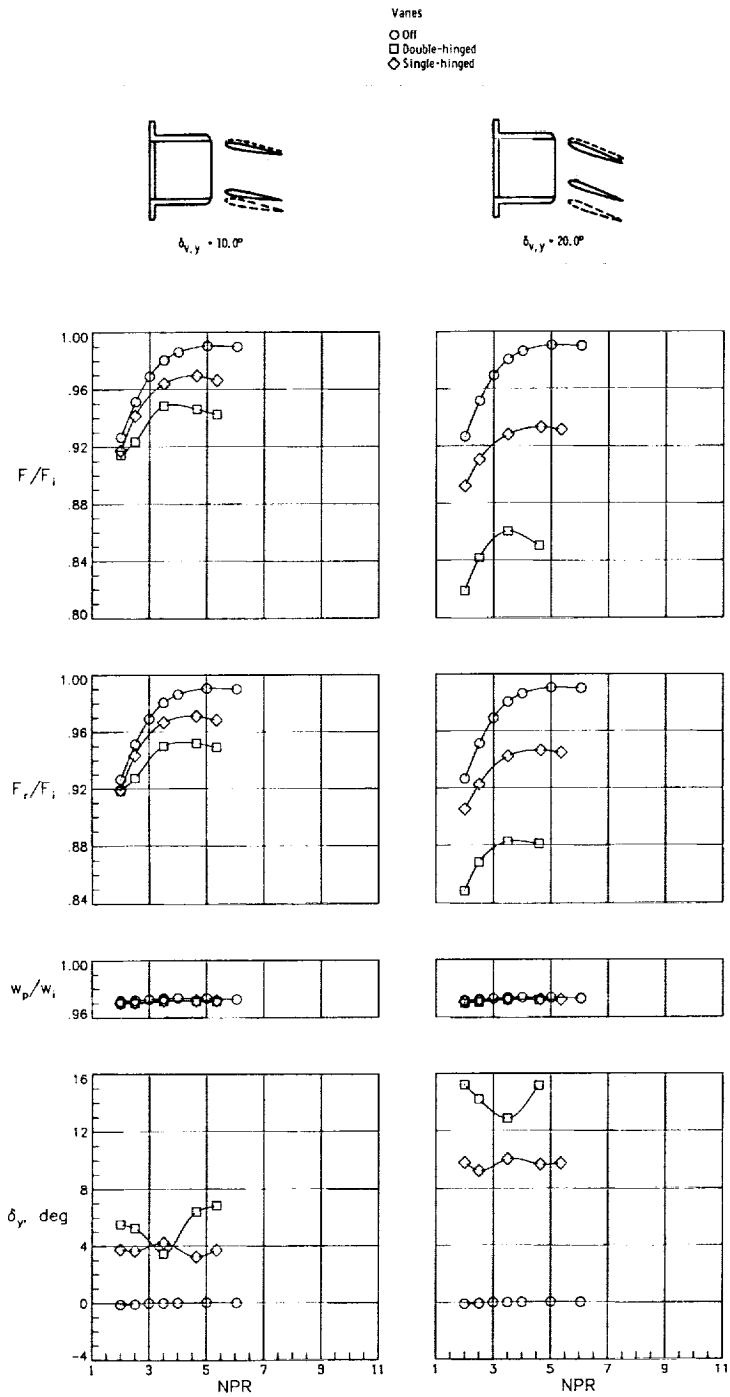

(b) A/B power nozzle.

Figure 21. Concluded.

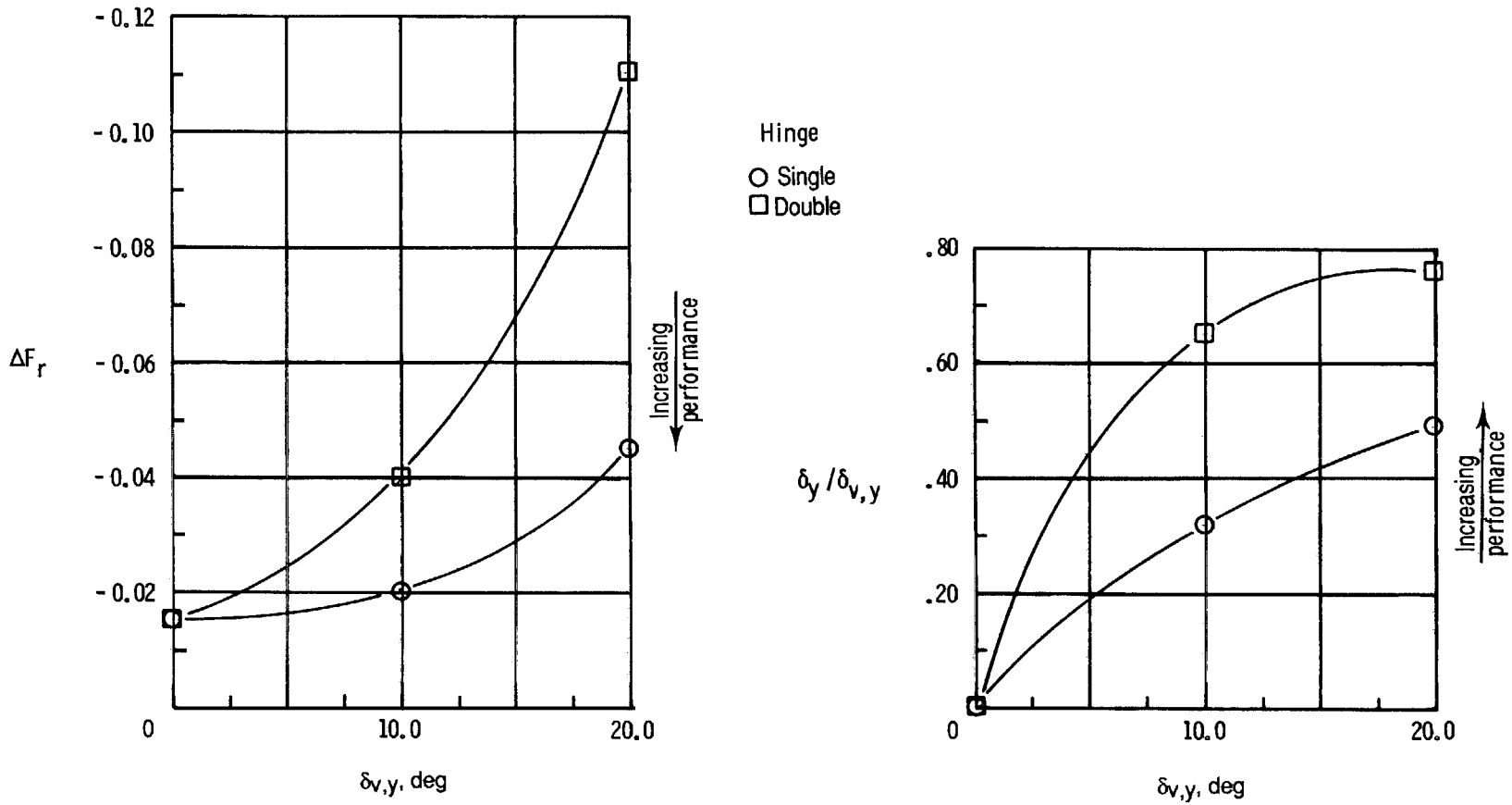

Figure 22. Effect of vane hinge type and yaw angle on A/B power nozzle performance and turning efficiency for unvectored nozzle with size A vanes, NPR = 4.6, $V_x = 1.455$, and $V_y = 1.00$.

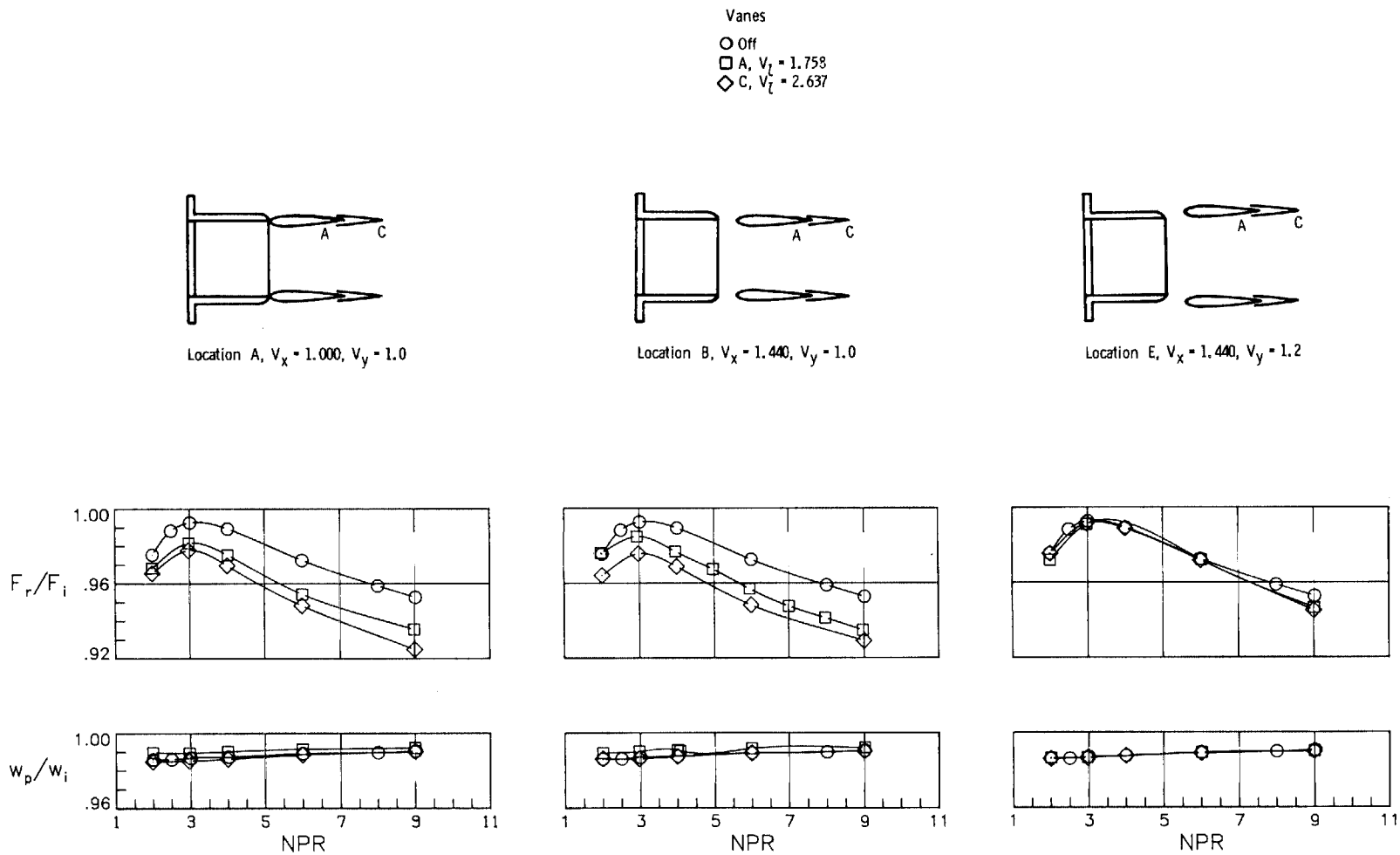

(a) $\delta_{v,y} = 0°$.

Figure 23. Effect of vane length for dry-power nozzle with $\delta_{v,p} = 0°$.

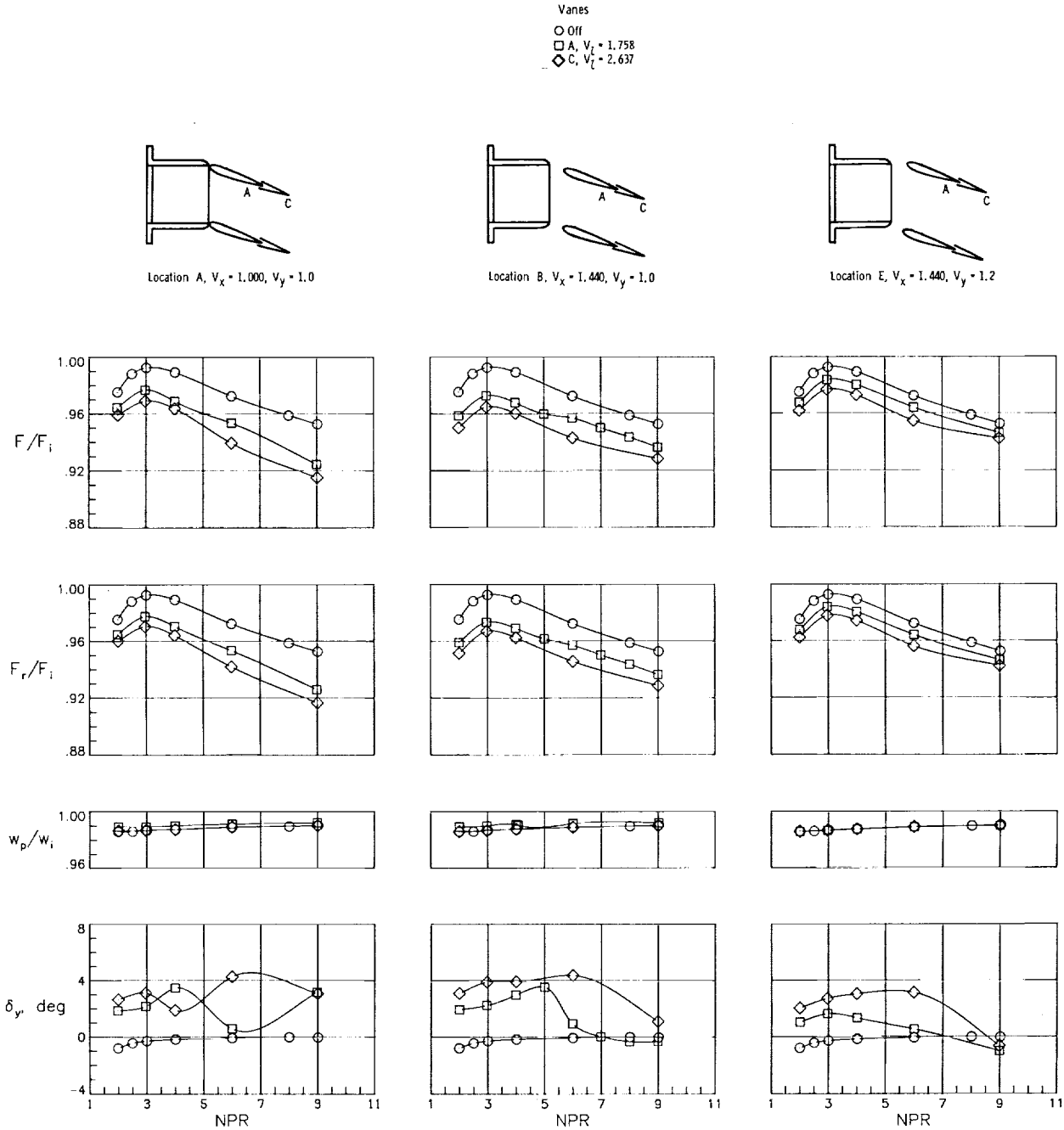

(b) $\delta_{v,y} = 10°$.

Figure 23. Continued.

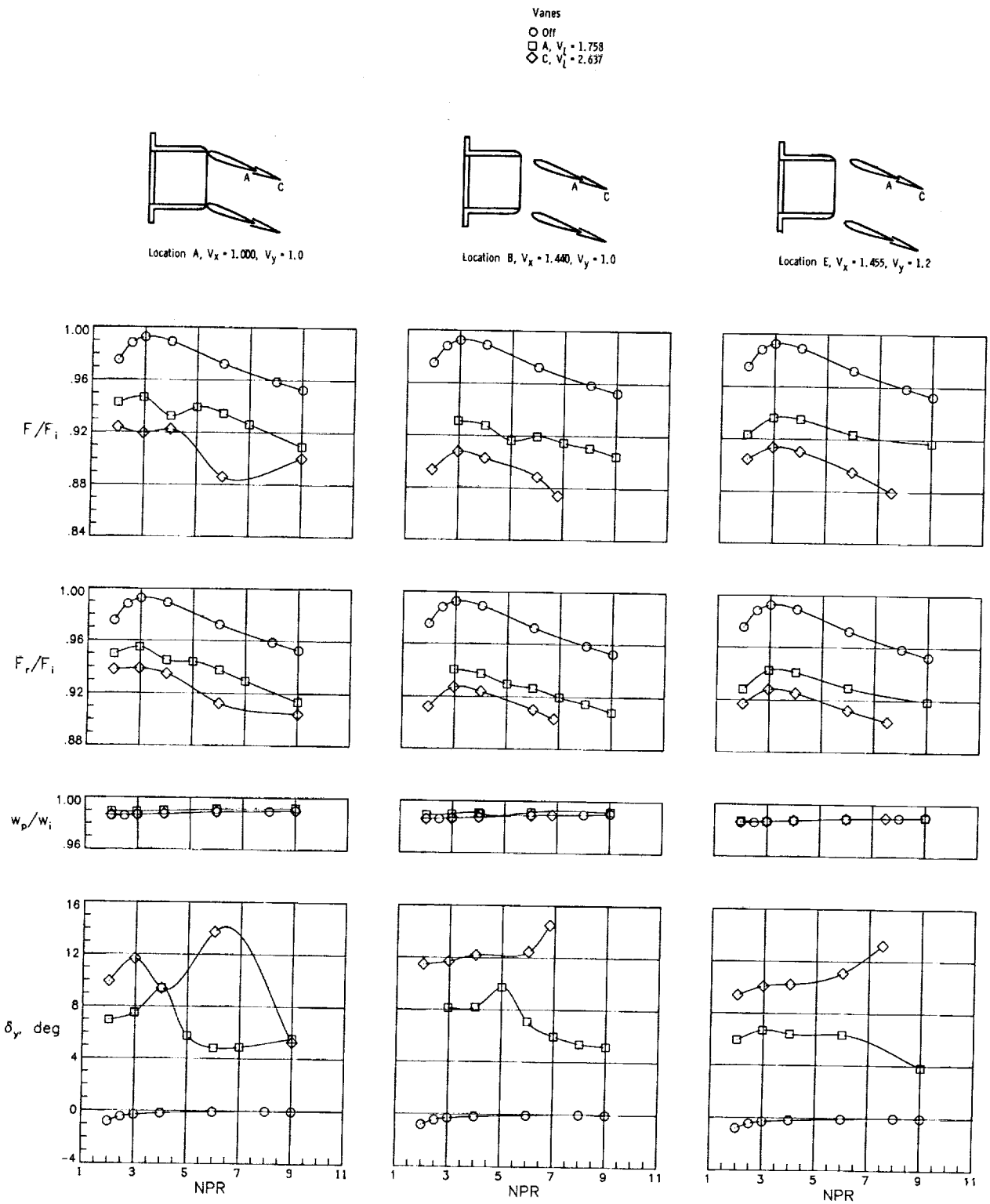

(c) $\delta_{v,y} = 20°$.

Figure 23. Concluded.

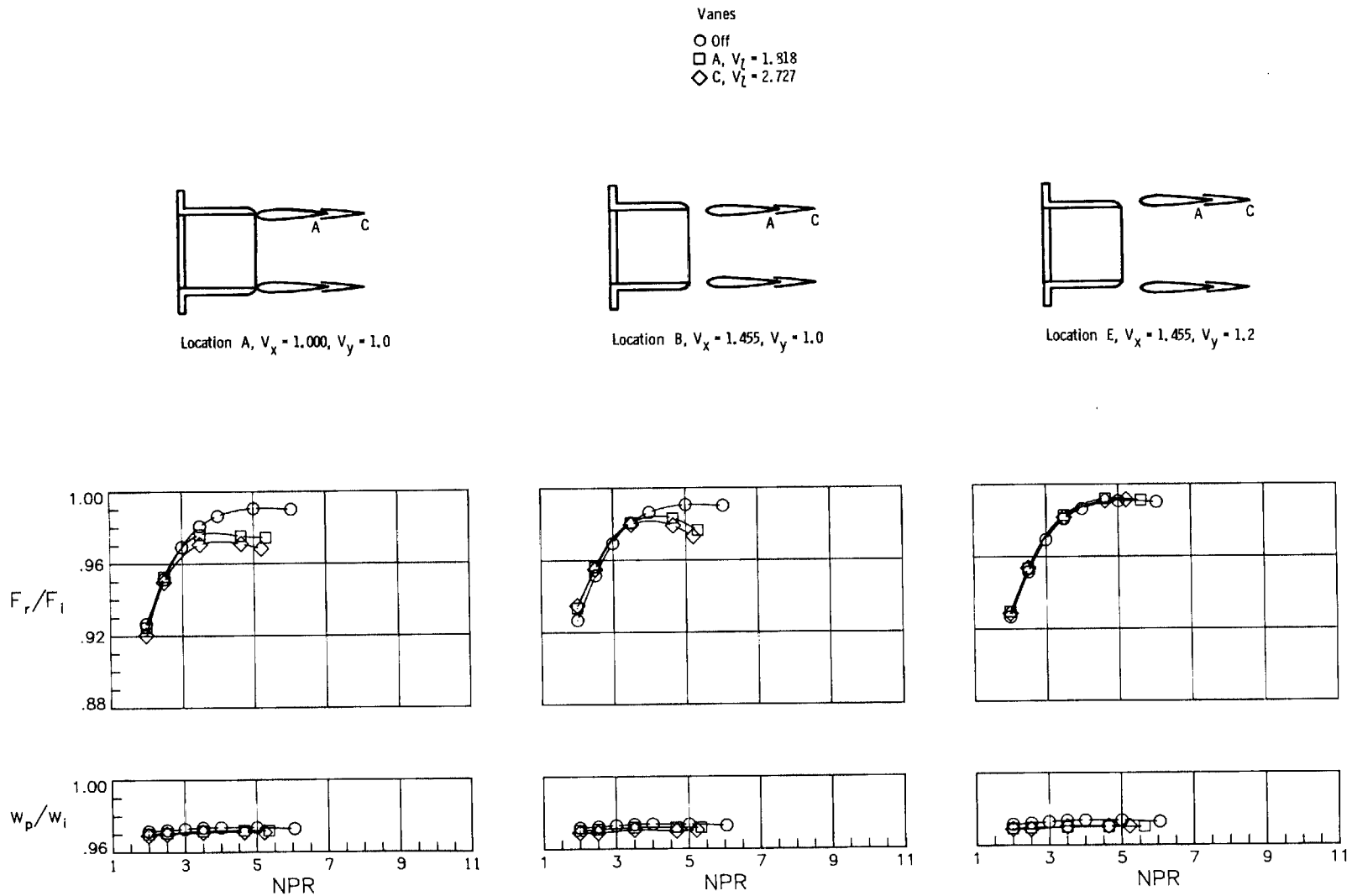

(a) $\delta_{v,y} = 0°$.

Figure 24. Effect of vane length for A/B power nozzle with $\delta_{v,p} = 0°$.

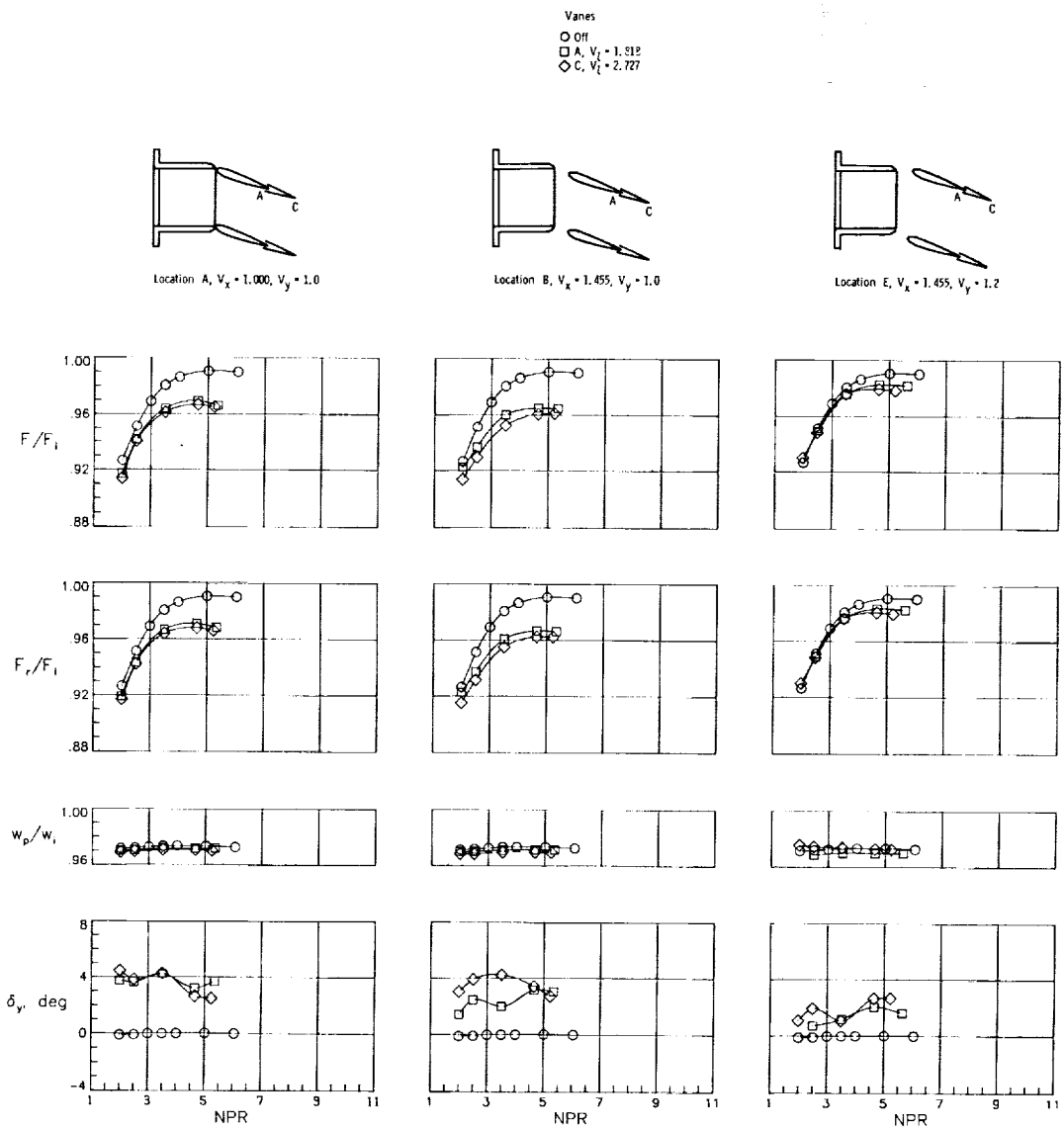

(b) $\delta_{v,y} = 10°$.

Figure 24. Continued.

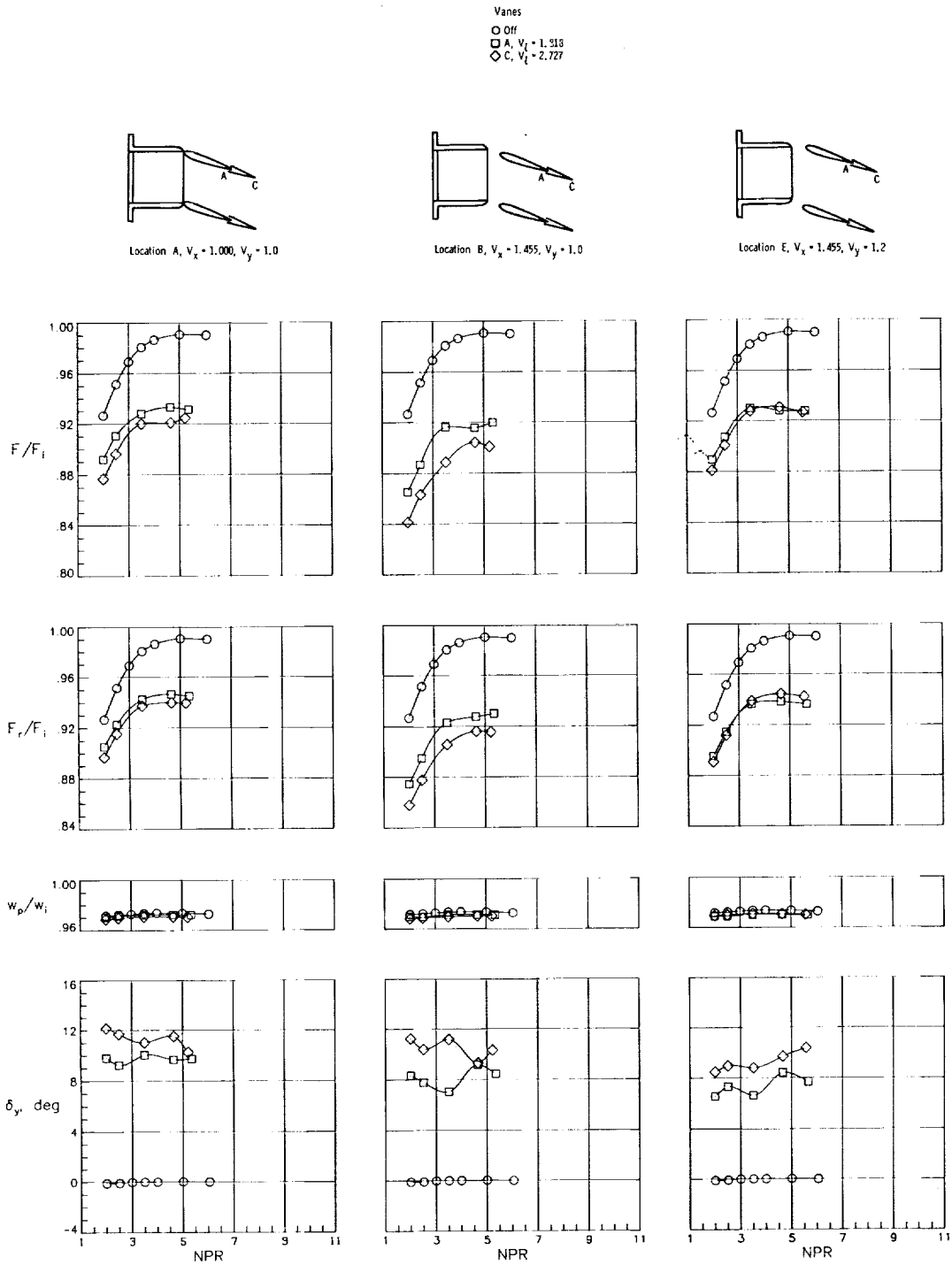

(c) $\delta_{v,y} = 20°$.

Figure 24. Concluded.

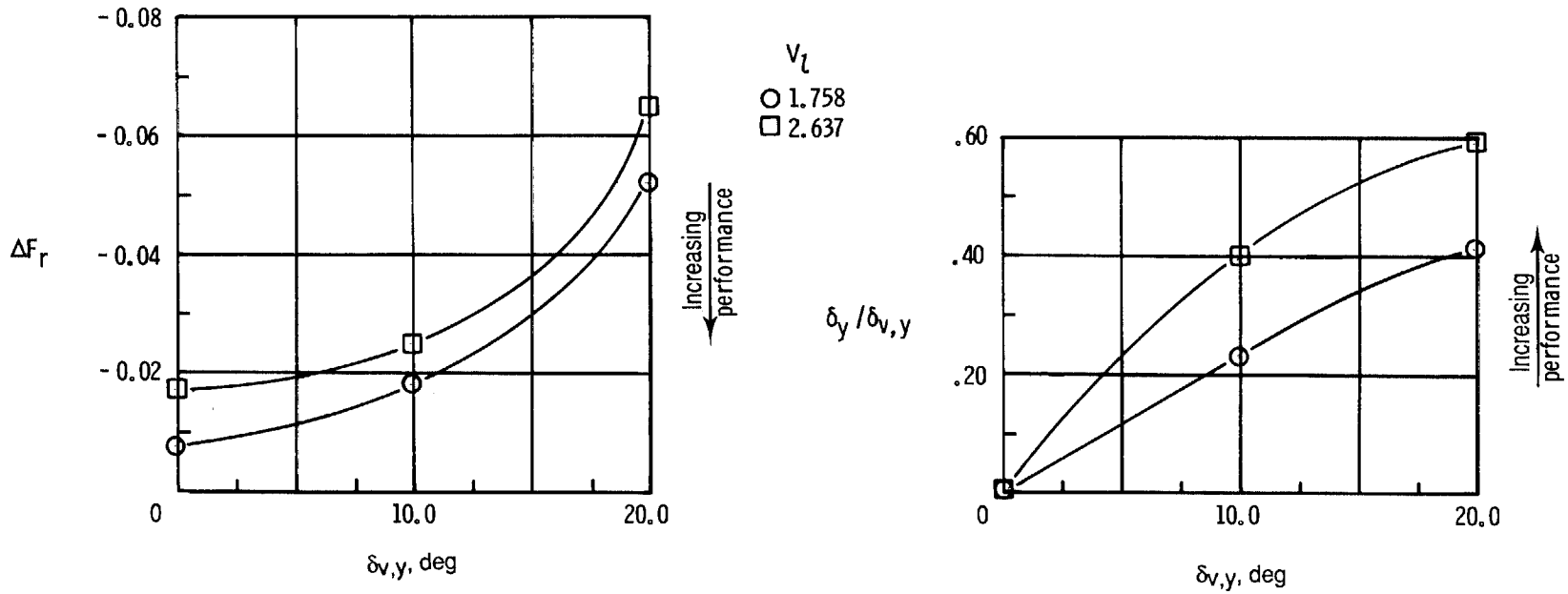

Figure 25. Effect of vane length and yaw angle on dry-power nozzle performance and turning efficiency for unvectored nozzle with size A and size C vanes, NPR = 3.0, $V_x = 1.440$, and $V_y = 1.00$.

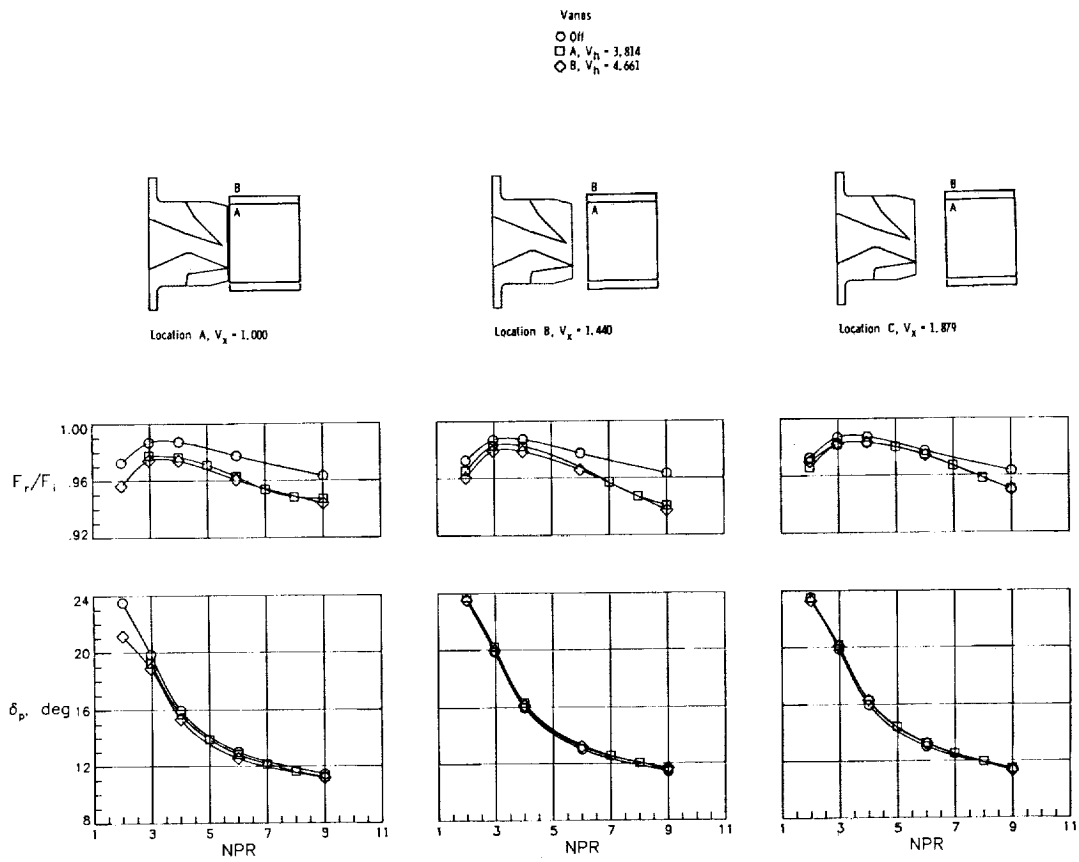

(a) $\delta_{v,y} = 0°$.

Figure 26. Effect of vane height for dry-power nozzle with $\delta_{v,p} = 19.56°$ and $V_y = 1.00$.

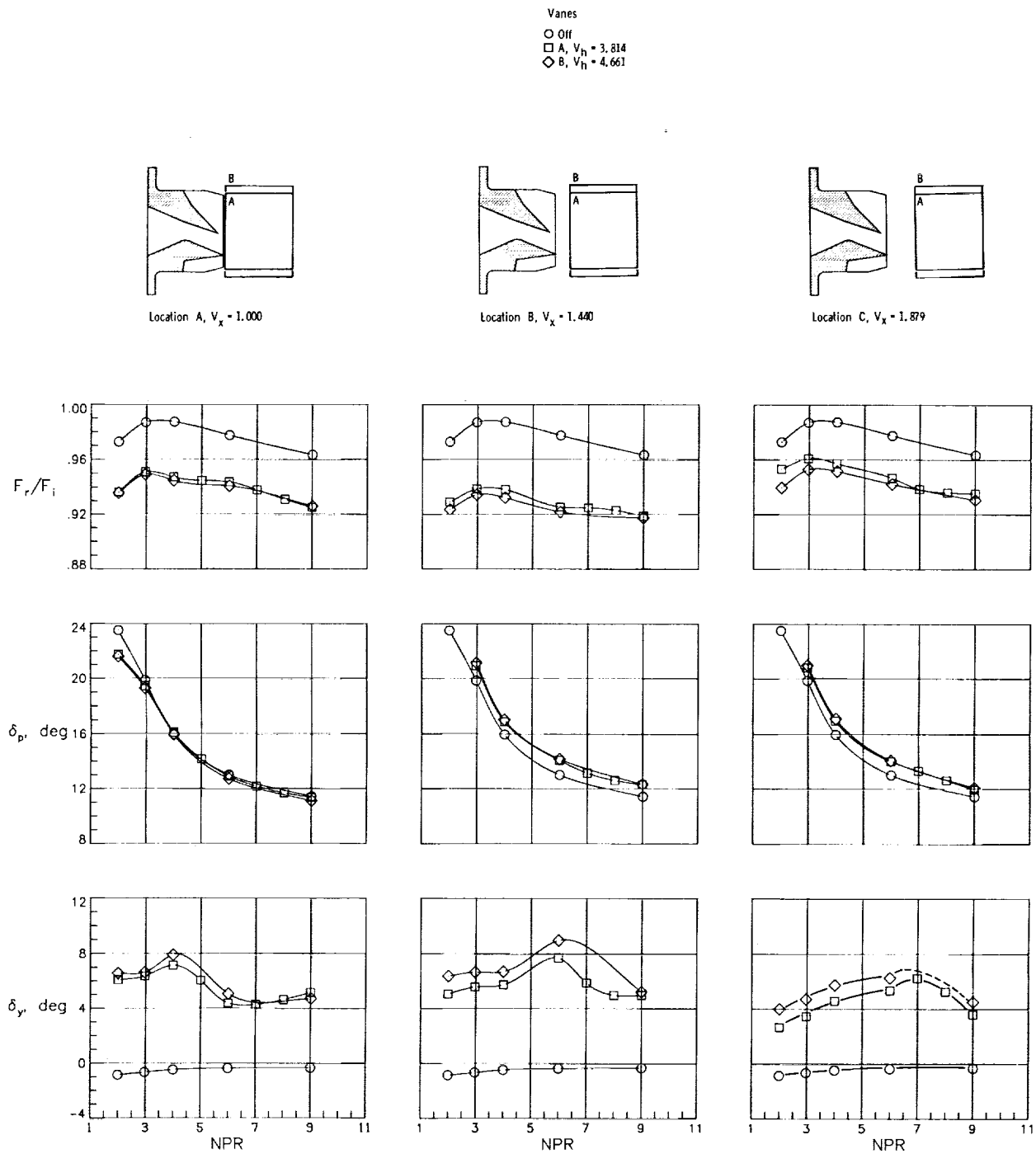

(b) $\delta_{v,y} = 10°$.

Figure 26. Continued.

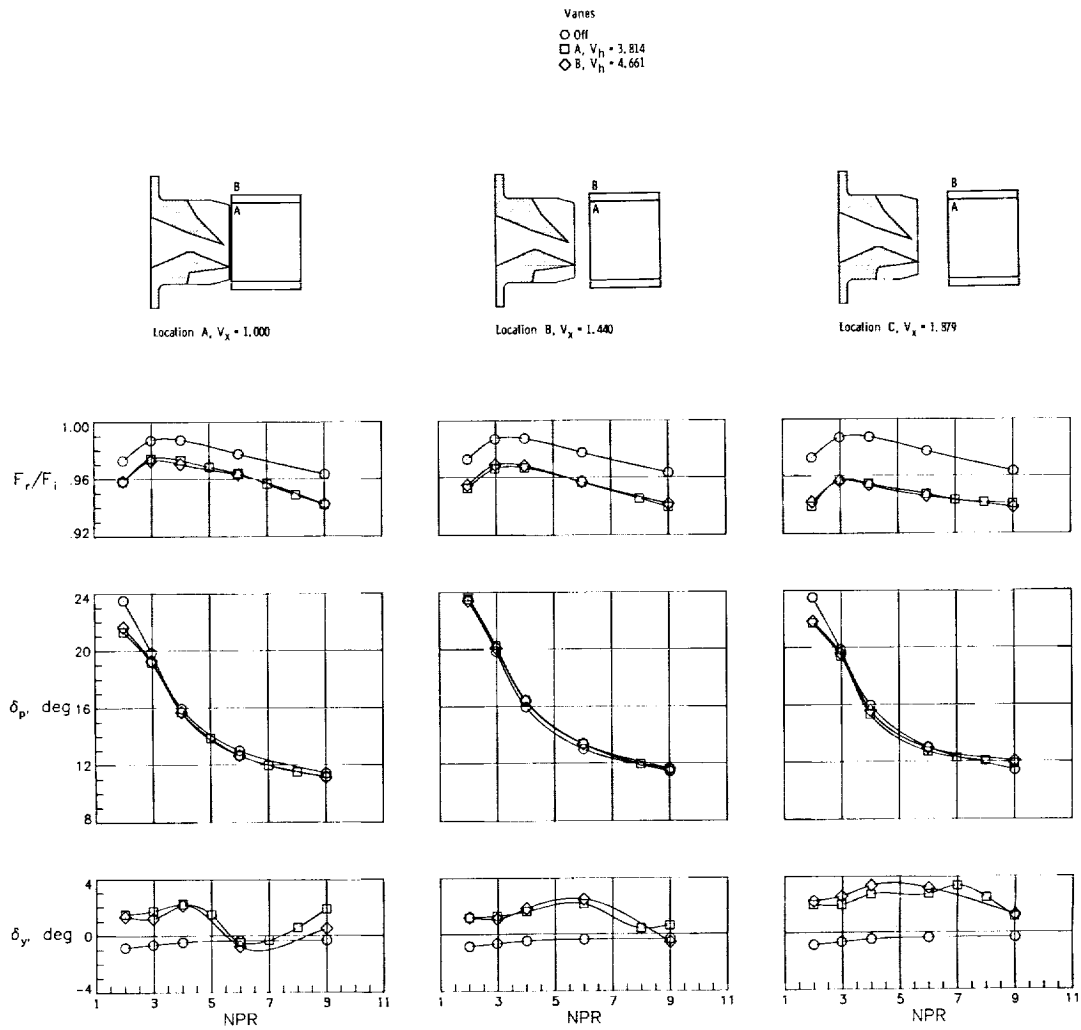

(c) $\delta_{v,y} = 20°$.

Figure 26. Concluded.

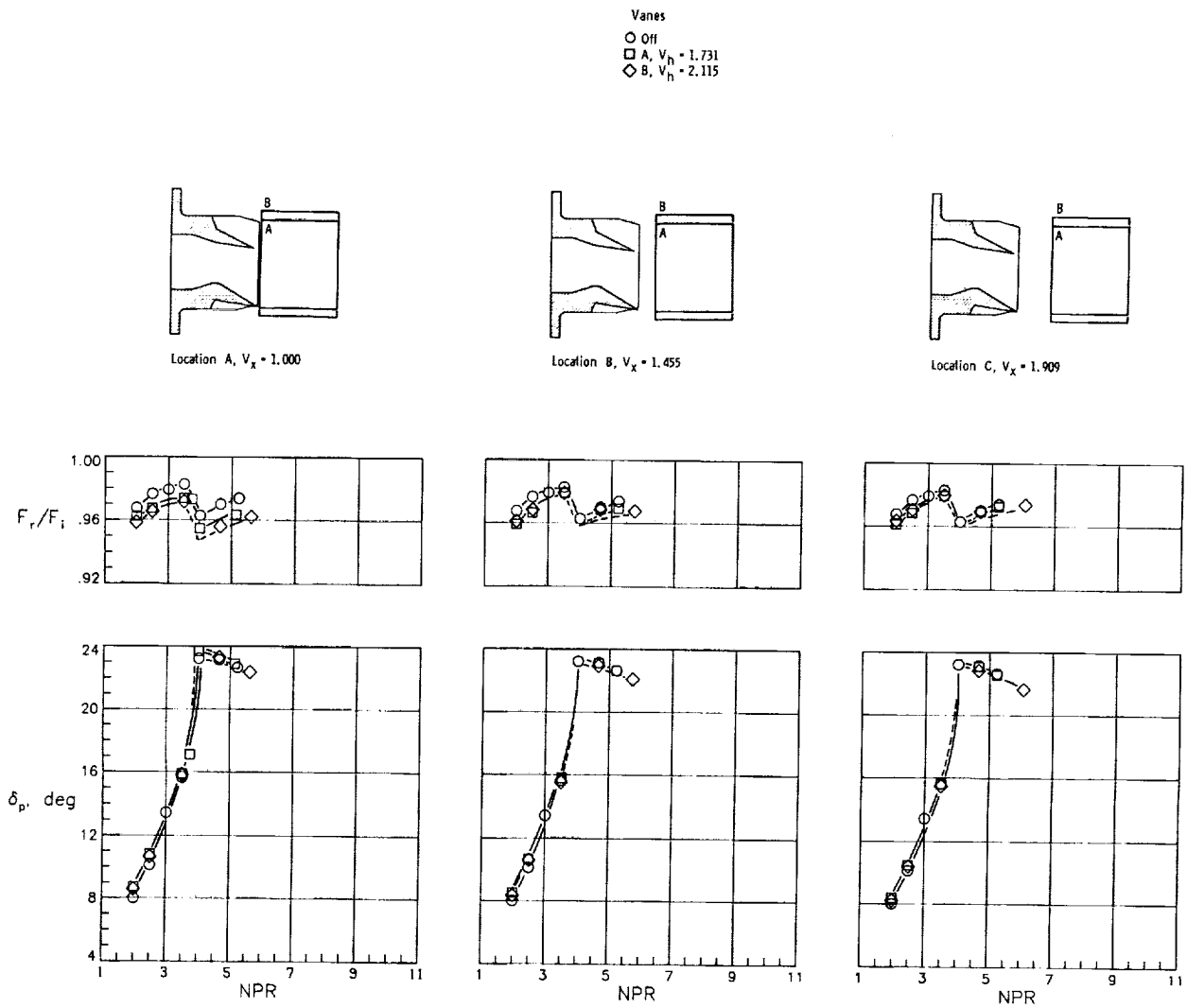

(a) $\delta_{v,y} = 0°$.

Figure 27. Effect of vane height for A/B power nozzle with $\delta_{v,p} = 20.26°$ and $V_y = 1.00$.

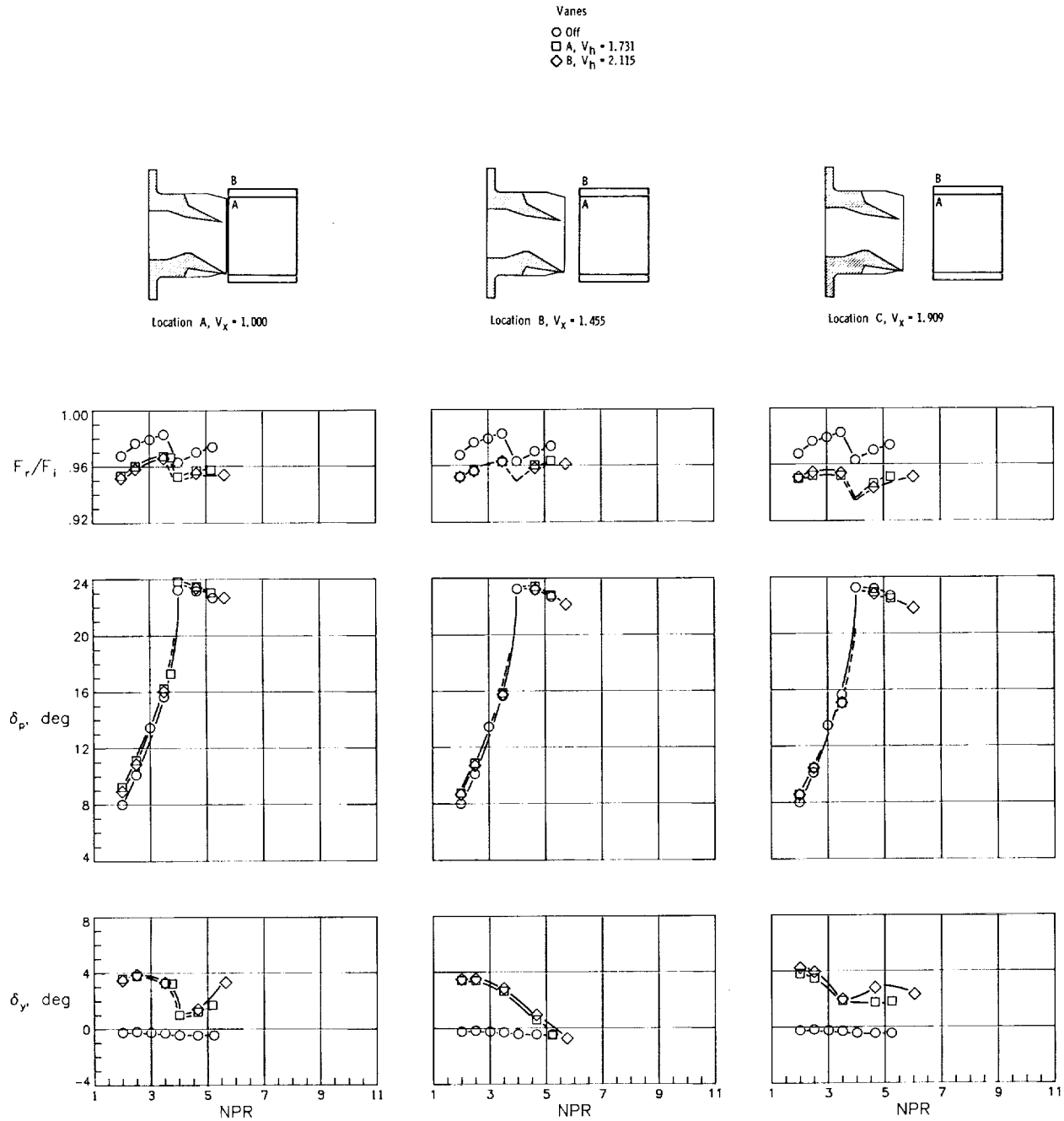

(b) $\delta_{v,y} = 10°$.

Figure 27. Continued.

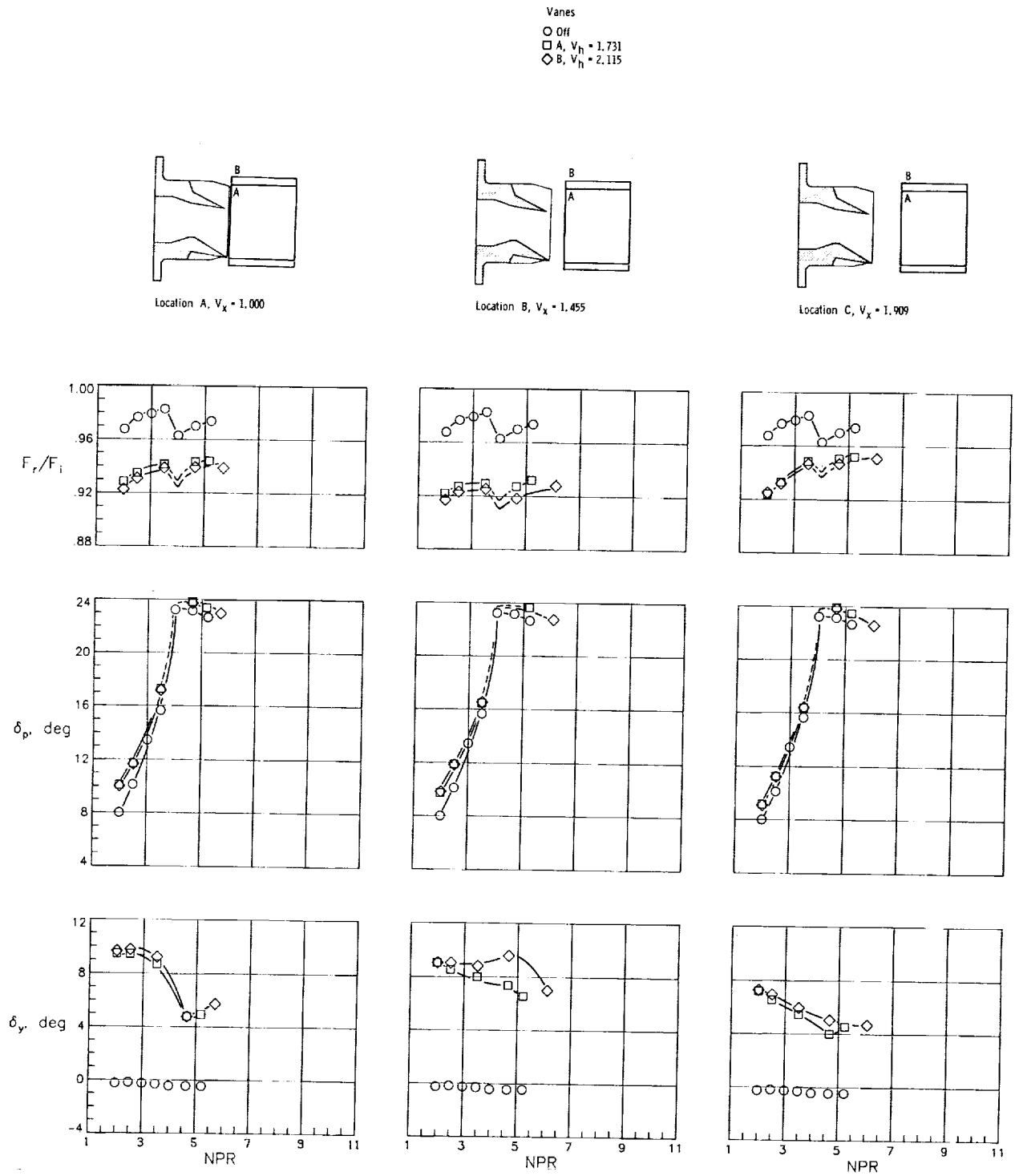

(c) $\delta_{v,y} = 20°$.

Figure 27. Concluded.

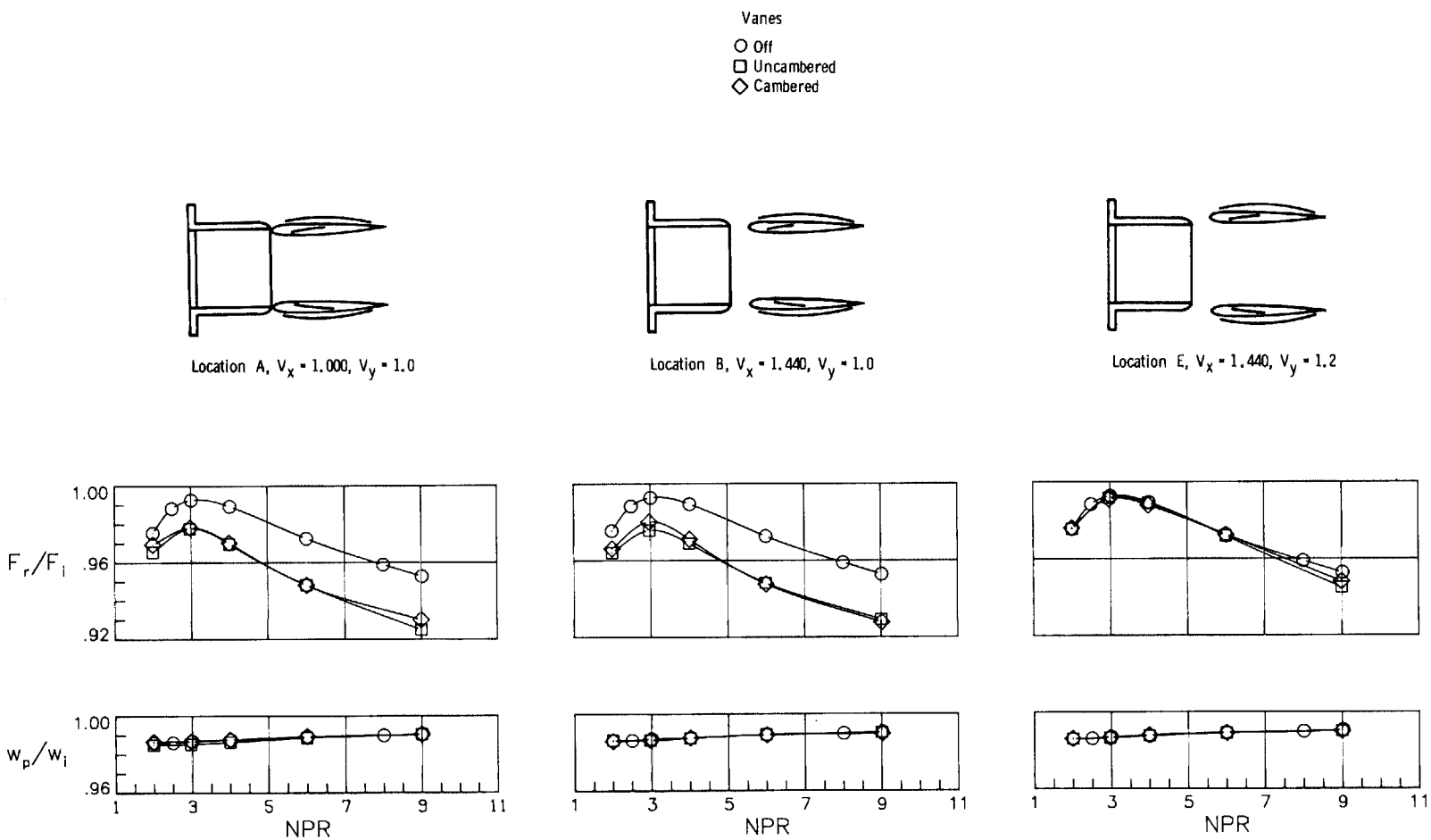

(a) $\delta_{v,y} = 0°$.

Figure 28. Effect of vane camber for dry-power nozzle with $\delta_{v,p} = 0°$.

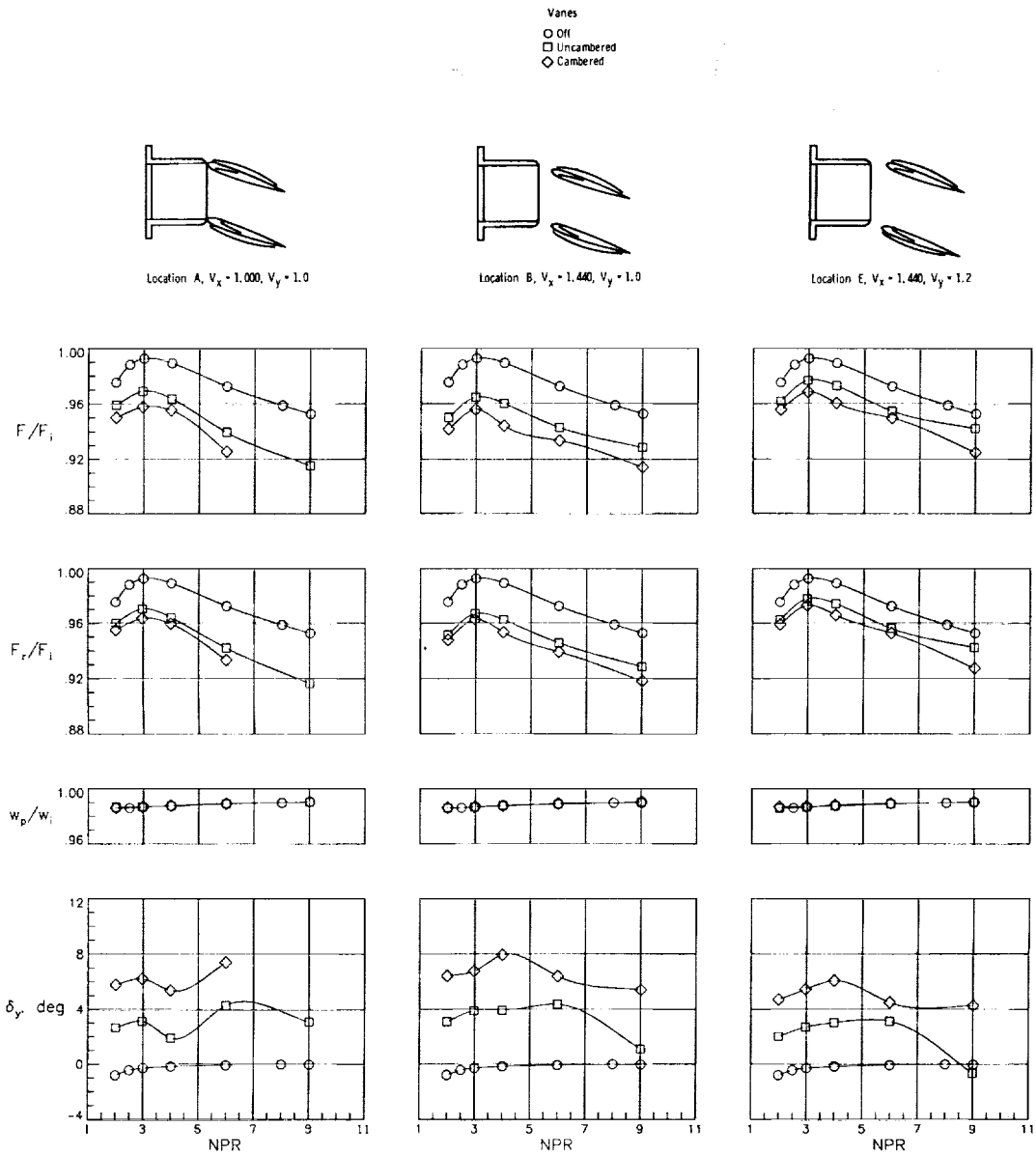

(b) $\delta_{v,y} = 10°$.

Figure 28. Continued.

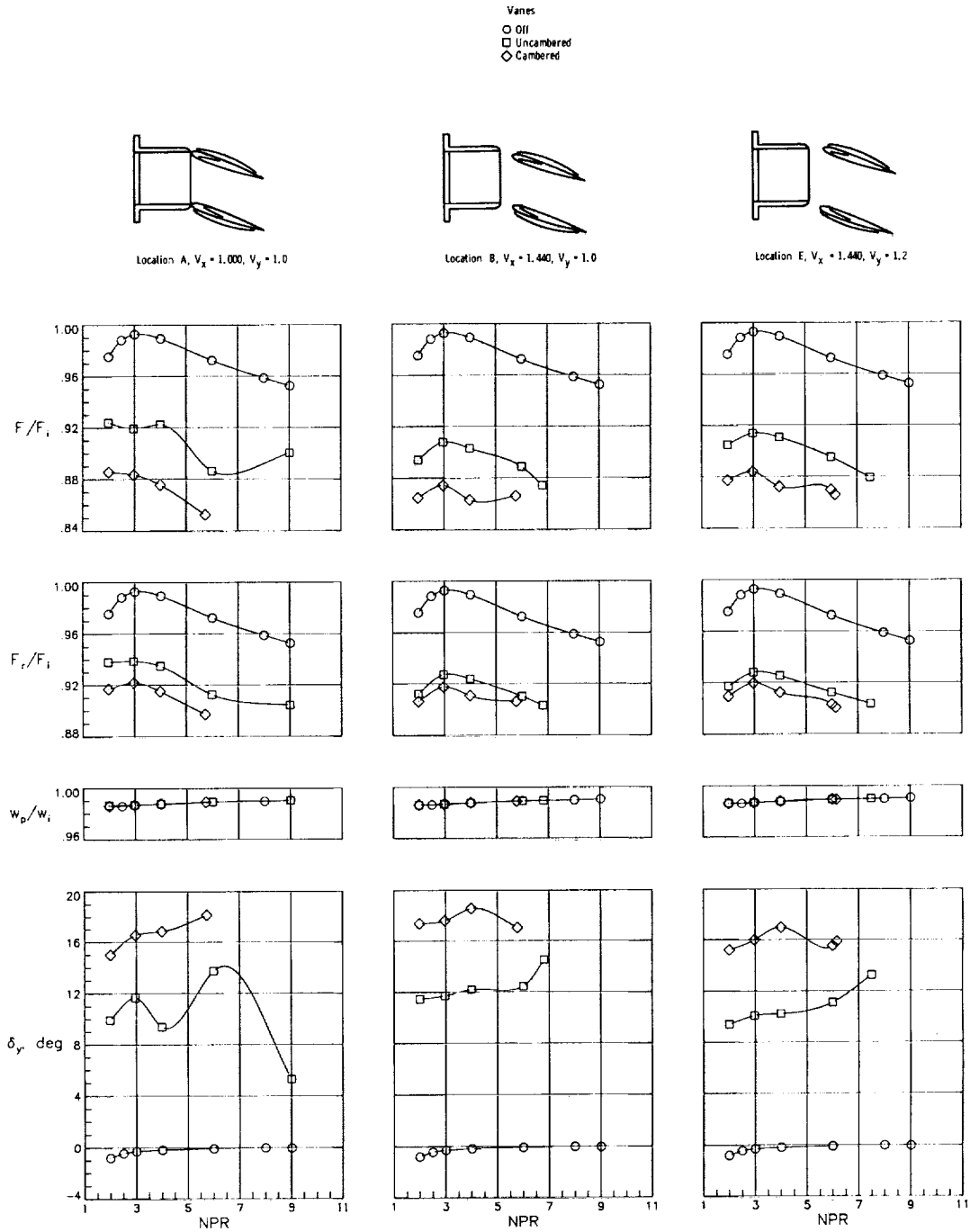

(c) $\delta_{v,y} = 20°$.

Figure 28. Concluded.

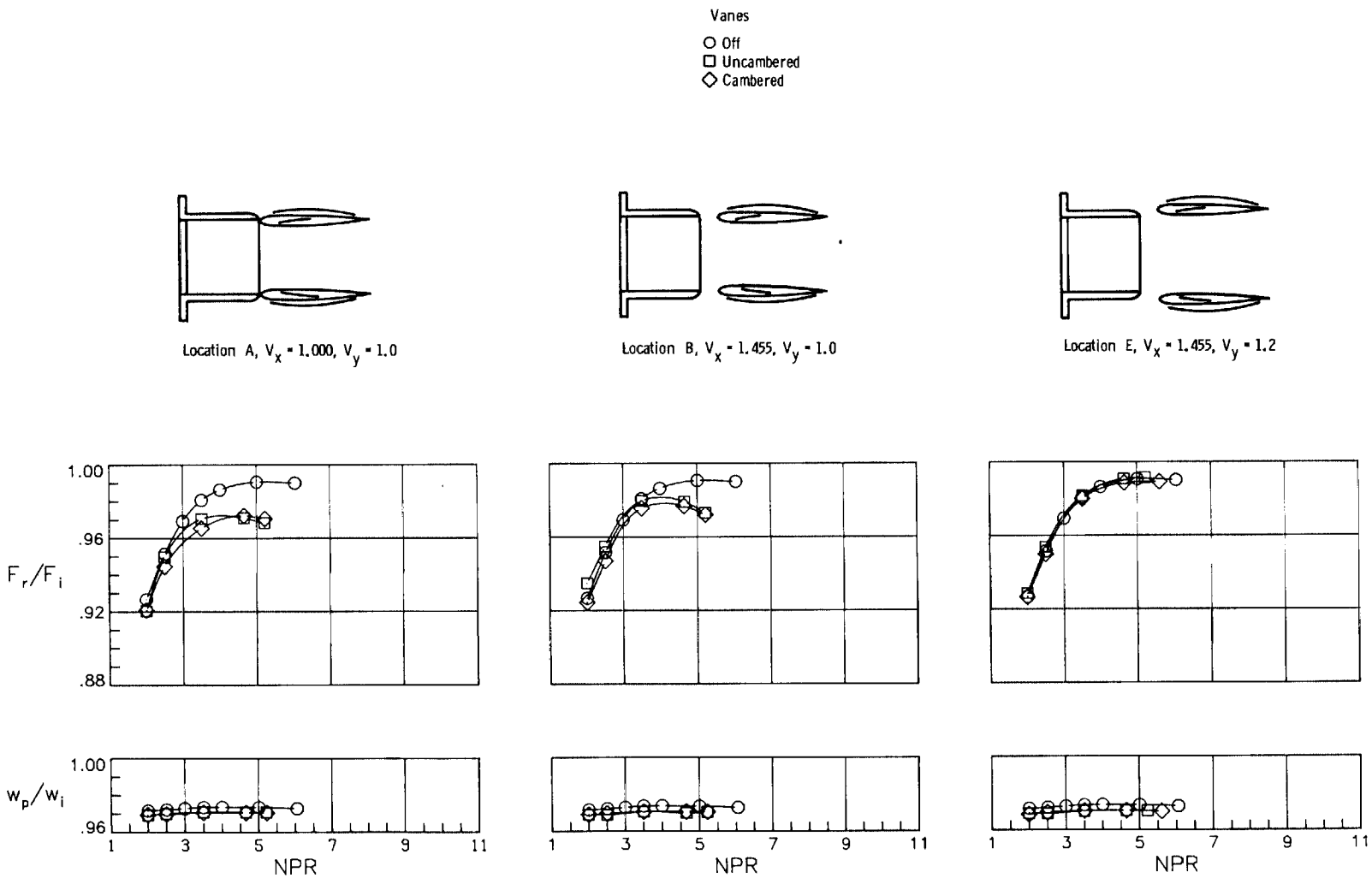

(a) $\delta_{v,y} = 0°$.

Figure 29. Effect of vane camber for A/B power nozzle with $\delta_{v,p} = 0°$.

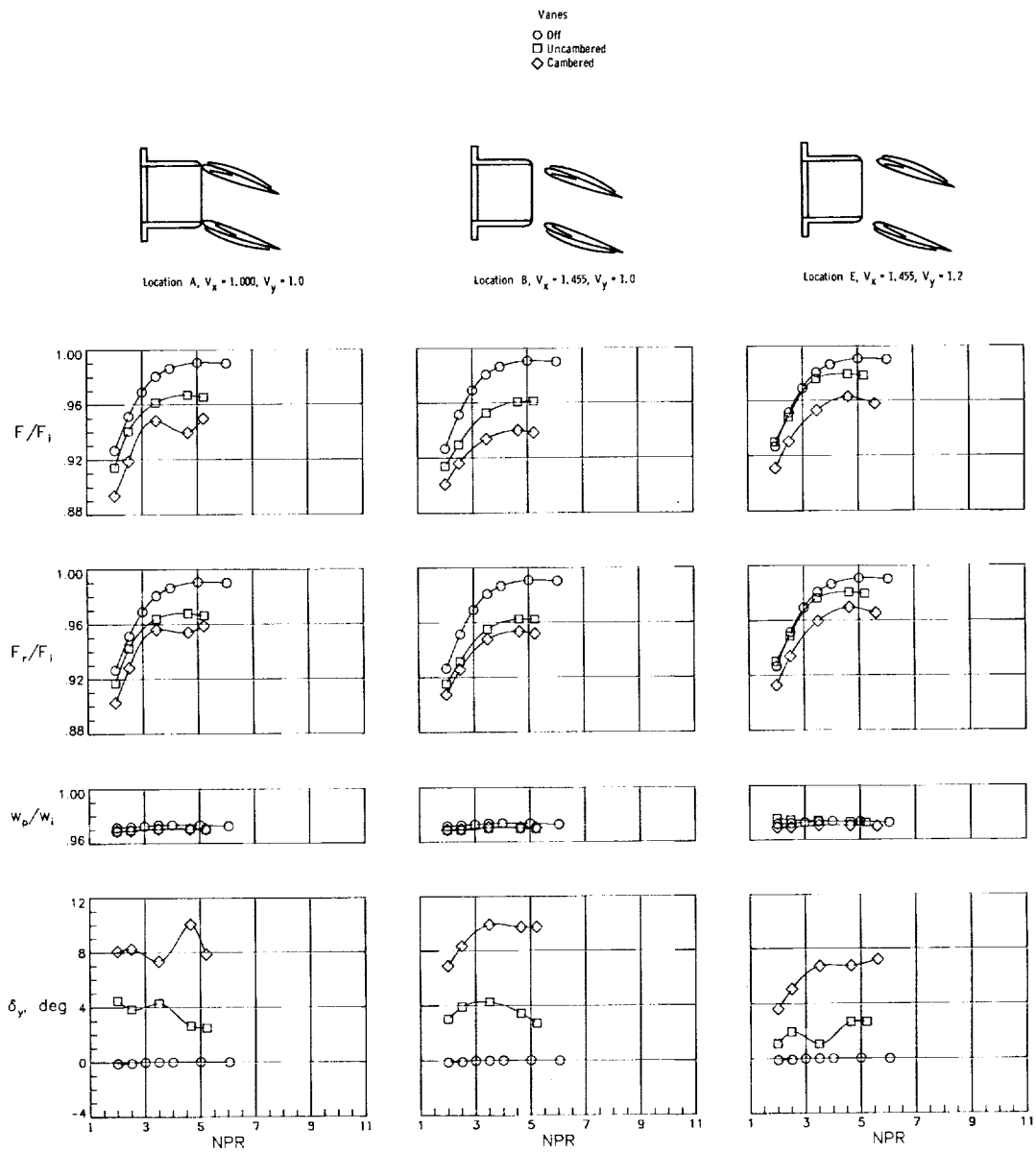

(b) $\delta_{v,y} = 10°$.

Figure 29. Continued.

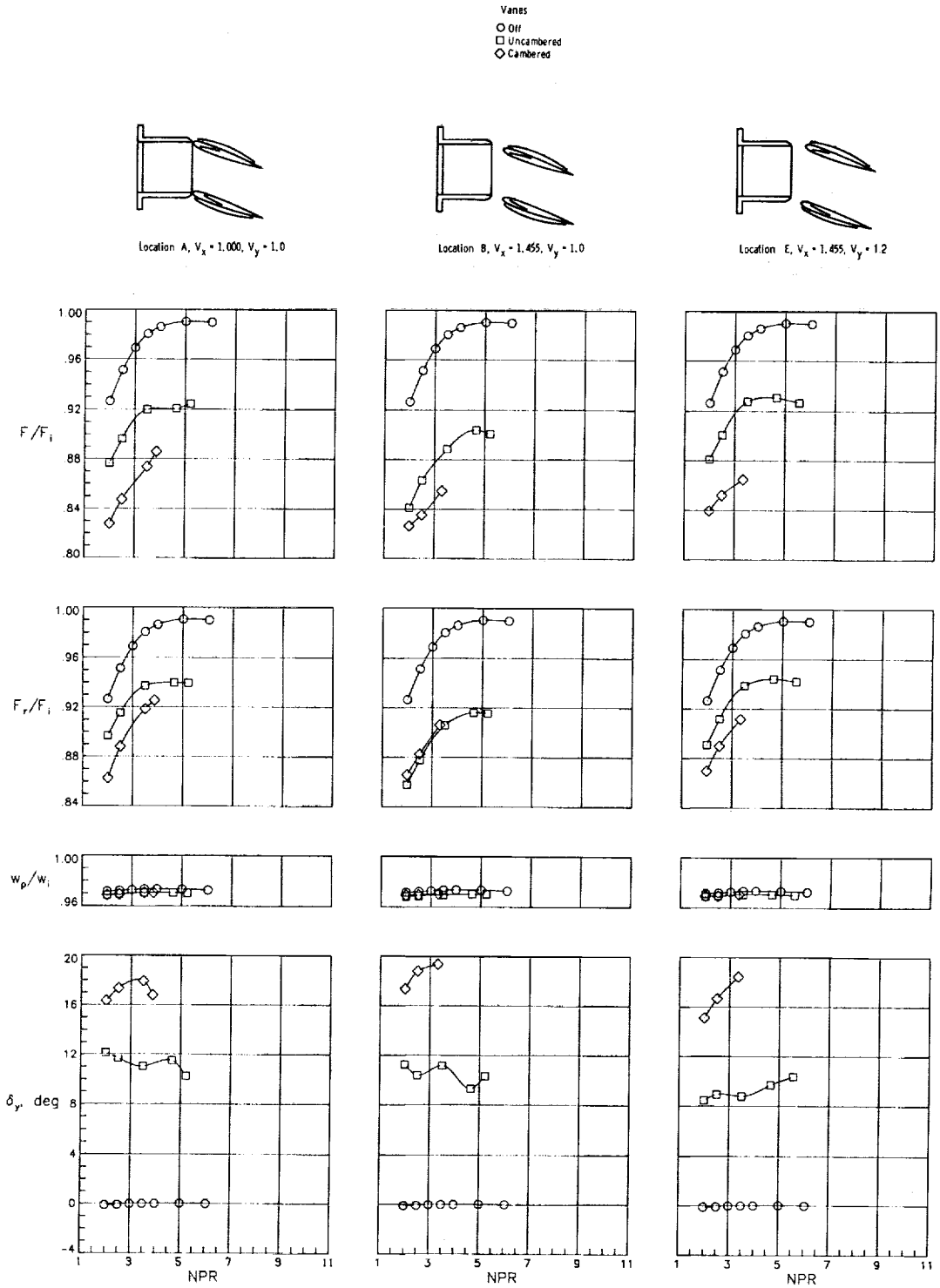

(c) $\delta_{v,y} = 20°$.

Figure 29. Concluded.

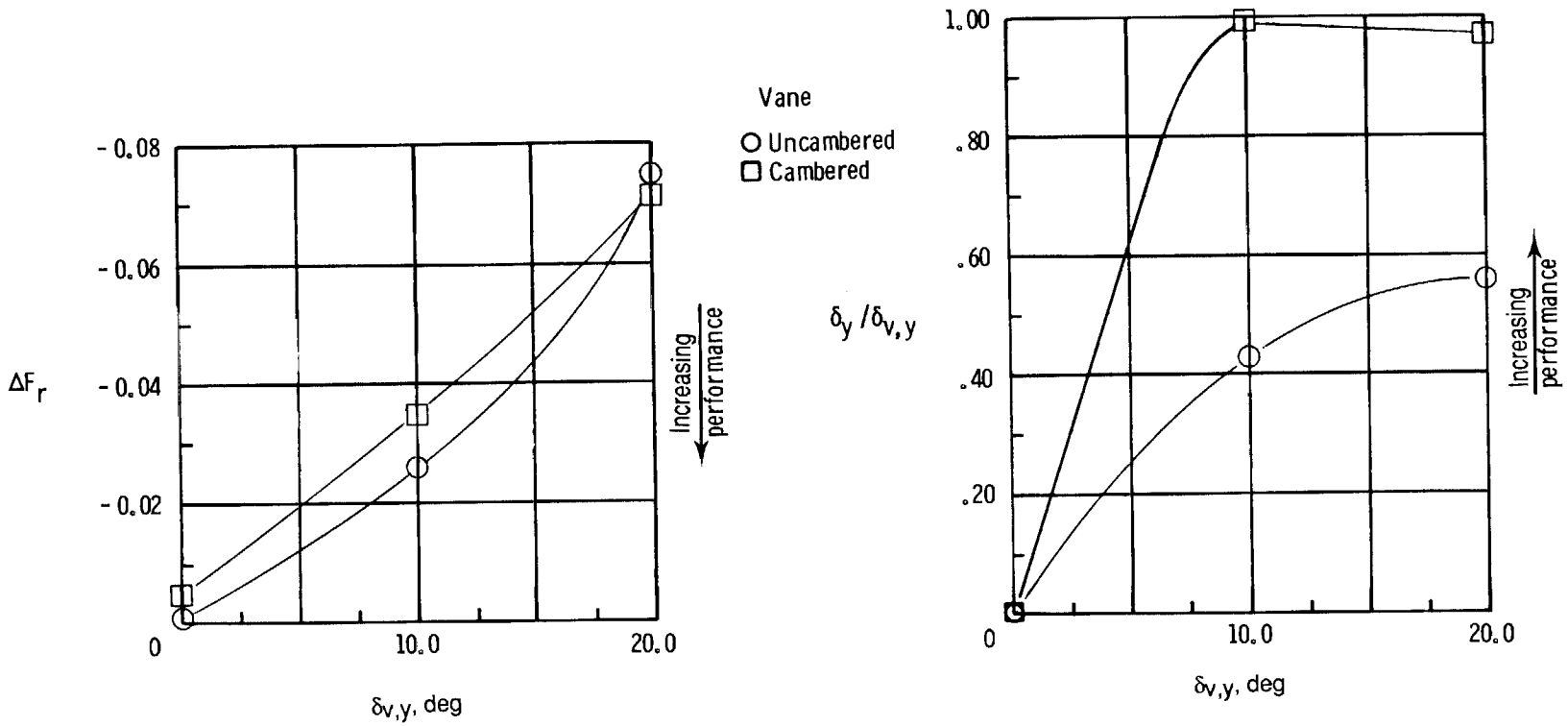

Figure 30. Effect of vane camber and yaw angle on A/B power nozzle performance and turning efficiency for unvectored nozzle with size C vanes, NPR ≈ 3.5, $V_x = 1.455$, and $V_y = 1.00$.

NASA
National Aeronautics and Space Administration

Report Documentation Page

1. Report No. NASA TP-3085	2. Government Accession No.	3. Recipient's Catalog No.
4. Title and Subtitle Static Thrust-Vectoring Performance of Nonaxisymmetric Convergent-Divergent Nozzles With Post-Exit Yaw Vanes		5. Report Date May 1991
		6. Performing Organization Code
7. Author(s) Robert J. Foley and Odis C. Pendergraft, Jr.		8. Performing Organization Report No. L-16784
9. Performing Organization Name and Address NASA Langley Research Center Hampton, VA 23665-5225		10. Work Unit No. 505-62-71-01
		11. Contract or Grant No.
12. Sponsoring Agency Name and Address National Aeronautics and Space Administration Washington, DC 20546-0001		13. Type of Report and Period Covered Technical Paper
		14. Sponsoring Agency Code

15. Supplementary Notes

Robert J. Foley: The George Washington University Joint Institute for Advancement of Flight Sciences, Hampton, Virginia.
Odis C. Pendergraft, Jr.: Langley Research Center, Hampton, Virginia.
Part of the information presented in this report was included in a thesis submitted by Robert J. Foley in partial fulfillment of the requirements for the degree of Master of Science at The George Washington University, Washington, D.C., August 1988.

16. Abstract

A static (wind-off) test has been conducted in the static test facility of the Langley 16-Foot Transonic Tunnel to determine the performance and turning effectiveness of post-exit yaw vanes installed on two-dimensional convergent-divergent nozzles. One nozzle design that had previously been tested was used as a baseline, simulating dry-power and afterburning power nozzles at both 0° and 20° pitch-vectoring conditions. Vanes were installed on these four nozzle configurations to study the effects of vane deflection angle, longitudinal and lateral location, size, and camber. All vanes were hinged at the nozzle sidewall exit, and some were also hinged at the vane quarter-chord (double-hinged). The vane concepts tested generally produced yaw thrust-vectoring angles that were much smaller than the geometric vane angles for large (up to 8 percent) resultant thrust losses. When the nozzles were pitch vectored, yawing effectiveness decreased as the vanes were moved downstream. Thrust penalties and yawing effectiveness decreased rapidly as the vanes were moved outboard (laterally). Vane length and height changes increased yawing effectiveness and thrust-ratio losses while using vane camber, and double-hinged vanes increased resultant yaw angles by 50 to 100 percent.

17. Key Words (Suggested by Author(s)) Nonaxisymmetric nozzles; Convergent-divergent nozzles; Static thrust vectoring; Cambered vanes; Post-exit vanes; Vane location and shape		18. Distribution Statement Unclassified—Unlimited; Subject Category 02	
19. Security Classif. (of this report) Unclassified	20. Security Classif. (of this page) Unclassified	21. No. of Pages 80	22. Price A05

NASA FORM 1626 OCT 86 NASA-Langley, 1991

For sale by the National Technical Information Service, Springfield, Virginia 22161-2171